SCUOLA DI DOTTORATO
UNIVERSITÀ DEGLI STUDI DI MILANO-BICOCCA

Dipartimento di / Department of

Scienza dei Materiali

Dottorato di Ricerca in / PhD program Scienza e Nanotecnologia dei Materiali Ciclo / Cycle XXIX

Curriculum in (se presente / if it is) .....

ADVANCED STRATEGIES FOR LIGHT MANAGEMENT IN PHOTONICS, IMAGING AND SENSING

Cognome / Surname Pedrini Nome / Name Jacopo

Matricola / Registration number 709055

Tutore / Tutor: Prof. Francesco Meinardi

Cotutore / Co-tutor: .....
(se presente / if there is one)

Supervisor: .....
(se presente / if there is one)

Coordinatore / Coordinator: Prof. Gian Paolo Brivio

ANNO ACCADEMICO / ACADEMIC YEAR 2015/2016

CONTENTS

INTRODUCTION

In this work I report the research activities I conducted during the three years of my Ph.D. My work was mainly focused on efficient materials for photon managing in several applications. The major topic I dealt with during my thesis was the development and the characterization of photonic crystals based on novel, extremely high refractive index materials. Work on this topic was entirely performed during my year-long period abroad at the Molecular Foundry, user facility at Lawrence Berkeley National Laboratory in Berkeley, California. After my period abroad, my focus was the development of materials for biological applications such as high contrast, anti-Stokes imaging and ratiometric intracellular pH sensing.

Specifically, during my work at the Molecular Foundry, I worked on the nanofabrication and characterization of photonic crystals based on transition metal dichalcogenides (TMDs). In this period, I demonstrated the potential of TMDs for their applications to photonics, due to a surprisingly high refractive index in their transparency range. TMDs have some fabrication issues that limit their use in electronics and photonics. However, I demonstrated that these limitations can be lifted by converting the corresponding pre-processed transition metal oxide by annealing it at high temperatures in presence of a chalcogenizing agent. The synthesis of the transition metal oxide was performed with atomic layer deposition, a powerful thin film growth technique that allows for extreme control on thickness and perfect conformality over any substrate. In this work I demonstrated the possibility to overcome strong fabrication constraints for TMDs by producing, characterizing and modeling TMD-based photonic crystals. To my knowledge, this is the first example of nanofabricated structures for photonics made with TMDs.

My work on photon managing techiniques continued after my period at the Molecular Foundry, but the main interest of my research shifted towards biotechnological applications. Specifically, I carried on a project I dealt with during my master thesis that was targeted at the development of high efficiency materials for sensitized triplet-triplet annihilation based up-conversion (TTA-UC) in multicomponent organic systems. Briefly, TTA-UC is a technique that allows for the generation of a high energy light starting from a lower energy excitation. It has

great interest in solar energy, but recently it is under the spotlight for its potential as anti-Stokes, high contrast fluorophore for biological imaging. However, TTA-UC biocompatibility is still under investigation because of poor water-solubility of the most efficient materials. In my work, this issue was tackled and solved by developing self-assembled nano-micelles loaded with a model TTA-UC chromophore pair. This approach preserves TTA-UC performances in water and biological media.

In parallel, I carried on the work on biological applications of photon managing techniques for a different target, the sensing of intracellular pH with a particular class of core/shell engineered heterostructured nanocrystals called Dot-in-Bulk (DiB). These nanocrystals feature a dual color emission consisting in well separated red and green bands originating from core and shell, respectively. The different exposure to the environment of core and shell determines a different sensitivity to oxidative and reductive species as H^+ and OH^- ions, respectively. Specifically, the core is weakly affected by the environment, while the opposite is true for the shell. This double sensitivity makes DiB extremely promising for ratiometric pH sensing. In this work, pH sensitivity was first demonstrated in solution. Then, DiB were internalized in human embrionic kidney (HEK) cells. Importantly, viability tests showed no cytotoxicity, demonstrating good biocompatibility for DiB nanocrystals. After the internalization into HEK cells, I was able to track an externally induced modification to cellular pH, demonstrating for the first time a single particle, fully inorganic ratiometric pH sensor based on a dual color emitting structure.

Part I

WS_2 PHOTONIC CRYSTALS

TMD PHOTONICS - AN OVERVIEW

All the work presented in the first part of this thesis was performed at the Molecular Foundry, user facility of Lawrence Berkeley National Laboratory in Berkeley, California (USA).

The invention of the laser in 1960 gave rise to the field of photonics. Since then, materials and techniques to control, handle and exploit the flow of light have been in the focus of research because of the extremely important ramifications in a vast number of technological applications. In recent times, interest in photonics arises from the approaching limit of Moore's Law and the steady shrinkage of electronic devices, that pose a serious technological problem on the semiconductor industry. Photonic materials have also wide interest for renewable energy applications, because they allow to handle the solar spectrum in order to reduce losses and increase device efficiencies. Moreover, with quantum information on the rise, the need for efficient and reliable photonic circuits has never been higher.

Photonic band gap materials as photonic crystals (PCs) are widely studied for their promising applicability to a range of technologies that span quantum information, optoelectronics, photovoltaics, LED and laser illumination, and sensors. Therefore, they can be applied to tackle issues in a large number of extremely demanding and interesting fields. PCs are characterized by a periodic array of materials with different refractive index (n). Photons interacting with a PC experience a bandstructure, and in some cases a bandgap, that are due to the alternating n, and are analogous to those experienced by electrons in a "classical" crystal as Silicon. Therefore, as we can handle electrons in classical crystals to make devices, PCs allow for the fabrication of photonic structures such as waveguides, perfect mirrors and beam-splitters, lossless fibers and more complex devices such as distributed feedback (DFB) lasers.

Research on PCs started in the early 1990s. Due to fabrication challenges, early research was mostly theoretical, while the first fabricated PCs worked in the microwave region of the electromagnetic spectrum because of their centimeter-scale periodicity. The evolution of micro- and nanofabrication techniques gave researchers the tools to fabricate PCs operating at increasingly shorter wavelengths, but the fabrication of PCs for visible light is still challenging because of the lack of both materials and techniques to fabricate efficient devices based on high n contrast. The majority of materials for PCs is indeed limited in one of the two most important features that are needed for photonics, i.e. i) high n and ii) fabrication simplicity. In general, very high n materials (as GaAs) are fabricatable to high resolutions only with great effort, while fabricatable materials (as TiO_2) possess an unsatisfactory n. It is therefore of great interest to find a class of materials that will combine a simple, high resolution and reproducible processability with an extremely high n. Transition metal dichalcogenides (TMDs) may be those who will solve this problem. They have a surprisingly high $n > 3$ through the visible and near-infrared spectrum, making them promising for mid- and short-wavelength PCs. However, the direct fabrication of TMDs is still challenging: the production of TMD-based PCs is limited by complex chemical interactions in high-resolution etching, which reduce the resolution or completely destroy the material.

Herein, we propose a way to go around this limitation, motivated by the fact that TMDs can be synthesized by converting the corresponding transition metal oxide (TMO) in presence of a chalcogenizing agent as sulfur or H_2S. TMOs are in general quite easy to process because they have simple and well-known chemistry. Our method consists in performing every fabrication process on a TMO, a material that is easily etchable with extremely high resolution, control and reproducibility, and with already estabilished processes. To grow the TMO film, we used atomic layer deposition (ALD), which is a powerful thin-film growth technique that not only allows for sub-monolayer control on thickness and for almost perfect stoichiometry, but also for conformal growth on virtually any substrate, and on extremely high aspect ratios. After the fabrication of a TMO-based PC, we converted the oxide to the corresponding TMD by exposing it to H_2S at high temperatures in a tube furnace. Therefore, we prevented issues posed by the complex chemistry of TMDs and we were able to produce TMD-based photonic devices with low effort. We fabricated TMD-based PCs following two different approaches: i) directly etching of holes in a thin film to produce a 2D slab and ii) conformally coating a pre-fabricated, low n PC. The second approach is possible only because we used ALD to grow the TMO film: no other deposition technique gives the same degree of con-

formal coating that is permitted by ALD. Both fabricated PCs showed intense resonances, due to the high n of the TMD. Those resonances can be modulated by changing design parameters, thickness of the material and light incidence angle. Therefore, we demonstrated that TMDs are promising materials for the development of PCs because of their high n, which is combined with fabrication processes that, though not direct, can be done with a series of simple and well-estabilished steps. With more than 60 TMDs to choose from, we believe that the process we demonstrated could be a significant step forward towards the fabrication of PCs working in the visible and near-infrared.

1

PHOTONIC CRYSTALS

A photonic crystal (PC) is a periodic structure composed by materials with different refractive index (n). This periodicity can be in one, two or all three spatial directions to yield 1D, 2D and 3D PCs, respectively (see Figure 1). Light interacting with the PC experiences a bandstructure that is completely equivalent to that affecting the behavior of electrons in a "classical" crystal. This bandstructure may exibit a bandgap that forbids the propagation of incident photons in a specific direction. Thus, PCs are extremely important structures because they allow for light control and manipulation in a wide range of technological applications. PCs properties are strongly dependent on the quality of the composing materials and of the fabrication process. Therefore, there is a strong push for the development of high n materials for the application to PCs. Moreover, there are serious efforts for the improvement of high resolution fabrication techniques to fabricate PCs with small features, interesting for visible light applications.

1.1 A THEORETICAL OUTLINE

The derivations presented in this section were drawn and adapted from John D. Joannopoulos's book "Photonic Crystals. Molding the flow of light"[1].

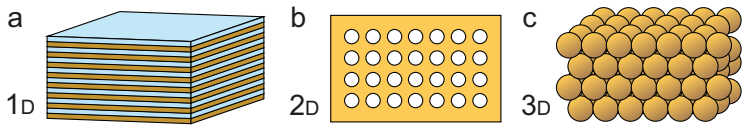

Figure 1: Examples of differerent dimensional PCs. a) 1D PC composed of alternating layers of a high (yellow) and a low (blue) index material. b) 2D PC composed of a rectangular array of holes etched into a high index material. c) 3D PC composed of a self-assembled structure of high index beads.

The study of PCs can be considered as the study of the behavior of electromagnetic fields in a periodic media. All electromagnetic phenomena can be described by Maxwell's equations, which can be written in their local form:

$$\nabla \cdot \mathbf{B} = 0 \tag{1}$$
$$\nabla \cdot \mathbf{D} = \rho \tag{2}$$
$$\nabla \times \mathbf{E} + \frac{\partial \mathbf{B}}{\partial t} = 0 \tag{3}$$
$$\nabla \times \mathbf{H} - \frac{\partial \mathbf{D}}{\partial t} = \mathbf{J}, \tag{4}$$

where $\mathbf{E}$ and $\mathbf{H}$ are the macroscopic electric and magnetic fields, $\mathbf{D}$ and $\mathbf{B}$ are the displacement and magnetic induction fields, and ρ and $\mathbf{J}$ are the free charge and current densities, respectively. In a dielectric medium with no charges or current, we can set ρ and $\mathbf{J} = 0$. It is possible to relate $\mathbf{D}$ to $\mathbf{E}$ and $\mathbf{B}$ to $\mathbf{H}$; in general this is done with power series[2]: For instance, in case of the electic field:

$$\frac{\mathbf{D_i}}{\varepsilon_0} = \sum_j \varepsilon_{ij} \mathbf{E}_j + \sum_{j,k} \chi_{ijk} \mathbf{E}_j \mathbf{E}_k + O(\mathbf{E}^3), \tag{5}$$

where ε_0 is the vacuum permettivity. Equation 5 can be simplyfied with some assumptions. First, it is possible to consider small field strenghts, i.e. linear regime, where the higher order terms can be neglected. Then, the material can be considered macroscopic and isotropic, so $\mathbf{D} = \varepsilon_0 \varepsilon(\mathbf{r}, \omega)\mathbf{E}(\mathbf{r}, \omega)$, where $\varepsilon(\mathbf{r}, \omega)$ is the relative permettivity of the material. Third, we ignore any explicit frequency dependence (material dispersion) of the dielectric constant by considering the value of the dielectric constant appropriate to the frequency range of the physical system. Finally, the material can be considered non absorbing, i.e. $\varepsilon(\mathbf{r}, \omega) > 0$ and real. Assuming these four approximations to be valid, we obtain $\mathbf{D}(\mathbf{r}) = \varepsilon_0 \varepsilon(\mathbf{r})\mathbf{E}(\mathbf{r})$, and a similar equation that relates $\mathbf{B}$ and $\mathbf{H}$, where instead of the permettivity ε we find the permeability μ (for most materials, $\mu_r \simeq 1$, therefore $\varepsilon = n^2$). With the assumptions above, Equations 1-4 become:

$$\nabla \cdot \mathbf{H}(\mathbf{r}, t) = 0 \tag{6}$$
$$\nabla \cdot [\varepsilon(\mathbf{r})\mathbf{E}(\mathbf{r}, t)] = 0 \tag{7}$$
$$\nabla \times \mathbf{E}(\mathbf{r}, t) + \mu_0 \frac{\partial \mathbf{H}(\mathbf{r}, t)}{\partial t} = 0 \tag{8}$$
$$\nabla \times \mathbf{H}(\mathbf{r}, t) - \varepsilon_0 \varepsilon_r \frac{\partial \mathbf{E}(\mathbf{r}, t)}{\partial t} = 0. \tag{9}$$

We consider the functional form of $\mathbf{E}$ and $\mathbf{H}$ a sinusoidal function. Since Maxwell's equations are linear, it is possible to separate time and space dependence by writing:

$$\mathbf{H}(\mathbf{r}, t) = \mathbf{H}(\mathbf{r})e^{-i\omega t} \tag{10}$$

$$\mathbf{E}(\mathbf{r}, t) = \mathbf{E}(\mathbf{r})e^{-i\omega t}. \tag{11}$$

By inserting Equations 10 and 11 into Equations 6-9 we have:

$$\nabla \cdot \mathbf{H}(\mathbf{r}) = 0 \tag{12}$$

$$\nabla \cdot [\varepsilon(\mathbf{r})\mathbf{E}(\mathbf{r})] = 0 \tag{13}$$

$$\nabla \times \mathbf{E}(\mathbf{r}) - i\omega\mu_0\mathbf{H}(\mathbf{r}) = 0 \tag{14}$$

$$\nabla \times \mathbf{H}(\mathbf{r}) + i\omega\varepsilon_0\varepsilon_r\mathbf{E}(\mathbf{r}) = 0. \tag{15}$$

Equations 12 and 13 say that there are no charges or sinks of displacements and magnetic field. With some math, it is possible to decouple Equations 14 and 15 in order to obtain equations only in $\mathbf{H}$ and $\mathbf{E}$, respectively. By considering the speed of light $c = 1/\sqrt{\varepsilon_0\mu_0}$, we obtain the so-called *master equation*:

$$\nabla \times \left(\frac{1}{\varepsilon(\mathbf{r})}\nabla \times \mathbf{H}(\mathbf{r})\right) = \left(\frac{\omega}{c}\right)^2 \mathbf{H}(\mathbf{r}). \tag{16}$$

Equation 16 allows for the calculation of the electromagnetic modes with the corresponding frequencies for a given structure, expressed by $\varepsilon(\mathbf{r})$. The electric field $\mathbf{E}(\mathbf{r})$ can be then obtained by inverting Equation 15:

$$\mathbf{E}(\mathbf{r}) = \frac{i}{\omega\varepsilon_0\varepsilon(\mathbf{r})}\nabla \times \mathbf{H}(\mathbf{r}). \tag{17}$$

It should be noted that Equation 16 can be expressed as an eigenvalue problem:

$$\hat{\Theta}\mathbf{H}(\mathbf{r}) = \left(\frac{\omega}{c}\right)^2 \mathbf{H}(\mathbf{r}), \tag{18}$$

where the operator $\hat{\Theta} = \nabla \times \left(\frac{1}{\varepsilon(\mathbf{r})}\nabla\times\right)$ acts on the eigenfunction $\mathbf{H}(\mathbf{r})$ with eigenvalues $\left(\frac{\omega}{c}\right)^2$. Interestingly, it can be proven that $\hat{\Theta}$ is Hermitian and positive-semi definite, i.e. that the eigenvalues $\left(\frac{\omega}{c}\right)^2$ must be real and non-negative. It is possible to roughly compare the operator $\hat{\Theta}$ in Equation 18 with the Schrödinger Hamiltonian, estabilishing a link between quantum mechanics and electrodynamics. In this comparison, the two curls correspond to the kinetic energy term, while $1/\varepsilon$ is linked

to the potential. However, it should be noted that while in quantum mechanics the Schrödinger equation is separable, in electrodynamics the master equation is not. Therefore, while it is sometimes possible to have analytical solutions for the first, solving the latter is in general more complicated and requires the use of numerical and computational methods.

Now, we want to describe the solution of Maxwell's equations in a PC. To do so, it is necessary to consider periodicity. This can be done by introducing the appropriate symmetry operators. For instance, we can consider translational symmetry, that can be expressed by an operator $\hat{T}_d$ such that:

$$\hat{T}_d e^{ikz} = e^{ik(z-d)} = e^{-ikd} e^{ikz}. \tag{19}$$

This is the case of *continuous translational symmetry*, where each eigenfunction e^{ikz} is invariant under translation. Each eigenfunction can be classified by a particular quantity that determines the eigenvalues, i.e. the wave vector k. It is possible to show that in a homogeneous medium, i.e. where continuous translational symmetry is valid, the modes have the form:

$$\mathbf{H}_k(\mathbf{r}) = \mathbf{H}_0 e^{i\mathbf{k}\cdot\mathbf{r}}. \tag{20}$$

Those reported in Equation 20 are plane waves that satisfy the master equation with eigenvalues $\left(\frac{\omega}{c}\right)^2 = \frac{|\mathbf{k}|^2}{\varepsilon}$, that gives the *dispersion relation* $\omega = \frac{c|\mathbf{k}|}{\sqrt{\varepsilon}}$. It is possible to label each mode with a different k with a number n that we define *band number* in such a way that each mode can be identified by (k, n). In general n is a continuous variable, but if the spectrum is discrete for k it can assume discrete values. The value for n grows with the frequency of the modes: a plot of k versus ω shows different lines that correspond to different solutions of the dispersion relation. Each solution is labeled by a different n: this plot is named a *bandstructure*. In a homogeneous, infinite medium, the spectrum for n is continuous, therefore there are no discrete lines. In some cases, when the symmetry breaks as in a infinite slab of dielectric, there are regions where the bands are discrete.

However, a PC is not a structure where the assumption of continuous translational symmetry is valid. Therefore, we have to consider *discrete translational symmetry*, which means that the system is invariant under a transformation that is a multiple of a definite step, determined by the *lattice constant* a. This is the case of a PC. Considering a 1-dimensional case, the unit step can be defined as the *primitive lattice*

vector $\mathbf{a} = a\hat{\mathbf{x}}$. In our case, this translates in a periodic dielectric function $\varepsilon(\mathbf{r}) = \varepsilon(\mathbf{r}+\mathbf{a}) = \varepsilon(\mathbf{r}+\mathbf{R})$, for any integer multiple of $\mathbf{a}$, $\mathbf{R} = l\mathbf{a}$. Therefore, we can express the discrete translational operator $\hat{T}_{\mathbf{R}}$ with a similar expression as the one reported in Equation 19:

$$\hat{T}_{\mathbf{R}} e^{ik_x x} = e^{ik_x(x-la)} = e^{-ik_x la} e^{ik_x x}. \tag{21}$$

Not every different value of k_x yields a different eigenvalue: it is easy to calculate that, for instance, k_x and $k_x + \frac{2\pi}{a}$ give the same solution. This is true for all $k_x + m\frac{2\pi}{a}$, with m integer. All those solutions are degenerate and we can define $b = \frac{2\pi}{a}$; $\mathbf{b} = b\mathbf{x}$ is defined a *primitive lattice vector*. We express the modes of the system, that are solutions of Equation 21 as a linear combination of the $e^{ik_x x}$:

$$\mathbf{H}_{k_x}(\mathbf{r}) = \sum_m \mathbf{c}_{k_x,m} e^{i(k_x+mb)x} \tag{22}$$

$$= e^{ik_x x} \sum_m \mathbf{c}_{k_x,m} e^{imbx} \tag{23}$$

$$= e^{ik_x x} \mathbf{u}_{k_x}(x). \tag{24}$$

Equation 24 says that the modes $\mathbf{H}$ are composed of a plane wave that is modulated by a periodic function. This result is the *Bloch's theorem*, which is completely analogous to the "solid-state-physics-textbook" one that expresses the behavior of electrons in a crystal composed of a periodic array of atoms. The nonreduntant area where all the k_x are unique is called the Brillouin zone:

$$-\frac{\pi}{a} < k_x \leqslant \frac{\pi}{a}. \tag{25}$$

It is now possible to generalize Bloch's theorem to a 3-dimensional case. After some math, we obtain:

$$\mathbf{H}_{\mathbf{k}}(\mathbf{r}) = e^{i\mathbf{k}\cdot\mathbf{r}} \mathbf{u}_{\mathbf{k}}(\mathbf{r}), \tag{26}$$

where the periodic function $\mathbf{u}_{\mathbf{k}}(\mathbf{r}) = \mathbf{u}_{\mathbf{k}}(\mathbf{r}+\mathbf{R})$. Therefore, electromagnetic modes of a 3D periodic array of dielectric constant, i.e. of a 3D PC, can be written as Bloch states. Every mode is defined by the wave

vector $\mathbf{k}$ and by the periodic function $\mathbf{u}$. It is possible to insert the mode, as in 26, into the master equation 16 to obtain a solution for $\mathbf{u}$:

$$\hat{\Theta}\mathbf{H}_{\mathbf{k}} = \left(\frac{\omega(\mathbf{k})}{c}\right)^2 \mathbf{H}_{\mathbf{k}} \tag{27}$$

$$\nabla \times \frac{1}{\varepsilon(\mathbf{r})} \nabla \times e^{i\mathbf{k}\cdot\mathbf{r}} \mathbf{u}_{\mathbf{k}}(\mathbf{r}) = \left(\frac{\omega(\mathbf{k})}{c}\right)^2 e^{i\mathbf{k}\cdot\mathbf{r}} \mathbf{u}_{\mathbf{k}}(\mathbf{r}) \tag{28}$$

$$(i\mathbf{k} + \nabla) \times \frac{1}{\varepsilon(\mathbf{r})} (i\mathbf{k} + \nabla) \times \mathbf{u}_{\mathbf{k}}(\mathbf{r}) = \left(\frac{\omega(\mathbf{k})}{c}\right)^2 \mathbf{u}_{\mathbf{k}}(\mathbf{r}) \tag{29}$$

$$\hat{\Theta}_{\mathbf{k}} \mathbf{u}_{\mathbf{k}}(\mathbf{r}) = \left(\frac{\omega(\mathbf{k})}{c}\right)^2 \mathbf{u}_{\mathbf{k}}(\mathbf{r}). \tag{30}$$

The periodicity allows the eigenvalue problem to be solved only in a single repeating unit of the PC, i.e. the *unit cell*. A general property of Hermitian operators states that restricting a Hermitian eigenvalue problem to a finite volume leads to a discrete spectrum of eigenvalues (one famous example is the particle-in-a-box problem). Therefore, for each k exists an infinite set of discretely spaced ω that can be labeled by a band index n, as in the case of a continuous translational symmetry that was discussed above. Since k is a continuous variable, ω varies continuously with k for a given n. The family of $\omega_n(k)$ is the *bandstructure* of the PC, a simple example of which is given in Figure 2.

Photonic bandstructures can present a bandgap, that is a frequency region where no mode can propagate, regardless of its wave vector. In Figure 2 the simplyfied bandstructure of three different multilayer films, i.e. 1D PCs, are reported. In a homogeneous medium an arbitrary periodicity can be set (similarly to the "empty lattice" approximation of a potential in solids). In this case, the modes are represented by the dispersion equation $\omega(k) = \frac{ck}{\sqrt{\varepsilon}}$, the so-called *light line*. Something interesting happens when an dielectric constant contrast is introduced: a small gap appears at the intersection of the dispersion curves. There is no allowed mode in the crystal that has a frequency within this range, that is called the *photonic bandgap*. The gap widens considerably as the dielectric contrast is increased. The physical origin of the bandgap can be understood by considering mode profiles for the states immediately above and below the gap, that are represented in the bottom part of Figure 2. The gap between bands 1 and 2 occurs at the edge of the Brillouin zone. Symmetry constraints determine that there are only two ways for a mode to propagate in this configuration: i) with the nodes in the low-ε layers or ii) with nodes in the high-ε layer. Low-frequency modes concentrate their energy in the high-ε regions, while high-frequency modes are more concentrated in the low-ε regions. This determines the frequency difference between the bands, i.e. the photonic bandgap.

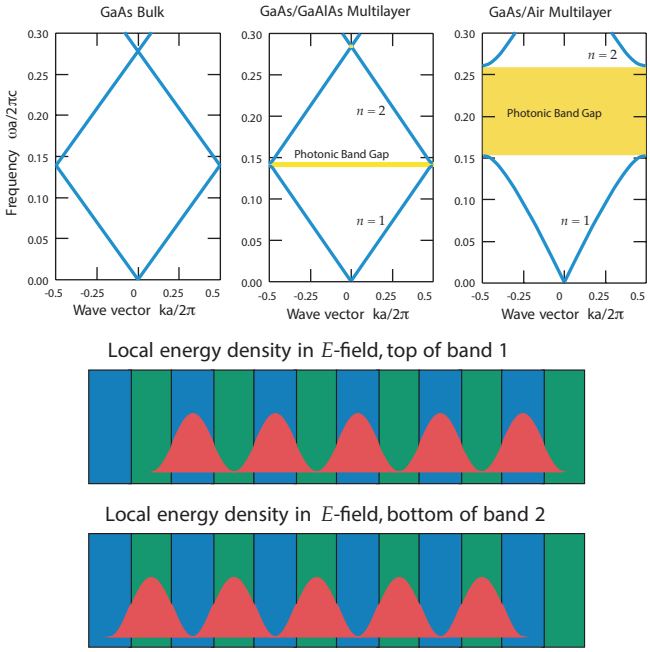

Figure 2: Schematic of a photonic bandgap. Photonic band structures for a 1D PC computed with three different multilayer films. Top-left: every layer has the same dielectric constant $\varepsilon = 13$. Top-center: layers alternate between ε of 13 and 12. Top-right: layers alternate between ε of 13 and 1. A photonic bandgap appears when a dielectric constant contrast is present. Bottom-side: electric-field energy density of band 1 and 2. The blue layers are the regions with high dielectric constant.

The mode just under the gap has more of its energy concentrated in the high-ε regions, giving it a lower frequency than the next band, most of whose energy is in the high-ε region.

Scaling Invariance

An interesting property of electromagnetism is that it presents no fundamental length scale. For PCs, this translates into the fact that the master equation is scale invariant. This can be proven by considering a solution to the master equation $\mathbf{H}(\mathbf{r})$ with frequency ω in a PC described by a dielectric configuration $\varepsilon(\mathbf{r})$. A compression or expansion of $\varepsilon(\mathbf{r})$ by a factor s yields a new dielectric configuration $\varepsilon'(\mathbf{r}) = \varepsilon\left(\frac{\mathbf{r}}{s}\right)$. We can rewrite the master equation (Equation 16) with the new dielectric configuration:

$$s\nabla' \times \left(\frac{1}{\varepsilon\left(\frac{\mathbf{r}'}{s}\right)} s\nabla' \times \mathbf{H}\left(\frac{\mathbf{r}'}{s}\right) \right) = \left(\frac{\omega}{c}\right)^2 \mathbf{H}\left(\frac{\mathbf{r}'}{s}\right), \tag{31}$$

where we performed a change of variables $\mathbf{r}' = s\mathbf{r}$ and $\nabla' = \frac{\nabla}{s}$. It should be noted that $\varepsilon'\left(\frac{\mathbf{r}'}{s}\right) = \varepsilon'(\mathbf{r}')$. Therefore, dividing by s, Equation 31 can be re-written as:

$$\nabla' \times \left(\frac{1}{\varepsilon'(\mathbf{r}')} \nabla' \times \mathbf{H}\left(\frac{\mathbf{r}'}{s}\right) \right) = \left(\frac{\omega}{cs}\right)^2 \mathbf{H}\left(\frac{\mathbf{r}'}{s}\right). \tag{32}$$

Equation 32 is the master equation with a mode profile $\mathbf{H}'(\mathbf{r}') = \mathbf{H}\left(\frac{\mathbf{r}'}{s}\right)$ and a corresponding frequency $\omega' = \frac{\omega}{s}$. This means that the new mode profile $\mathbf{H}'$ and frequency ω' can be obtained by simply rescaling the old mode profile and its frequency. Therefore, solving the problem in one length scale allows to consider the same functional form for every other scale. This property is of considerable importance for the fabrication of PCs of increasingly smaller size, as will be reported in the historical notes in Section 1.2.

Scaling invariance affects not only the dimensionality of PCs, but also the dielectric constant. By considering a new dielectric constant $\varepsilon'(\mathbf{r}) = \frac{\varepsilon(\mathbf{r})}{s^2}$ and performing the change of variables $s^2\varepsilon'(\mathbf{r}) = \varepsilon(\mathbf{r})$, the master equation becomes:

$$\nabla \times \left(\frac{1}{\varepsilon'(\mathbf{r})} \nabla \times \mathbf{H}(\mathbf{r}) \right) = \left(\frac{s\omega}{c}\right)^2 \mathbf{H}(\mathbf{r}). \tag{33}$$

The solutions of the new system are not changed, while the new frequencies are scaled by a factor s. Therefore, changing the dielectric

constant by s^2 and rescaling the coordinates by s leaves the solutions unchanged.

Dielectric constant and refractive index

Until now, we have been talking about the dielectric constant ε of a material. However, it is common to find, mostly in experimental papers, materials for PCs classified on their refractive index n. In this section, we highlight the relationship between the complex dielectric constant and the complex refractive index of a material. The dielectric constant ε can be expressed by a real part and an imaginary part:

$$\varepsilon = \varepsilon_1 + i\varepsilon_2. \tag{34}$$

Similarly, the refractive index $\tilde{n}$ can also be expressed as a complex number:

$$\tilde{n} = n + ik, \tag{35}$$

where the real part n is defined as the ratio between the speed of light in the medium and in vacuum, $n = \frac{c}{v}$, while the complex part k is called the extinction coefficient and takes into account light absorption. k is related to the attenuation coefficient $\alpha = \frac{4\pi k}{\lambda}$ and to the absorbance of a material $A = \alpha l$. For transparent materials k and ε_2 are zero, therefore the real part of refractive index and dielectric constants are related by $n^2 = \varepsilon_1$. We can extend the equality to the complex quantities to take into account also absorbing materials:

$$(n + ik)^2 = \varepsilon_1 + i\varepsilon_2. \tag{36}$$

It follows that:

$$\varepsilon_1 = n^2 - k^2 \tag{37}$$

$$\varepsilon_2 = 2nk. \tag{38}$$

From now on, we will be talking about refractive index, and not dielectric constant, when discussing about materials for photonics.

1.2 HISTORY AND STATE OF THE ART

PCs are widely present in nature. Several examples can be found of animals with iridescent color that is determined not by pigments, but by microstructured surfaces as feathers and scales (*stuctural color*). Examples of structural coloration[3] are found in butterflies[4], beetles[5,6], cephalopods[7], birds[8], and plants[9]. PCs are also found in minerals as

in opals, hydrated silicates composed of hundreds-of-nanometer sized SiO_2 spheres in hexagonal close packed (*hcp*) lattice[10,11]. The opaline structure diffracts light and gives the typical iridescent coloration, also known as *opalescence*.

Synthetic PCs have been known since 1888, when Lord Rayleigh observed increased reflectivity in multi-layer dielectric stacks[12]. What Rayleigh observed was what now we would call a photonic band-gap in a 1D PC, also known as Bragg mirror. However, at Rayleigh's time the theoretical structure for the study of PCs did not exist: almost 40 years had to pass for Schrodinger to formulate his equation, giving rise to quantum mechanics and, ultimately, solid state physics. Therefore, after Rayleigh's observation of a photonic bandgap, PCs were not considered until 100 years later. In 1987, Eli Yablonovitch[13] and Sajeev John[14] published two independent papers where they considered the effect of a periodic dielectric structure on photophysical parameters of matter. In his paper, Yablonovitch considered PCs in order to inhibit spontaneous emission of materials, while John aimed to change light localization and performed the first modeling of a photonic bandstructure. Therefore, Yablonovitch and John had different goals, but they both considered PCs as promising tools for light control. Their work reopened the field of PCs, but this time there was all the necessary to build a solid theoretical structure. In the first years, the majority of research on PCs was theoretical because of the challenges that were found in fabrication, in particular at optical scales, i.e. in sizes around 500 nm. However, the scaling invariance properties for PCs described in Section 1.1 allowed to tackle this issue. Models could be made and tested in the microwave regime, at the much larger length scale of centimeters. Scaling invariance guarantees that the centimeter-scaled model has the same properties if shrinked to submicron-scale. Therefore, a PC with a $\sim$ 500 nm periodicity has solutions with the same functional form of a PC of the same geometry, but with $\sim$ 5 cm periodicity. What changes are the frequencies, that are different by a factor 10^5. Therefore, the first PCs were built to work in the microwaves because fabrication processes were more accessible.
In 1991 Yablonovitch's group fabricated the first 3D PC showing a full photonic bandgap in the microwave range by drilling holes in a dielectric material to obtain the structure that now is named *Yablonovite*[15]. The first PC working at optical wavelengths was fabricated by Thomas Krauss in 1996[16] and it was a 2D slab. This remarkable result opened research on 2D PCs, which have an enormous advantage with respect to their 3D counterparts: fabrication processes for 2D PCs are more compatible with the ones used by the semiconductor industry. For instance, techniques like lithography and etching are well known and extremely

diffuse in micro- and nano-electronics and are also used in the fabrication of PCs. Therefore, still nowadays the most studied and characterized PCs are 2D structures. A wide range of applications appreared for 2D PCs, from waveguides and PC fibers to cavities and photonic circuits. However, while more complex to fabricate, 3D PCs show great potential and many different approaches have been proposed to obtain a complete photonic bandgap in the visible. In addition to Yablonovite, other 3D PCs are self-assembled synthetic opals made of polymer or silica beads and inverse opals that are fabricated by coating or infiltrating opals with a high n material and then removing the templating beads[17–20]; woodpile PCs fabricated by several lithography and etching steps[21,22]; more complex strategies are also being followed, as for instance using 3D holographic lithography[23–25]. Each of the listed structures has some advantages and some limitations. Historically, the first 3D PC with a complete bandgap in the visible was fabricated in 2000 by Noda and co-workers[26] and was an inverse opal. Opals and inverse opals are, moreover, easier to fabricate because they are the product of a self assembly process that can be easily directed and controlled.
Nowadays, PCs have broad application in a wide number of fields. Some of them, with relevant examples, are listed below.

Spontaneous Radiation Management

The property of PCs to change, inhibit or enhance the spontaneous emission rate of materials has been known since Yablonovitch's work in 1987[13] and plays an important role for the design of PC-based light sources. Basically, an emitter's spontaneous emission rate will change depending on the features of the PC. For instance, if a PC is designed such as a given frequency mode can not propagate, an emitter embedded in the PC will have its spontaneous decay rate drastically reduced (and vice-versa in the opposite case, where the PC is designed for a mode to propagate).

Photonic Crystal Light Sources

PCs can be used to increase the efficiency and to lower the threshold current of semiconductor lasers and LEDs[27–29]. Moreover, there are different strategies to fabricate PC-based lasers. Distributed Feedback (DFB) lasers[30–33] have a diffraction grating (Bragg reflector) on top of the active medium. The grating reflects only a narrow band of wavelenghts, allowing the propagation of a single lasing mode. Another approach is that of high-Q resonators or cavities fabricated into a PC. The laser can be fabricated such that the reflectance is maximized for

the lasing wavelength, greatly increasing efficiency with respect to classical mirror reflectors[34–37].

Optical Insulation

The use of PCs as optical insulators is allowed by the possibility to localize light inside a defect in a periodic structure. This defect can assume various forms based on the scope. Generally, the defect can be a variation of the geometric parameters of the PC or the removal of the periodicity: for example, in a 2D PC made of holes in a dielectric film, the removal of a row of holes will act as a line defect. For instance, a 0D defect will act as a cavity[34,38–40], while a 1D defect will be a waveguide[40–43]. The perfect reflectivity of PCs allows waveguides to have virtually no losses, in contrast to planar waveguides that are based on total internal reflection. It is worth noting that extremely efficient photonic circuits can be obtained bu designing high n waveguides[44–46]However, PC waveguides are generally more efficient and compact. Moreover, one of the unique PC waveguide properties is the possibility to form very sharp bends with almost no loss of signal. It is possible to form bends at extremely sharp angles[47,48] that can be larger than 90°. Complex defects in PCs allow for the formation of passive optical circuitry elements as splitters, couplers and combiners other than the already discussed waveguides and cavities.

Nonlinear Effects for Optical Circuitry

Nonlinear PCs[49–51] are based on the optical Kerr effect, i.e. the variation of polarizability of a material as a function of light irradiance (it is different from the electro-optical Kerr effect, where the dependence is on the electric field intensity). This change in polarizability, thus in n, can give rise to interesting applications such as optical memories and storage elements[52,53], logical elements[54], optical switches[55,56] and optical power limiters[57]. Complex active circuitry elements will be of great interest for the development of photonic-based quantum computing[58–60], that is one of the greatest challenges of current research.
On a side note, another exceptional effect given by n nonlinearity is supercontinuum generation[61]: when ultrashort, high-energy pulses travel through a nonlinear material, their frequency spectrum can experience giant broadening due to a range of interconnected nonlinear effects. As a result, it is possible to generate a extremely broad spectrum with the same repetition rate of an excitation laser, that in general is a 800 nm Ti:Sapphire (the repetition rate is $\sim$ 13 ns). Supercontinuum generation

is a powerful tool for spectroscopist, because it allows ultrafast excitation on virtually any wavelength in the visible spectrum.

Optical Coatings

PCs can be used to coat surfaces, in order to increase or diminish light transmission efficiency. For instance, PCs used as back reflectors in solar cells have been shown to increase the optical path of light inside the active medium, sensibly increasing power conversion efficiency[62,63]. On the other hand, periodically patterned surfaces can also increase the light transmission ability of a surface. Antireflective coatings[64] are used in a large number of applications as lenses, eyeglasses, lasers, mirrors, photovoltaic cells, filters, screens, sensors, cameras, and many more.

Structural Color

As reported above, PCs are diffuse in nature as structural colorants[3]. Synthetic structural color materials have attracted interest for their applications in optical filtering and sensors[65] and in biomimetics[66]. Moreover, structural colored materials can be designed to be superhydrophobic[67] or superhydrophilic[68], and can also be fabricated with self-cleaning materials as TiO_2[69]. Those are all effects determined by a selective patterning of a surface with hydrophobic or hydrophilic materials, and of enhanced surface area that increases reactivity.

Metamaterials

Metamaterials and negative n materials have recently attracted interest of research for their interest to many different applications. A metamaterial is not composed of a single material with $n<0$, but it is a complex nanostructured system, much smaller than the wavelength of light so it behaves like a continuum, that overall behaves like it has a negative n[70]. For instance, a typical effect that yields a negative n is the appearance of surface waves in photonic structures, that yield a combined photonic and plasmonic behavior in the surface wave. This effect has been detected in 2D slabs[71] and in 3D structures[72]. Applications of metamaterials span optical cloaking[73], superlenses for sub-diffraction imaging[72,74], lab-on-a-chip with lossless light transmission[75] and more[76].

Sensors

PC-based sensors allow to detect an analyte because it brings a perturbation in the periodic n structure. For instance, the presence of a sub-

stance inside a PC changes the light-matter interaction, influencing the mode frequencies and allowing for chemical sensing[77]. Another type of PC sensor is based on polymeric PCs that are subject to swelling when interacting with analytes. Examples are 3D polymeric PCs where intercalation of ions causes the change in the lattice constant, therefore in the reflectance, allowing sensing of pH and ions[78], and bragg stacks composed of swellable polymers and inorganic materials allowing sensing of molecules as water[79].

The brief list of applications presented above is a demonstration that PCs have great interest in many fields of science and technology. A common request for all of those is that materials for PCs need a high n, irrespective of the field of application. Currently, the main focus of research on PCs is the increase of the efficiency and the development of high n materials working in the visible.

1.3 MATERIALS FOR PHOTONIC CRYSTALS

The ideal material for PCs has to be easily fabricatable with good resolution and with well-known, non-complex processes. Moreover, it needs a n as high as possible to increase index contrast, i.e. efficiency, and a negligible k to avoid absorption losses in the working range. A material that meets all the aforementioned requirements is silicon[80–83]. Thanks to a incredibly high n[84] > 3.5, silicon can be used to produce highly efficient PCs which operate in the near-infrared (NIR). Moreover, processes for silicon are extremely well known and it is possible to deposit, etch and fabricate it with extreme precision and control. The major drawback for the application of Si to PCs is its low energy gap, meaning that k and therefore light absorption are not negligible for wavelengths shorter than ~1000 nm. Therefore, Si-based PCs, while extremely efficient, cannot be applied to devices working in the visible. This is quite a strong limitation: the progressive shrinkage of electronic and photonic devices determines a dimension reduction for every component, and since the bandgap of a PC is proportional to the periodicity of the PC itself, a shorter periodicity reduces the operating wavelength range of the device from, for instance, the NIR to the visible. Therefore, it is necessary to find other materials that have all the good qualities of Si but can work in a shorter wavelength range.

The most used materials for PCs are transition metal oxides (TMOs) as TiO_2[19,85–87], Al_2O_3[88], ZnO[89], CeO_2[18], and other oxides as SiO_2[90,91]. The great advantage of TMOs is that they are very easy to fabricate. Etching processes are well known and can be controlled with extreme

precision. Moreover, TMO-based PCs can be efficiently fabricated with numerous techniques as lithography, chemical vapor deposition, atomic layer deposition, infiltration of 3D opaline structures, micro- and nano-imprinting, and focused-ion beam. The popularity of TMOs arises from the fact that they combine the high fabricability with excellent absorption properties. Typical TMOs have a high energy gap that can be ~ 3, and therefore they are completely transparent in a spectral range that spans all the visible and can extend to the UV-A. Therefore, TMO-based PCs can be fabricated for visible light applications and with small periodicity, compatible with the reduction of size in electronic devices. However, the downside for TMO photonics derives from the low n of the most common materials. It is indeed extremely unlikely to synthesize a TMO with a n higher than 2.5, meaning that the index contrast is still not satisfactory for the fabrication of complete-photonic bandgap PCs working in the visible. While this could be a very strong limitation, it is possible to design TMO-PCs with a complete bandgap. However, the progressive shrinkage of devices poses the need for a high n contrast between the media to have both a large photonic bandgap and light confinement in the photonic structure[1,92]. Therefore, high n contrast is always needed to fabricate high efficiency PCs. By considering that in many cases the low n material is air (or vacuum), that has $n \sim 1$, the high n material is the one that determines index contrast. It has been indeed demonstrated that to have a complete photonic bandgap in all 3 spatial dimensions, the index contrast between the media needs to be[20]:

$$\frac{n_{high}}{n_{low}} > 2.8. \tag{39}$$

Therefore, other materials with extremely high n combined with novel fabrication techniques are needed to push forward the production of high index contrast, efficient PCs. Beyond Si and TMOs, other promising materials are III-V and III-nitrides semiconductors, as GaAs and GaN. The intermediate energy gap of those materials allows for applications to devices working in the visible and NIR. The candidacy of III-V and III-nitrides for the fabrication of PCs emerges from the extremely high n in the transparency range. Those materials have n comparable to Si. Therefore, as for Si, the high n allows for efficient devices, but the slightly higher bandgap extends the operativity range of fabricated PCs. Moreover, III-V and III-nitrides are already compatible with semiconductor technology processes, meaning that fabrication of PCs can exploit well known, efficient techniques without the need of developing new ones. All these advantages are however eclipsed by major fabrication challenges, that make III-V PCs very uncommon in the literature and industry. The chemistry of the III and V elements are

quite different and it is extremely complex to etch structures with high resolution, precision and reproducibility. Therefore, while interesting, III-V and III-nitrides are not the best choice of materials for photonics, because the need of facile fabrication processes is at least as important to the need of high n materials.

A possible alternative to all the materials listed above is presented by transition metal dichalcogenides (TMDs). They are well known for their extraordinary optoelectronic properties, but they also present an unusually high n in their transparency region[93]. The energy gap of the most common TMDs, like tungsten and molybdenum disulfides and diselenides (WS_2, WSe_2, MoS_2, $MoSe_2$), is between ~1.2 eV and ~ 2.0 eV for bulk and monolayer, respectively, which makes them very interesting for photonic applications in the NIR[93,94]. Therefore, TMDs belong to a class of materials that could generate extremely high refractive index contrast both in 1D, 2D and 3D PCs. However, as for III-V and III-nitrides, their good optical properties still go against a complex chemistry, which is restrictive for their application to the nanofabrication of photonic structures. The chalcogen chemistry prevents high resolution etching and, therefore, precise and reproducible fabrication in the size range of visible and NIR light (400 to 1000 nm).

Herein, we propose a novel approach for the fabrication of TMD-based PCs motivated by the possibility of converting a TMO to TMD in presence of a calchogenizing agent. Fabrication processes for transition metal oxides are better known, more controllable and less complex with respect to their TMD counterpart. The driving idea for our work is that we can exploit existing processes to fabricate PCs in low-refractive index materials and then convert the structure into a TMD-based PC. In this way it is possible to go around the limitation posed by the complex chemistry and fabricate high n PCs with simple, well known processes. The problems generated by chemistry of high n materials are therefore avoided and essentially any structure can be produced, in a way that would not be possible with direct fabrication methods. The synthetic procedure we are proposing is a step forward in the fabrication of high refractive index contrast PCs, that has always been delayed by the issues placed by the chemistry of high n materials as III-V and III-nitrides semiconductors. Following this route, the production of high-index contrast PCs in a facile and controllable fashion will be possible, going beyond the current limitations and paving a new way for the development of photonic structure for light manipulation.

2

TRANSITION METAL DICHALCOGENIDES

Two-dimensional layered materials (2DLMs) are bulk materials composed of single, weakly interacting one-atomic-layer thick sheets[95]. Each single 2D layer interacts with the nearest neighbors by weak Van der Waals forces and can therefore be separated with no particular effort. Bulk material and single-layer sheet behave in different way: reducing a bulk crystal to a single layer gives rise to a whole new spectrum of remarkable properties that surprised scientists and stimulated research on physics, chemistry and engineering applications of 2DLMs. The most famous 2DLM is graphene, a single layer of graphite composed of carbon atoms in a honeycomb lattice. Its exceptional electronic, optical and mechanical properties have put graphene in the spotlight of research for more than a decade. The majority of 2DLMs share with graphene most of their properties, i.e. excellent optoelectronic properties, remarkable mechanical stability, and extremely high transport mobility. Beyond graphene, other 2DLMs like silicene[96], hexagonal boron nitride[97] (h-BN), black phosphorus[98] and transition metal dichalcogenides are currently intensively studied because they have great potential for a wide spectrum of applications that exploit diverse properties, such as extremely high mobility[99] (graphene), electrical insulation and thermal conductivity[100] (h-BN), superconductivity[101] ($NbSe_2$), remarkable light matter interaction[102] (MoS_2), topological insulation[103] (Bi_2Te_3), and more. 2DLMs are therefore one of the most important classes of materials to date, because of the vast implications they can have in almost every field of science and technology.

Transition metal dichalcogenides (TMDs) are a prominent family of 2DLMs with the chemical formula MX_2, where M is a transition metal, in general from group IV (Ti, Hf), V (V, Nb) or VI (Mo, W) and X is a chalcogen (S, Se and Te). The interest in TMDs arises from the indirect-to-direct band gap transition that occurs when they are reduced from a bulk crystal to a single layer[104,105]. Bulk TMDs have low energy, indirect band gap, but a single, isolated layer has a medium-high energy, direct band gap[106]: single layer TMDs are therefore semiconductors with a remarkably high oscillator strenght. The connection between TMDs

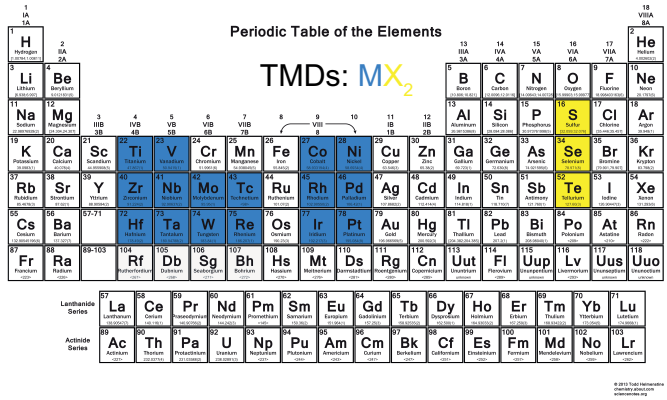

Figure 3: Periodic table, where elements composing TMDs are highlighted. Blue: transition metal; yellow: chalcogen.

and optoelectronics industry is straightforward. However, the exceptional properties of TMDs are not just limited to enhanced light-matter interaction but also include high transport mobility[107], superconductivity[101], and remarkably high refractive index[93]. Therefore, TMDs are extremely promising and versatile materials that can be used in a wide spectrum of applications and can be considered one of the most important classes of 2DLMs.

2.1 HISTORY AND STATE OF THE ART

TMDs have been known since the 1960s for their semiconducting properties[108]. Common knowledge was that a single bulk crystal could be exfoliated to smaller particles down to a size of ~100 nm, where, however, no interesting change in properties occurs. The difficulty of separating single layers has always hindered research on their applications and, since their properties as a bulk are quite ordinary, interest never broke out. Nevertheless, TMDs found several applications in industrial processes as solid lubricants, thanks to the weak interactions between the layers that allowed for low friction[109]. After Geim and Novoselov demonstrated that it is possible to isolate single layers of a bulk material by mechanically exfoliating graphene from graphite in 2004[110], research on 2DLMs had a huge boost. While for some time the most promising and studied material was clearly graphene, even TMDs started to be put again, after almost 40 years, under the spotlight. In a 2010 paper, Splendiani and coworkers demonstrated that the exfoliation of a MoS_2 crystal generated high luminescence efficiency in correspondence to single layers[104]. Bandstructure calculations al-

lowed to show that the multilayer to monolayer transition coincided with a change in the band-gap of the material from indirect to direct[111]. The transition towards a direct bandgap increases oscillator strength, light-matter interaction and absorption and photoluminescence intensities. Moreover, thanks to their intermediate bandgap energy, TMDs attracted a lot of interest for electronics applications because thay can overcome one of the most critical drawbacks of graphene, i.e. the unsatisfying on/off current ratio determined by the lack of a bandgap. The combination of the exceptional optical properties with a quite good electrical mobility legitimates the application of TMDs to a new generation of electronics with unique functions or performances, as transparent and flexible electronics and photovoltaic devices. For instance, a 2011 paper by Radisavljevic and coworkers demonstrated MoS_2 mobility larger than 200 $cm^2V^{-1}s^{-1}$ that allowed for the fabrication a high performance transistors[107] based on MoS_2 showing a on/off current ratio larger than 10^8.

Intense light absorption and high transport mobility are two fundamental conditions for materials to be applied in solar energy technologies. Therefore, TMDs have attracted lots of interest for application to photovoltaic cells and photocatalytic devices[112,113]. Shanmugam and coworkers fabricated a bulk-heterojunction photovoltaic cell composed of TiO_2 nanoparticles conformally coated with an atomic layer of MoS_2 that worked as the active material and poly(3-hexylthio-phene) that showed a photoconversion efficiency of 1.3%[114]. The application of TMDs to photocatalysis, in particular to photoelectrochemical water splitting, looks even more interesting because of the small energy gap of these materials. A photoactivated water splitting reaction needs photons of at least 1.23 eV to occur[115]. This value is in good agreement with the energy gap of monolayer-TMDs as MoS_2 and WS_2, allowing to explit almost all the useful light coming from the sun. This is a great advantage with respect to typical photoelectrodes, made of TMOs like TiO_2 or WO_3 that have a too large bandgap, therefore wasting the majority of incident photons. Moreover, many monolayer-TMDs present the correct offset between their valence and conduction band and the oxidation potential of water and reduction potential of hydrogen, respectively[112]. Therefore, TMDs are extremely powerful materials for water splitting since they combine optimal photoelectrochemical properties with a strong light absorption and transport mobility. There are numerous different approaches to TMD-based water splitting that employ mixed chalcogenides as MoS_xSe_{1-x} or TiO_2/WS_2 composites that allow for high absorption by the TMD layer and efficient transport by the TMO substrate[112].

Another interesting application of TMDs is in the synthesis of vertically aligned heterostructures[116]. Van der Waals interactions between each single TMD layer allow for the fabrication of vertically aligned heterostructures with no need for lattice parameters matching. Moreover, since each layer is distinct and well separated from the others, there is no interdiffusion of atoms and interfaces are atomically sharp. TMD heterostructures can be used in the fabrication of functional devices, such as p-n junctions[117]. The fabrication of a TMD-based diode[118] is extremely complex as far as it is limited to a single layer, because selective doping a single sheet with different dopants is still challenging. However, it is possible to create a TMD p-n junction by vertically stacking differently doped single TMD layers, as for instance p-type WSe_2 and n-type MoS_2[119,120]. By fabricating TMD-TMD heterostructures it is not only possible to fabricate p-n junction based devices as diodes and photovoltaic cells, but also to investigate exciton dynamics and energy transfer processes in novel complex systems. Following this approach, Cheng and coworkers fabricated a p-n diode made of a heterojunction between monolayer p-type WSe_2 and multilayer n-type MoS_2 with an external quantum efficiency (EQE) of about 12%[119]. It is then possible to stretch the concept even further by fabricating all-monolayer heterostructures. By sandwiching a TMD-TMD heterostructure composed of monolayer p-type WSe_2 and monolayer n-type MoS_2 between sheets of graphene, Lee and coworkers were able to fabricate a p-n junction with EQE of 34%[120]. In this example, graphene layers are used as transparent contacts that allow for the extraction and migration of charges from the p-n junction. Wan der Waals heterostructures allow for the fabrication of fully tailorable, extremely efficient devices that exploit single layers for what they are best: for instance, Massicotte and coworkers fabricated a photodetector fully based on weak interactions between its components[121]. In detail, the active layer was WS_2 and was chosen for the exceptional optical absorption properties. The WS_2 layer was sandwiched between graphite electrodes, while the entire structure was isolated with h-BN. The device showed photoresponse of about 5 ps and EQE about 7%.
The brief list of applications reported above demonstrates the potential and the versatility of TMDs, that are increasingly more important as key players in the vast 2DLM field and can be applied in many fields of technology for innovative and efficient devices.

Optical Constants

Another impressive feature of TMDs, though less known and investigated, is their refractive index n that can be extremely high. Liu and

coworkers performed a spectroscopic ellipsometry analysis of the four most studied TMDs, showing that n for both the monolayer and the bulk material that can be as high as 4.25 for $MoSe_2$, 5.7 for WSe_2, 6.25 for WS_2 and 6.5 for MoS_2[122]. Those values are strikingly large, suggesting the application of TMDs to a whole new list of functions, that goes from antireflective coatings[123] to high efficient substrates for luminescent devices[124], to encapsulants for enhancing efficiency of photovolatic cells[125]. Moreover, with more than 60 TMDs, it is likely that other materials can be found with an even larger n with respect to those reported above. However, the feature that is perhaps even more exciting is that n is surprisingly large (~4) even in the spectral region where the material is completely transparent, i.e. where the extinction coefficient k is negligible. This feature is extremely important because it opens a new important field for the application of TMDs: photonics. For a material to be applied to photonics a high n is clearly needed because it allows for the confinement and manipulation electromagnetic radiation. However, this is just one of the conditions, the other being the low k in the range of large n to avoid absorption losses that determine a low efficiency of the photonic device. The high-n, low-k feature is not common among materials and therefore TMDs are extremely valuable for photonics, in particular for photonic crystals, where the high contrast between the high- and low-n materials is mandatory for good performances. However, even though TMDs are known to possess valuable optical constants for the fabrication of photonic devices, it is worth noting that there are no examples in the literature where this has been done. This is mostly due to the lack of synthesis techniques needed to produce a large area, controlled thickness and morphology, high quality material.

2.2 SYNTHETIC APPROACHES

Synthetic strategies for achieving TMDs can be divided in two classes: top-down and bottom-up. Top-down approach consist in various exfoliation techniques that allow to obtain a single- or a multi-layer TMD starting from a bulk crystal: the weak cohesive Van der Waals forces that keep together bulk TMD crystals allow for it to be separated with low effort. Exfoliation processes can be divided into two classes: mechanical and liquid-based. Mechanical exfoliation consists in the separation of TMD layers with Scotch tape, in the same way as it is done with graphene[126]. This technique allows to have very high quality, ~10 μm^2 sized layers, but it is very time consuming, not greatly controllable and the upscaling of the process is almost impossible. Liquid exfoliation techniques are instead based on the sonication of a bulk crystal

in appropriate solvents or on the intercalation of lithium containing compounds into atomic layers[105,127]. Both systems have a high reaction yield but, as mechanical exfoliation methods, are not greatly controllable; moreover the average flake size is quite small ($< 1\mu m^2$). Top down methods produce therefore extremely high quality materials, but they are limited for applications to devices because they lack thickness control and scalability, that are key parameters as much as the purity of the synthesized material. Bottom-up approaches can dismantle the limitations posed by exfoliation techniques. The majority of bottom-up methods exploit gas phase reactions between TMD precursors[117,128]. These methods fall in the large family of chemical vapor deposition (CVD) techniques. CVDs are well known and widely used film growth techniques consisting in the reaction of precursors in a gas chamber, with the final product growing on a substrate. The great advantage of CVD growth is that it allows for good control over stoichiometry, film quality and thickness, and reproducibility[129]. Importantly, with some gas flow optimization it is possible to have omogeneous films over very large areas: the greatest advantage of bottom-up methods with respect to their top-down counterparts is that they are scalable up to unprecedented levels. Those reaction can be divided into 4 categories:

1. reaction between metal and chalcogen precursors generated by thermal evaporation of powders[130];
2. reaction between metal and chalcogen precursor gases[131];
3. reaction between a metal or metal oxide substrate and a chalcogen precursor generated by thermal evaporation of a powder[132];
4. reaction between a metal or metal oxide substrate and a chalcogen precursor gas[133].

The choice between gas phase and powder precursor can be made depending on the employed system and on the requested features of the final product. For instance, as a sulfur (S) precursor it is possible to choose between S powders or hydrogen disulfide (H_2S). Both precursors allow for the reaction, but the main difference is that S powders are easy to handle and non-toxic, while H_2S needs to be handled with extreme care because of its severe toxicity, flammability and explosivity. However, if the correct safety procedures are followed, H_2S allows for a better control of the gas flow to the reaction chamber and to the sample, therefore yielding a better quality film with higher reproducibility[117]. Another technique for the growth of thin TMD films is atomic layer deposition (ALD), that will be described in Section 3.1.2. It is a modified CVD where the reactants enter in the chamber one at a time and not simultaneously. ALD allows for extreme control on film thickness

and morphology, for high scalability and reproducibility and for completely conformal growth on very large aspect ratios. The last feature is the one that differences the most ALD from other gas phase growth techniques: with no other process it is possible to obtain an extremely conformal growth on large areas and aspect ratios. However, direct ALD growth of TMDs is still not common because of the extreme contamination ability of common chalcogen precursors and for the lack of suitable chemistry. To overcome this issue, it is possible to use ALD to grow a thin film of a metal or metal oxide and then chalcogenize it in a two-step synthesis, following the process briefly described in point 4 of the list reported above[134]. In this way, the metal oxide film has all the benefits of ALD deposition that allow to satisfy the need of high quality, uniform substrates, that is one of the major drawbacks of TMD synthesis. Moreover since thickness and morphology of the chalcogenized TMD film are inherited from the precursor oxide[132], also the final TMD film presents all the benefits given by ALD. It is therefore possible to have extremely high quality, large area and conformal monolayers with precision and control thanks to the combination of ALD growth and gas phase chalcogenization.
In this work, we chose to use ALD to deposit WO_3 and then we converted it to WS_2 using dry H_2S in a tube furnace at high temperature. The details of the synthetic procedure will be given in Chapter 3.

3

FABRICATION PROCESSES AND CHARACTERIZATION TECHNIQUES

3.1 FABRICATION

3.1.1 *Lithography and Etching*

Lithography: A cleaned fused silica substrate is spin-coated with 50 nm of poly(methyl methacrylate) (PMMA), a positive electron beam resist. To avoid charging effects during electron beam exposure, a conductive polymer called aquaSAVE (Mitsubishi Rayon Co, Ltd.) is spin-coated on top of PMMA. The PC pattern is exposed on a defined area of the resist with an electron beam at 100 keV of energy, 500 pA of beam current, and $\sim$ 2000 $\mu C/cm^2$ dose using a Vistec VB300 e-beam lithography system. After the exposure, aquaSAVE is removed by rinsing with water, the desired patterns are developed by dissolving the exposed part of the resist in a 7:3 ratio mixture (chilled to -5°C) of isopropyl alcohol and water, sonicating for 100 s.

Etching: etching was performed with an Oxford Instruments Plasmalab 80+ reactive ion etching (RIE). The plasma is composed of 96 sccm CHF_3 and 4 sccm O_2. The etching process alternates between 45 s at a power of 300 W and 45 s at a power of 25 W, repeating two times. The overall etching rate is $\sim$ 0.5 nm s^{-1}. The resist is stripped with MicroChem Remover PG.

3.1.2 *Atomic Layer Deposition*

Canonical fabrication routes for PCs can be divided into two general classes: top-down and bottom-up approaches. Top-down fabrication is based on lithography and etching of a bulk material and can produce remarkably high precision and resolution, although it is slow and expensive. Bottom-up fabrication uses self assembly of repeating subunits (generally spheres, as in opals) to create a photonic lattice. Due to

the low n of these sub units (often polystyrene or silica), index contrast can be improved by infilling the opal with a high index material via sol-gel[66,86] or atomic layer deposition (ALD) processes to produce inverse opals[89]. While cheaper and easier to fabricate than top-down processing, the resulting structures are less controlled and yield more defects. Both methods are limited by a lack of techniques to grow or etch materials with a sufficiently high n: common materials for ALD infiltration of opaline structures are transition metal oxides as TiO_2[19,135] and ZnO[89], but the highest n for these materials is still not enough to obtain extremely high index contrast PCs. Here we propose a novel strategy for the fabrication of high n PCs combining ALD with canonical PC fabrication methods. This strategy has already been applied in some cases to PCs, from 2D slabs[85,136] to 3D opals[88] and it has been shown that it gives control on the photonic bandstructure just by changing thickness of the deposited material. It is therefore a promising approach that has already been investigated, and we believe that the combination of ALD with the chalcogenization processes to yield TMDs reported in Section 2.2 will be the best route to easily fabricate high n PCs working in the visible and NIR.

Atomic Layer Deposition (ALD)[137,138] is a thin film synthesis technique that allows for the deposition, as the name suggests, of one atomic layer at a time over surfaces of virtually any morphology. It exploits self-limiting reactions of gas-phase precursors with a surface. ALD can be considered a modified CVD, where in contrast with CVD the precursors are inserted in the reaction chamber in well separated time frames. Precursors are chosen to be extremely reactive with surface species, but inert to self-reactivity. Since surface sites are not infinite, the reaction can only deposit a finite number of precursors. In this way, the reaction stops as soon as the available surface species are saturated, allowing for self-limiting growth. The deposition is always uniform and, since the reaction is completed during every cycle, ALD grown films are always smooth. Moreover, since the reaction occurs between a precursor and a surface site, ALD produces remarkably continuous films, with no pinholes that may be a problem in some applications where perfect insulation is mandatory. The nature itself of ALD allows for an almost perfect conformal growth of extremely high quality films on surprisingly high aspect ratios (up to 300:1) and on very large scales (up to several cm^2). This is because the reaction only happens at the surface and does not depend on the morphology but only on its termination. A typical ALD process, reported in Figure 4, can be outlined as follows:

1. The first precursor, for instance a metal-organic complex, is injected into the reaction chamber and reacts with terminal functionalities of the sample's surface. The reaction binds precursors to the surface, generating organic species as a product;

2. The chamber is purged and unwanted products are removed;

3. The second precursor, for instance a plasma like H_2O or O_2, is injected into the chamber and reacts with the remaining organic ligands bound to the metal ions;

4. The reaction products are removed by purging the chamber. A cycle is now completed and the process starts again from step 1.

Typical materials grown by ALD are binary transition metal oxides as Al_2O_3, TiO_2, ZnO, ZrO_2, HfO_2 and WO_3[137]. Most processes for the deposition of those oxides are based on CVD reactants that are injected in the chamber at separate times; reactions are in general exothermic and can occur in a wide range of temperatures as low as 150°C (for thermal processes) or room temperature (for plasma-activated processes). Other common materials are nitrides as TiN, TaN and W_2N[137], while ALD processes for chalcogenides[139] are less common because the resulting film quality is still not satisfactory[140]. Therefore, to overcome this issue the synthesis of ALD TMDs follows the different approach briefly outlined in Section 1.3: ALD is employed to deposit a transition metal oxide as WO_3, which is then exposed to a chalcogenizing agent as H_2S and converted to the corresponding TMD, as WS_2, that inherits morphology and conformality from the starting oxide.

Fused silica wafers were conformally coated with WO_3 using plasma-enhanced ALD at T = 40°C. We used bis(tert-butylimido)-bis-(dimethylamido) tungsten[141] and oxygen plasma in an Oxford Instruments FlexAl ALD system. The growth rate for the WO_3 was ~ 1 Å per ALD cycle. The tungsten precursor was dosed into the chamber for 3 seconds at 20 mTorr. The chamber was isolated from the turbo pump and held at 30 mTorr for 1 second as a wait step, to compensate for the low reactivity of the precursor. The chamber and dosage line were then purged with 100 sccm of argon and pumped to 15 mTorr for 10 seconds at 40°C. Oxygen plasma was generated via remote inductively coupled plasma at 30 mTorr with 300 W power, and maintained for 2 seconds, then purged with argon at 15 mTorr for 10 seconds. This process was repeated as necessary to produce the required thickness, at approximately 1 Å/cycle.

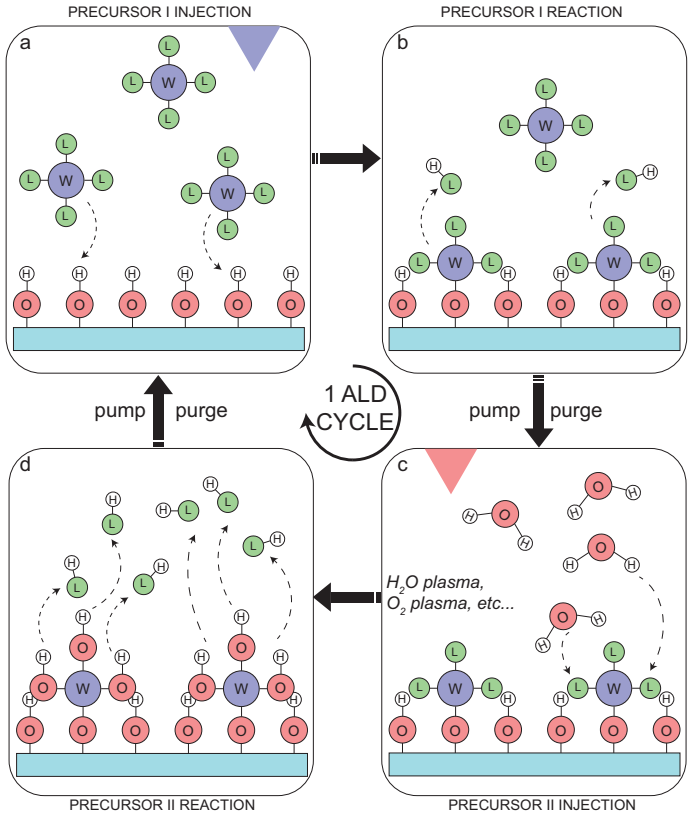

Figure 4: Schematic of the ALD process. a) A first precursor, for instance a metal-organic complex, is injected into the reaction chamber. b) The precursor reacts with the terminal functionalities of a substrate (e.g. hydroxil groups on a SiO_2 wafer). After the reaction time, the chamber is purged and the products are removed. c) A second precursor, for instance H_2O or O_2 plasma, is inserted in the chamber and d) it reacts with the first precursor's organic ligands, to yield the final product. The chamber is purged and the cycle starts again from a).

3.1.3 *Chalcogenization in a Tube Furnace*

The conversion of ALD-grown WO_3 to WS_2 occurs efficiently at high temperatures[117] and is therefore performed in a furnace. Chalcogenide precursors are delivered in gas-phase, and the laminar flow of the carrier gas brings them in contact with the WO_3 film. Although there are several configurations, a typical tube furnace system, reported in Figure 5, consists of 4 fundamental parts:

1. the gas sources and pressure regulators. Gas sources can be pressurized cylinders or solid/liquid precursors that are vaporized. Gas-phase precursors (as H_2S) are contained in cylinders that are in general highly pressurized as high as 2000 psi. Therefore, pressure regulators are used to reduce the outstream pressure to a value below 150 psi. Precursors that are solid (as sulfur) or liquid (as ammonia) at room temperature are handled in a different way, by using a solid/liquid precursor delivery system, usually referred to as the bubbler. Precursors have to exhibit relatively high vapor pressures, so that their vapors can be delivered by a carrier gas (usually inert gas like nitrogen or argon) to the reaction chamber. The bubbler consists of a glass or stainless steel vessel. The carrier gas is fed through a mass flow controller to the inlet line and exits through the outlet line saturated with precursor vapors;

2. mass flow controllers (MFCs). MFCs regulate the flow of the gas supplied either to a precursor bubbler or directly into the system. Input pressure is generally between 30-50 psi, and output is held under vacuum or atmospheric pressure. Flow rates are generally from 1 to 2000 sccm (standard cubic centimeters per minute);

3. the reactor. It is designed to be operated safely under vacuum or pressures close to 1 atm. The reactor consists of a process tube encased in a tube furnace. The process tube is made of heat resistant high-density ceramics or glass (typically: quartz, alumina, zirconia or boron nitride), which is selected according to the process temperature and chemical nature of the process gases. Typical diameters are from 2.5-7.5 cm (1-3 inches), and the length of the process tube is sufficient to prevent temperature rise (above $\sim$ 100°C) at the tube ends. The tube is connected to the gas manifold and the exhaust by sealed connectors;

4. the exhaust system. Its role is to properly dispose of the gaseous reaction products and excess reactants. In most cases the exhausts gases are released to the building ventilation or hood exhaust through a stainless steel discharge line. However, in cases

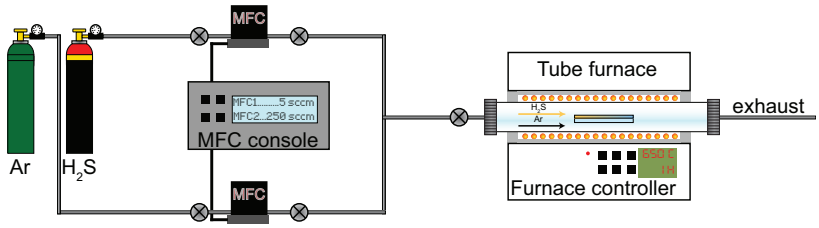

Figure 5: Schematic of the tube furnace system used to convert WO_3 to WS_2. The gas phase precursor (H_2S) and the carrier gas (Ar) cylinders are connected to MFCs that determine the gas flux to be respectively 5 sccm and 250 sccm. The reaction occurs between the H_2S laminar flow and the WO_3 film inside the tube furnace at 650°C for 1 hour.

that their chemical nature requires it, the gases will be bubbled through a scrubbing solution that removes the hazardous components.

WO_3 films deposited on SiO_2 substrates are placed at the center of a 2.5 cm (1 inch) diameter tube furnace. We used a Lindberg-BlueM Mini-Mite equipped with power supplies controlled by programmable PID controllers reaching temperatures as high as 1300°C. We used 99.999% pure Ar (Praxair Ultra High Purity Grade) as a carrier gas at a flow rate of 250 sccm. As a chalcogen source, we used 99.6 % pure H_2S (Praxair) at a flow rate of 5 sccm. We pumped and purged the tube furnace multiple times, from low vacuum to atmospheric pressure under Ar flow, after loading the samples. The temperature of the furnace is increased from RT to T=650°C and is kept for 60 minutes total. The H_2S flow is stopped at the end of the 60 minutes annealing. At the end of the annealing the furnace is purged with 250 sccm Ar during cooldown.

3.2 CHARACTERIZATION

3.2.1 *Spectroscopic Ellipsometry*

Ellipsometry is an optical characterization technique that allows for the measurement of dielectric properties, for instance n and k, of thin films[142]. Moreover, ellipsometry can be employed to measure and estimate composition, doping level, roughness and thickness of a deposited thin film. An ellipsometry measurement detects the variation of polarization of an incident wave as it interacts with the material or structure of interest. It is an extremely sensitive technique that allows to have a detailed physical characterization even for very thin materi-

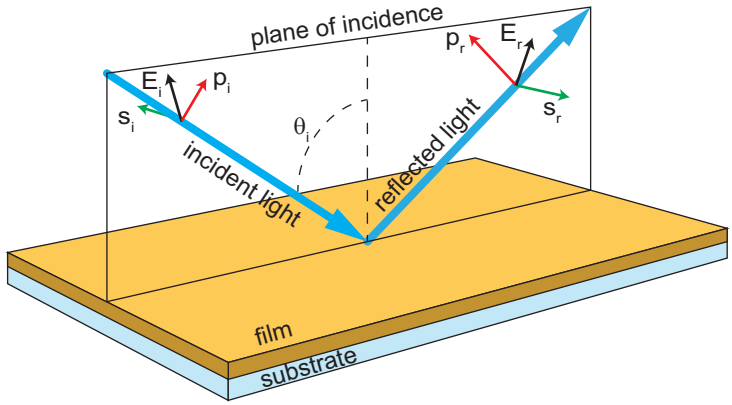

Figure 6: Schematic of an ellipsometry experiment. A polarized beam is reflected from the sample. The incident polarization E_i has a parallel and a perpendicular component with respect to the incidence plane (p_i and s_i, respectively). The reflected beam changes its polarization E_r and its parallel and perpendicular components (p_r and s_r, respectively).

als, down to an atomic layer. Ellipsometry measurements are in general performed in a reflection setup, as shown in Figure 6. Incidence angle is in general close to the Brewster angle to maximize reflection. A more precise, yet more complex measure is done by changing incidence angles and integrating the acquired data with a measurement obtained at 0°, i.e. in transmission configuration.

Light emitted from a source is polarized and its polarization is divided in two components: one parallel and one perpendicular to the plane of incidence (p and s components, respectively). Incident light needs to be linearly polarized with both p and s components. Reflected light, after interacting with the samples, experiences variations in amplitude and phase for both p and s components. The ellipsometer measures the complex reflectance ratio ρ of the sample, that is defined as the ratio between the complex reflectance of the p component and that of the s component:

$$\rho = \frac{r_p}{r_s} = \tan(\Psi)e^{i\Delta}, \tag{40}$$

where $\tan(\Psi)$ is the amplitude ratio after reflection and Δ is the phase difference. The reason why ellipsometry is such a precise technique is because it measures a difference and a ratio and does not rely on standard samples or calibration curves. A classical ellipsometry measurement is made with just one wavelength (i.e. with a laser), but by us-

ing a broadband lamp with a monochromator it is possible to generate spectra for Ψ and Δ in the technique named Spectroscopic Ellipsometry.

While extremely powerful, ellipsometry is a very complex technique when it comes to data analysis. The measurement of Ψ and Δ is not a direct measurement of a physical quantity of interest: ellipsometry is an indirect method and the experimental data have to be modeled in order to be converted in the parameters of interest (i.e., n and thickness). In case of a perfectly isotrope, bulk and transparent material, the equations derived from an ellipsometry measurement can be inverted to provide "pseudo" optical constants, using the following:

$$\langle \tilde{\varepsilon} \rangle = \sin^2\theta_i \left[1 + \tan^2\theta_i \left(\frac{1-\rho}{1+\rho} \right)^2 \right]. \tag{41}$$

θ_i is the angle of incidence and $\tilde{\varepsilon}$ is the complex dielectric constant of the material, related to the complex refractive index by the relations provided in Section 1.1.

However, for most materials Equation 41 cannot be applied because it does not take into account surface effects, reflections due to scattering and roughness, defects, and other deviations from ideality. Therefore, the most common way to analyze ellipsometry data is through modeling. The model parametrizes each layer, from substrate to measured film, and calculates Ψ and Δ. Calculated values are compared to experiment results and, if the mean squared error (MSE) is too high, the calculation is done again following an iterative fitting process. The model can be a physical description of the system but it can also be made of free parameters used to best fit the experimental data. After the fit is finished, i.e. MSE is minimized, it is possible to extract the physical parameters of interest. It is worth noting that, since ellipsometry is a technique based on the detection of reflected light, it is particularly complex when applied to absorbing materials. Light absorption decreases the reflected signal, thus increases the error on the measurement yielding poor quality data that are extremely hard to fit with a model. By acquiring ellipsometry measurements at different angles it is possible to tackle this issue: the change in the angle modifies the optical path of the light beam in the material, i.e. the quantity of absorbed light. Therefore, as the complexity of the sample increases (e.g. for strongly absorbing films) it is good norm to acquire data at more incidence angles than just one. While the standard angle of incidence is around 75°, a good range for various angle measurement is 50° to 75°.

We measured the thickness of the deposited WO_3 film with a Woolam M-2000 ellipsometer in situ on the ALD. The optical constants measurements were performed with a similar M-2000 spectrometer, but not

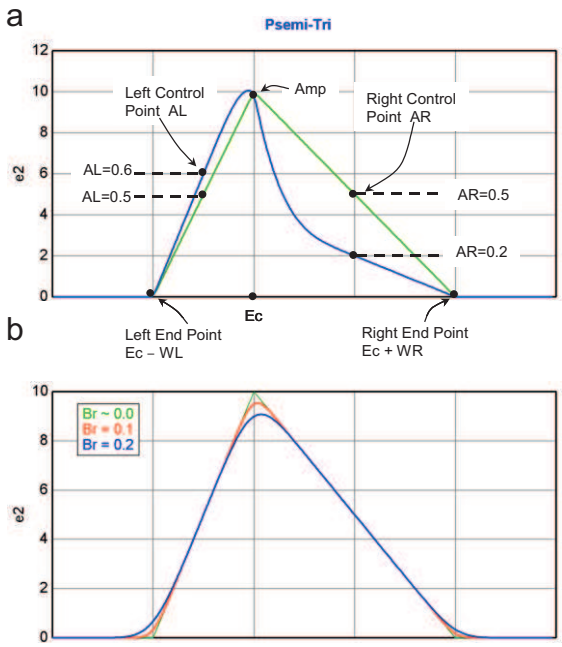

Figure 7: PSemi-Tri oscillator. a) The fit parameters are *Amp*, the amplitude of the oscilator; the gaussian broadening parameter *Br*; the center point *Ec*; the left and right end points *WL* and *WR*, respectively; the left and right adjustment point *AL* and *AR*, respectively. b) Three PSemi-Tri oscillators with the same parameters but with different *Br*.

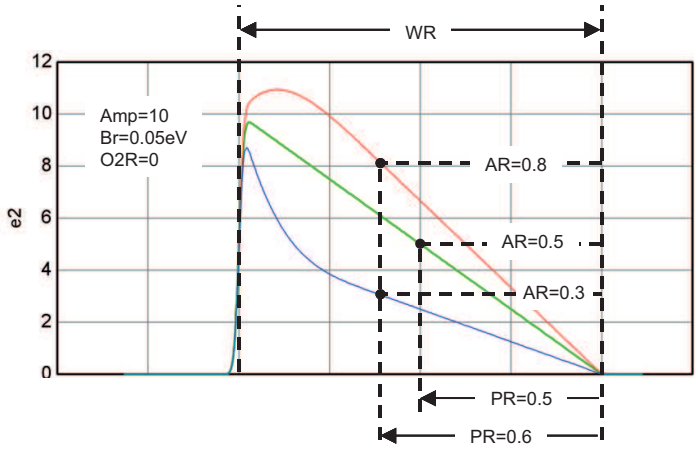

Figure 8: PSemi-M0 oscillator. The fit parameters are the amplitude *Amp*; the gaussian broadening parameter *Br*, the right end point *WR*; the right adjustment point *AR*; the right position of the adjustment point *PR*.

mounted on an ALD. This allowed for a measurement with different incidence angles, from 45° to 60°, as will be reported in Section 4.2. n and k for WS_2 were extracted from ellipsometric data after fitting with a general oscillator model consisting of PSemi-Tri and PSemi-Mo functions. These functions, which are a subset of the more general Herzinger-Johs Parametrized Semiconductor Oscillator functions, are proprietary of Woolam that provides them in the CompleteEase^{TM} software. The shape of the functions is reported in Figure 7 and Figure 8, respectively. Each function has a set of various parameters that give a highly flexible functional shape.

3.2.2 *Structure and Morphology*

Structure and morphology of the synthesized structures were characterized by atomic force microscopy (AFM), scanning electron microscopy (SEM) and Raman spectroscopy.
AFM: AFM micrographs were acquired with a Park NX-10 AFM, acquiring images in tapping mode.
SEM: SEM micrographs were acquired with a Zeiss Ultra 60-SEM, detecting back-scattered electrons at 5 keV. Each image was averaged 10 times for a total acquisition time of about 1 minute.
Raman: Raman spectra were acquired with Horiba Jobin Yvon LabRAM ARAMIS automated scanning confocal Raman microscope with a 50x objective. The excitation wavelength was 532 nm. The integration time was 10 s.

3.2.3 *Transmission Measurements*

The characterization of the fabricated PCs was performed by measuring their light transmission properties. Since the fabricated structures are squares of about 100 µm side it was essential to measure the transmission with a microscope in order to focus on each different PC, excluding every other from the field of view. Therefore, the setup we used was a home-built bright field microscope that allowed for simple measurement with great precision and versatility. The setup is reported in Figure 9.

The light source was a Thorlabs SLS201 fiber-coupled white lamp, which emission was collimated and directed towards the sample. The transmitted light was then collected with a 40x 0.75 NA, 0.66 mm working distance Nikon flat-field corrected fluorite objective. The collection objective was mounted on a *xyz* stage that allowed for the focusing of the detection system on the PCs and for its movement between the various samples fabricated on the same SiO_2 wafer. The sample was

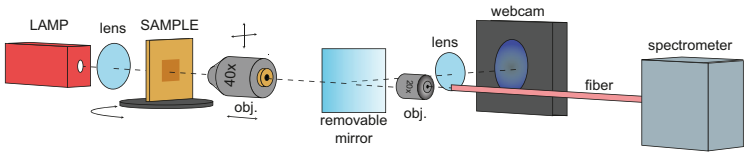

Figure 9: Schematic of the transmission measurement setup. Light is generated from a white lamp and is collimated by a lens. It then reaches the sample that is mounted on a rotation stage. The transmitted light is collected by a 40x objective and is focused with a 20x objective on a fiber bundle coupled to a CCD spectrometer. If inserted, the removable mirror allows to direct the transmitted light towards a webcam used to focus the collection setup.

mounted on a rotating sample-holder to collect of the transmission spectra as a function of light incidence angle. The transmitted light was then focused with a 20x objective on a multimode round-to-linear fiber bundle and collected with an Andor Shamrock SR303i spectrometer coupled to an Andor Newton CCD camera. A removable mirror positioned after the sample, but before the fiber bundle, allowed to deviate the transmitted light towards a Thorlabs webcam, which was used as a reference during focusing of the collection objective on each PC.
To calculate the transmission of each sample, we measured the light transmitted by the WS_2 PCs and we considered as a baseline the light transmitted by and unstructured WS_2 thin film of the same thickness, as is reported in Figure 10. Then, we normalized the light transmitted by the PC, I_{PC}, to the light transmitted by the unstructured sample, I_0, and we defined the transmission of the PC:

$$T_{PC} = \frac{I_{PC}}{I_0}. \tag{42}$$

The normalization was performed in order to eliminate the residual contributions to reflection and absorption of WS_2, so that any deviation from unity is exclusively determined by the PC.

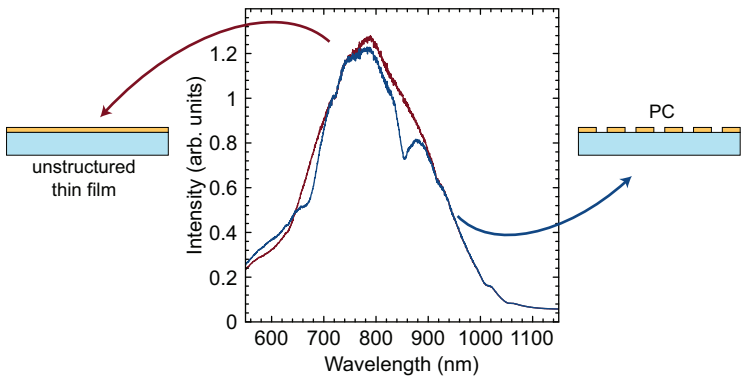

Figure 10: Schematic of the transmission measurement calculation. The red line is light transmitted by an unstructured WS_2 film. The blue line is light transmitted by a WS_2 PC. Dividing the second by the firs yields the PC transmission T_{PC}.

4

RESULTS AND DISCUSSION

The first step towards the fabrication of WS_2 based PCs was the optical and morphological characterization of the material. We performed AFM and SEM microscopy measurements to set the optimal growth conditions in order to have the best quality material. Then, we obtained the optical constants n and k with the modeling of spectroscopic ellipsometry curves. The obtained n and k legitimate the application of WS_2 to photonics: therefore, we fabricated WS_2 based PCs using two different approaches: first by etching holes in a deposited ALD film and then by coating a pre-fabricated low-n structure.

4.1 WS_2 MORPHOLOGY

Optical and photonic properties of PCs strongly depend on both fabrication accuracy and on material morphology. A PC fabricated with low precision will not be regular enough, thus generating inhomogeneous broadening in the features and sometimes yielding loss of periodicity. Furthermore, defects in the fabrication process could cause unwanted modes that may affect the application of the PC. For instance, unwanted cavity modes resulting from fabrication defects may induce uncontrolled resonances that hinder the applicability of a device. On the other hand, bad surface morphology will determine uncontrolled optical effects and will lower PC performances. Optimization of fabrication processes and material quality is therefore the first and most important step in the production of good quality PCs. To investigate both aspect we first fabricated a prototype structure. We etched $\sim$ 100 nm deep holes in a fused SiO_2 wafer with electron beam lithography (EBL) and reactive ion etching (RIE), as described in Section 3.1.1. We then coated the so-fabricated PC with a 20 nm thick layer of WO_3 grown with atomic layer deposition (ALD), as described in Section 3.1.2. The deposition temperature was set at 40°C because it allowed for a faster process. In general, the deposition temperature affects morphology and density of the deposited film[143]. However, the deposited WO_3

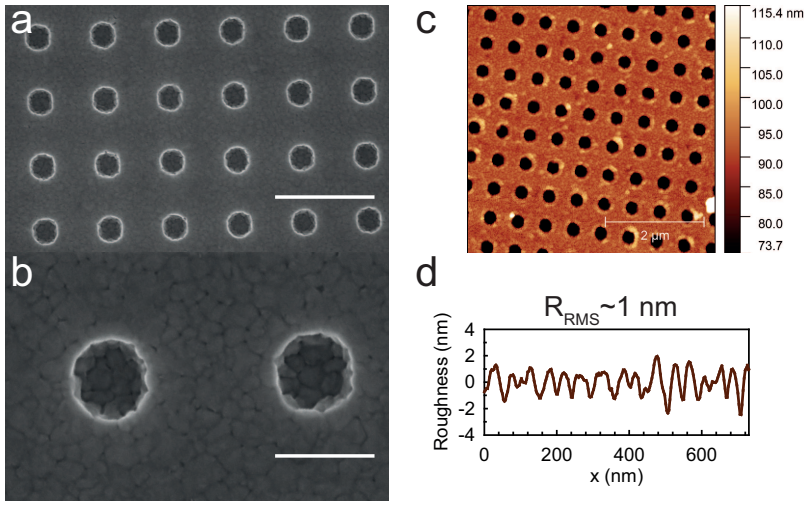

Figure 11: Surface morphology analysis of a WS_2 PC chalcogenized at 750°C. a) SEM micrograph at 25kx magnification. The scale bar is 1 µm. Grains with different contrast can be noticed. b) SEM micrograph at 100kx magnification. The scale bar is 250 nm. The grains of different morphology are more noticeable and are tens of nanometers in size. c) AFM micrograph of the same WS_2 PC, showing an overall not satisfactory morphology. The scale bar is 2 µm. d) surface roughness extracted from the AFM in c). The average roughness of the sample is ~ 1 nm.

films were then chalcogenized at higher temperatures with respect to the maximum temperature obtainable by the ALD. The bottleneck for morphology of the final WS_2 film is therefore the annealing step and not ALD growth. Test samples deposited at different temperatures and annealed at the same temperature showed no measurable difference. After depositing the WO_3 film on the etched SiO_2 wafer, the sample is annealed in a tube furnace in presence of H_2S and with Ar as a carrier gas, as described in Section 3.1.3. The annealing temperature was chosen to be 750°C because of previous experience, and annealing time was set to 1 hour. SEM and AFM micrographs of the PC fabricated with the process described above are reported in Figure 11. A major problem can be noticed: WS_2 morphology is not satisfactory. After some literature investigation, we determined that this is because at 750°C the volatility of WO_3 starts to be not negligible, resulting in increased mobility and film evaporation in the furnace[144]. While average roughness measured with AFM is just around 1 nm (see Figure 11d), it can be seen from SEM micrographs that there are regions with different contrast that form grain boundaries. This is clearly a non-ideal situation, because grains break the simmetry and introduce defects that signif-

icantly lower performances of the fabricated device. We decided to tackle this issue by changing annealing temperature. Therefore, we fabricated two more WO_3 films on fused SiO_2 wafers in the same way as described above, but this time we did not fabricate the photonic structure, in order to just focus on film morphology. We chalcogenized one film at 550°C and one at 650°C for 1 hour and we report AFM and SEM micrographs of the resulting WS_2 films in Figure 12. To confirm that the roughness we measured was not due to the underlying substrate, we acquired an AFM image of a bare SiO_2 wafer, as shown in Figure 13.

The sample at 550°C shows an average roughness of ~ 3 nm, i.e. higher with respect to the 750°C case. The SEM micrograph shows that there are no large grains as in the aforementioned case, but the overall morphology is still not satisfactory and shows some irregularities. Those are likely due to a too low annealing temperature that does not allow for a complete conversion of WO_3 to WS_2. The sample converted at 650°C shows instead a good average surface roughness of < 1 nm. The goodness of this sample is confirmed by the SEM micrograph, which shows a substantially uniform film on large scales. The parallel lines that can be seen in the sample chalcogenized at 650°C and in the bare SiO_2 wafer are determined by the polishing of the wafer. Interestingly, the morphology of WS_2 perfectly traces that of the underlying wafer, demonstrating perfect conformal growth. We therefore decided to set the annealing temperature at 650°C for all following chalcogenizations, because the resulting film met our quality requests.

4.2 OPTICAL CHARACTERIZATION OF THE WS_2 FILM

After setting the synthesis parameters we proceeded with the optical characterization of the material. To confirm that the chalcogenization of WO_3 to WS_2 was successful we performed Raman spectroscopy as described in Section 3.2.2 on a 150 nm thick, bulk like WS_2 film obtained after chalcogenization of ALD WO_3. The Raman spectrum of WS_2 after annealing is reported in Figure 14. The presence of WS_2 fingerprint vibrational modes[145] (E^1_{2g} at 353 cm^{-1} and A_{1g} at 417 cm^{-1}) demonstrates conversion of WO_3 to WS_2.

We then performed spectroscopic ellipsometry measurements on the annealed film to obtain the optical constants n and k of the WS_2 we synthesized. Since WS_2 is a strongly absorbing material, ellipsometry is extremely complex and it is critical to have a good model that fits the measurements results in order to have an accurate estimate of the optical constants. Moreover, data acquisition is crucial to take into account absorption losses in the best possible way, as explained in Sec-

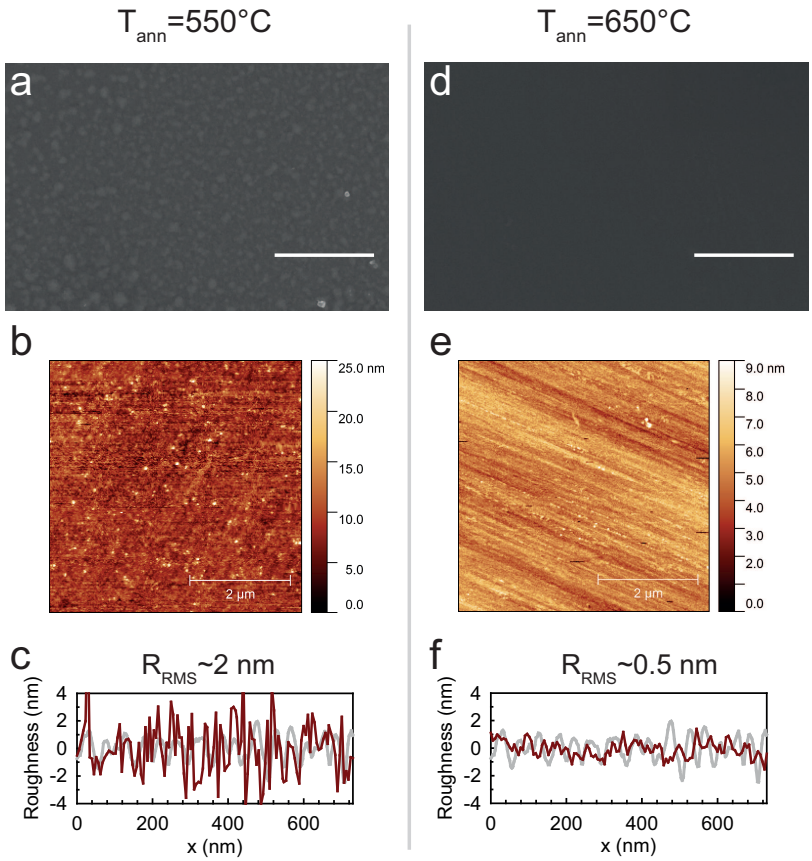

Figure 12: Surface morphology analysis of WS_2 films chalcogenized at 550°C (left-hand side) and at 650°C (right-hand side). a), d) SEM micrographs at 25kx magnification. The scale bar is 1 µm. Grains with different contrast can be noticed in the sample converted at 550°C, while the surface morphology of the sample converted at 650°C is much smoother. b), e) AFM micrographs of the same WS_2 samples. The sample converted at 550°C shows grains that make the surface morphology not satisfactory. The sample converted at 650°C shows instead parallel lines that correspond to polishing lines of the underlying SiO_2 wafer (see Figure 13). The scale bar is 2 µm. c), f) Surface roughness extracted from the AFM in b) and e), respectively. The average roughness of the sample converted at 550°C is ~ 2 nm, while for the sample converted at 650°C is ~ 0.5 nm. The grey line in both graphs is the average roughness on the sample converted at 750°C and shown in Figure 11d.

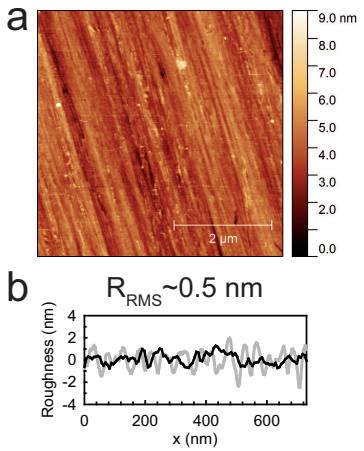

Figure 13: Surface morphology analysis of a fused SiO_2 wafer. a) AFM micrograph of the wafer. The scale bar is 2 µm. The parallel lines are generated by the wafer polishing process. b) Surface roughness extracted from the AFM in a). The average roughness of the SiO_2 wafer is 0.5 nm. The grey line is the average roughness on the sample converted at 750°C and shown in Figure 11d.

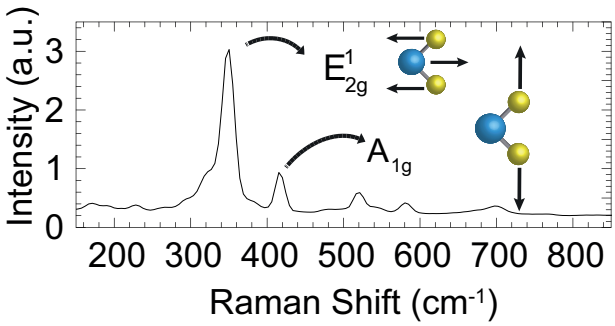

Figure 14: Raman spectrum of the WS_2 film synthesized as described in the main text. The excitation wavelength was 532 nm. The E^1_{2g} peak at 353 cm^{-1} and the A_{1g} peak at 417 cm^{-1}, related to the vibrational modes illustrated with the ball-and-stick molecule drawn in the image, are the fingerprints of WS_2.

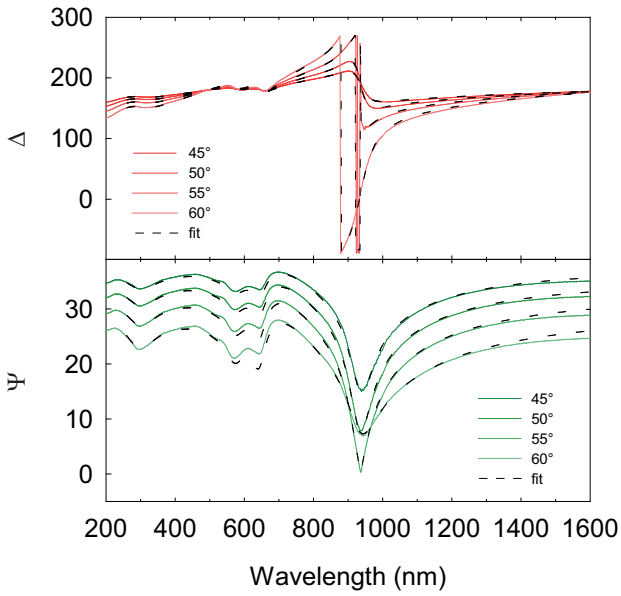

Figure 15: Result of the ellipsometry measurement on the WS_2 film. The phase Δ (red lines) and the amplitude Ψ (green lines) are reported after acquisition at various angles, from 45° to 60°. The black dotted lines are the fit for each angle obtained from the model described in the main text and whose parameters are reported in Figure 16.

tion 3.2.1. Therefore, we measured amplitude Ψ and phase Δ both in reflection and in transmission configuration. Results of ellipsometry measurements are reported in Figure 15.

n and k for WS_2 were extracted from ellipsometric data after fitting with a general oscillator model consisting of PSemi-MO and PSemi-Tri functions, that are described in Section 3.2.1. Fitting parameters for WS_2 oscillators were refined until the mean squared error (MSE) of the fit was minimized to a value =14. Fit parameters are reported in Figure 16, while the resulting fit is reported in Figure 15. It can be noticed that the agreement between experimental value and modeled curves is very good.

The optical costants n and k obtained from the SE modeling are reported in Figure 17. n is remarkably high through all the electromagnetic spectrum and reaches a value of ~ 3.8 at 640 nm. Interestingly, n is very high even in the spectral region where k is negligible, i.e. where WS_2 is transparent. This is the most relevant region of the spectrum for the application to photonics, because a completely transparent mate-

t=161 nm
E_{inf}=0.0953 IR pole amp=-0.9555
UV pole en=11.07 UV pole amp=11.07

Oscillator1: PSemi-M0			
Amp_1=15.409	BR_1=0.1958	$E0_1$=2.272	WR_1=1.8007
PR_1=0.691	AR_1=0.504	$O2R_1$=0.809	
Oscillator2: PSemi-Tri			
Amp_2=3.180	BR_2=0.0875	EC_2=2.028	WL_2=0.5832
WR_2=0.0546	AL_2=0.1503	AR_2=5.000	
Oscillator3: PSemi-M0			
Amp_3=15.466	BR_3=1.0252	$E0_3$=3.581	WR_3=5.0562
PR_3=0.468	AR_3=0.172	$O2R_3$=-0.934	

Figure 16: Schematic of the model and fitting parameters for the Spectroscopic Ellipsometry data reported in Figure 15.

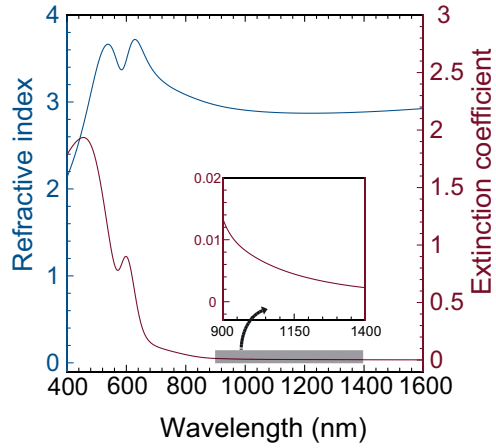

Figure 17: Optical constants of the synthesized WS_2 film derived by modeling the ellipsometry measurement reported in Figure 15. The refractive index n (blue line) is remarkably high in the region where the extinction coefficient k (red line) is negligible. Inset: magnification of the transparency area of the material, where k is < 0.01.

rial in the region of high n allows for having a strongly modulated PC without absorption losses. n for the synthesized WS_2 is ~ 3 for $\lambda > 900$ nm, where $k < 0.01$ (see inset in Figure 17). This combination of high n and low light absorption legitimates the application of the WS_2 we synthesized to photonic devices working in the near-infrared (NIR). We want to point out that the value for n we obtained in WS_2 is noticeably higher with respect to the best performing transition metal oxides, as TiO_2 or Al_2O_3, that have a n that is generally below 2 and can be as high as 2.5 in the best-case scenario[146]. However, the transparency region of transition metal oxides is far wider with respect to that of TMDs, spanning all the visible spectrum and reaching the near-ultraviolet. Thus, transition metal oxide-based PCs are more suitable for devices working in the visible or near-ultraviolet region of the spectrum, in spite of worse index contrast. The smaller energy gap of the most studied TMDs yields absorption edges in the NIR, preventing these materials from the fabrication of PCs operating in the visible. However, there are more than 60 different TMDs that have diverse optical properties: different combinations of high n and low k are likely to be found in other materials as $NbSe_2$ and $TaSe_2$[147]. In this work, we synthesized WS_2 because it is the material that best matches our expertise. It should be noticed that the optical constants we obtained for WS_2 we synthesized are lower in comparison with best-performing TMDs reported in the literature[93,122,148,149]. However, there is a lot of room for improving n, both in WS_2 and in other TMDs. For instance, higher ALD growth temperatures should increase density of the deposited material, which in turn will yield higher n[150]. The same is true for chalcogenization temperature: as reported in Section 4.1, high annealing temperatures will result in denser films and n increase, but on the other hand it will yield roughened surfaces due to increased volatility of WO_3[144], that will affect the final morphology of the WS_2 film and the quality of the PC itself. Work is underway to improve n for WS_2 while keeping the morphology of the material intact.

Evaluation of the optical constants of the synthesized WS_2 demonstrated its potential for applications to photonic devices and PCs. Therefore, we proceeded with the fabrication of prototypical PC structures based on a square array of holes. To do so, we followed two different approaches:

1. etching holes in a synthesized TMD slab (see Section 4.3);

2. conformally coating holes etched into a dielectric substrate (see Section 4.4).

PCs fabricated with both methods were characterized by measuring their light transmission properties as described in Section 3.2.3.

4.3 TWO-DIMENSIONAL PC SLAB

A two-dimensional (2D) PC slab is a thin film, virtually infinite in one plane but confined in one direction, with a PC structure fabricated into it[1]. For instance, it can be a film with a 2D array of holes or pillars fabricated into a substrate. PC slabs are interesting, model PC systems because they are easy to fabricate and their properties can be modeled with different theoretical techniques (Finite-Difference Time Domain, scattering-matrix based, and more). PC slabs work following two different effects. First, light is confined into the thin film because of total internal reflaction, that is determined by the high n contrast between the material composing the PC and the environment. Second, in the periodicity plane light experiences the photonic bandstructure (and bandgap, if present) and therefore propagates by following the solutions of the electromagnetic problem described in Section 1.1. Therefore, in most cases photonic properties of a PC slab are considered and evaluated inside the periodicity plane[92,151,152], but to measure them in this configuration some intensive device engineering has to be done. In detail: film thickness and geometric parameters of the PC should be optimized; then a waveguide that brings light to the <100 nm-thick slab needs to be fabricated; and last macroscopically generated light has to be coupled to the nanometer-sized waveguide. However, this type of experimental setup needs extensive optimization that was not a scope of the present work. It is nevertheless possible to inspect photonic properties of 2D slabs by analyzing *quasi-guided* modes[34,153,154]. Those are photonic modes of the slab that propagate in the periodicity plane, but they can be excited by an external radiation (or, if generated inside the 2D plane, they can radiate outside of the PC). The bandstructure of a PC slab has some states that extend in the continuum outside the slab itself. While in an "ideal" slab the modes are perfectly guided and confined in the high-n film, in a "real" system the introduction of corrugation and defects can couple guided modes towards the envrionment[155]. Those states are quasi-guided modes, that are also known as *resonant states*. In the text, we will refer to these modes as "resonances". When light of the correct wavelength interacts with the PC, it is scattered into the slab where it propagates following the bandstructure. Therefore, the study of resonant states allows for an investigation of the properties of a PC slab with no need for complex fabrication steps to couple light into the periodicity plane. Tikhodeev and coworkers have shown that the excitation of resonant states in a square-patterned PC slab with ex-

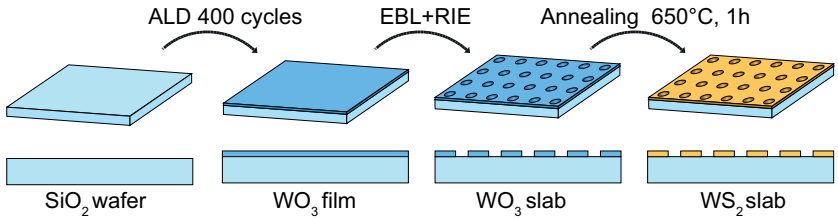

Figure 18: Schematic of the fabrication process for the WS_2 2D slab. A ~ 40 nm WO_3 film is grown via ALD on a fused SiO_2 wafer. The PC structures are fabricated with electron beam lithography followed by reactive ion etching. The fabricated WO_3 PC is then chalcogenized at 650°C in presence of H_2S for 1 h to obtain the final WS_2 PC.

ternal light generates two well-separated and pronounced dips in the transmission spectrum of the PC[155].

In this work, we designed a 2D slab made of a WS_2 film grown on SiO_2 with a PC structure etched into it. The n contrast is therefore given by alternating WS_2 and air in the xy plane, while the electromagnetic wave is confined in the z direction due to the high n of WS_2. The sketch of the fabrication strategy we followed is reported in Figure 18. First, we deposited WO_3 on a fused SiO_2 wafer with 400 ALD cycles, corresponding to a ~ 40 nm thick film. Following results on PC morphology described in Section 4.1, we then fabricated the PC structure using EBL followed by RIE, as described in Section 3.1.1, and chalcogenized the WO_3 to WS_2 at 650°C, with 5 sccm H_2S and Ar as a carrier gas, for 1 hour. We want to point out that the synthetized film is not a single-crystal monolayer, but rather a bulk-like nanocrystalline film. Therefore, it could be considered almost amorphous and has none of the exciting optoelectronic properties described in Chapter 2. We chose to grow an amorphous film because even if the energy gap is lower than in the monolayer case, the absorption cross section is lower - thus reducing absorption losses. Our TMD film just behaves like a very high-n dielectric. However, it is possible in principle to fabricate high index contrast PCs with high-energy gap monolayer TMDs working in a spectral range where light absorption is negligible. The photonic structure we chose to fabricate was a square lattice of holes of diameter equal to 260 nm, 310 nm and 360 nm with a periodicity of 590 nm, 610 nm and 630 nm. Therefore, we had a 3x3 grid of PCs with different combinations of hole diameter and periodicity. A schematic of the 9 PCs is reported in Figure 19.

The SEM micrograph in Figure 20 shows that the morphology of WS_2 is extremely good. To investigate the photonic properties of the

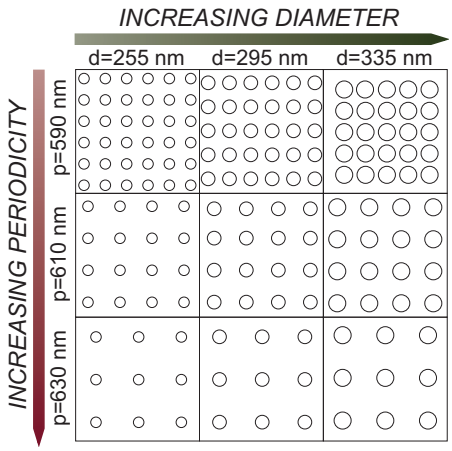

Figure 19: Schematic of the 9 fabricated PCs with different hole diameters (d) and periodicities (p).

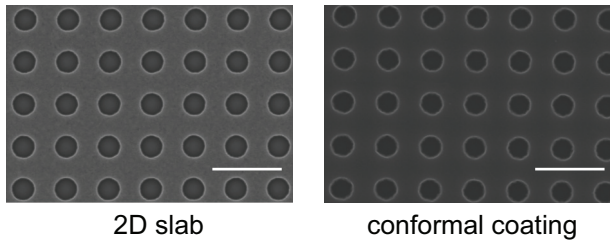

Figure 20: SEM micrographs of the WS_2 2D slab (left) and of the PC conformally coated with 10 nm of WS_2 (right). The scale bar is 1μm for both images.

WS_2-based PC, we measured the light transmitted by illuminating the sample with white light in a perpendicular geometry with respect to the periodicity plane with the setup described in Section 3.2.3.
We measured T_{PC} for all 9 fabricated structures. Each spectrum shows two features that correspond to different resonances, i.e. different ways light can couple into the 2D slab. This spectrum is in agreement with the theoretical prediction made by Tikhodeev[155]. Transmission spectra as a function of the hole diameter and of the PC periodicity are reported in Figure 21. By changing hole size the resonance intensity can be changed. A higher hole diameter increases the scattering cross-section, thus increasing the quantity of incident light that is coupled into the perpendicular 2D slab. Alternatively, changing the PC periodicity modifies the wavelength of both resonances. In detail, an increase of the periodicity yields a red-shift of both resonances due to the direct proportionality between the periodicity of a PC and its photonic bandstructure.

While the spectra reported in Figure 21 were acquired with normal light incidence, we also investigated the effect of different light incidence angles on the T_{PC} spectra. In their paper, Tikhodeev and coworkers showed that by changing the angle between sample and incident light it was possible to change number and position of the resonances[155]. The contour plot reported in Figure 22 shows that by rotating the sample, i.e. by changing the incidence angle of the light, it is possible to control shape and position of both resonances while mantaining their intensity unchanged, in good agreement with what reported in Tikhodeev's theoretical simulations. Specifically, the short-wavelength resonance slightly red-shifts symmetrically when changing the angle from 0° to ±10°. The long-wavelength resonance splits instead in 3 different peaks: the wavelength of the most intense peak does not change, while the other two peaks experience a wavelength shift of ~100 nm, symmetrically with respect to the first.

With these first results we demonstrated that PCs made with WS_2 show photonic properties that can be modulated by i) the design of the periodic structure and ii) by the angle of incidence of the light. Furthermore, we shown that ALD is a powerful tool that allows for exceptionally precise and controlled growth, that would not be possible on the same extent with other techniques. Moreover, the chalcogenization of ALD-deposited WO_3 overcomes the issue of TMD chemistry, allowing for a facile fabrication on material that are easy to etch with extreme control as transition metal oxides. Nevertheless, the great advantage of ALD with respect to other dry growth techniques is not only the remarkable control on thickness and composition of the material, but the possibility to have a perfectly conformal growth on a complex substrate

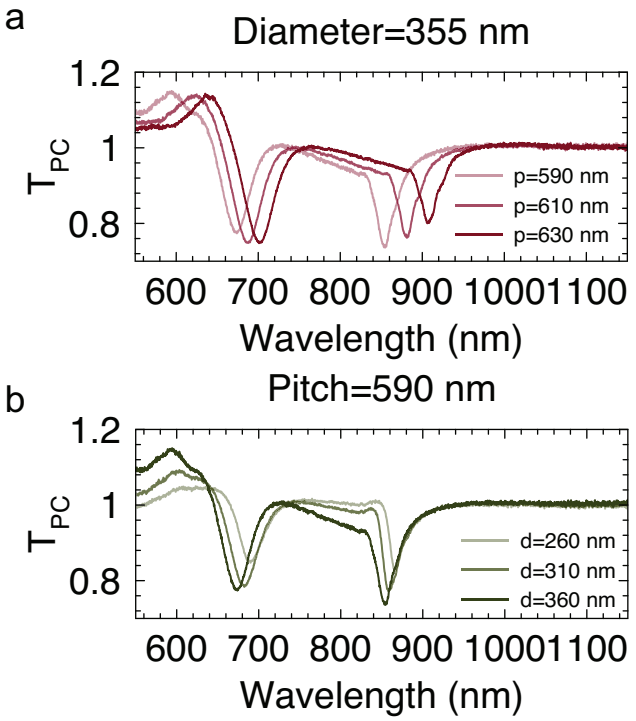

Figure 21: Light transmission properties of the 2D PC slab. a) Variation of T_{PC} as a function of the PC periodicity. As the periodicity increases from 590 nm (light red) to 630 nm (dark red), both the long- and short-wavelength resonances red-shift. b) Variation of T_{PC} as a function of the hole diameter. As the diameter increases from 260 nm (light green) to 360 nm (dark green), both the long- and short-wavelength resonances increase their intensity.

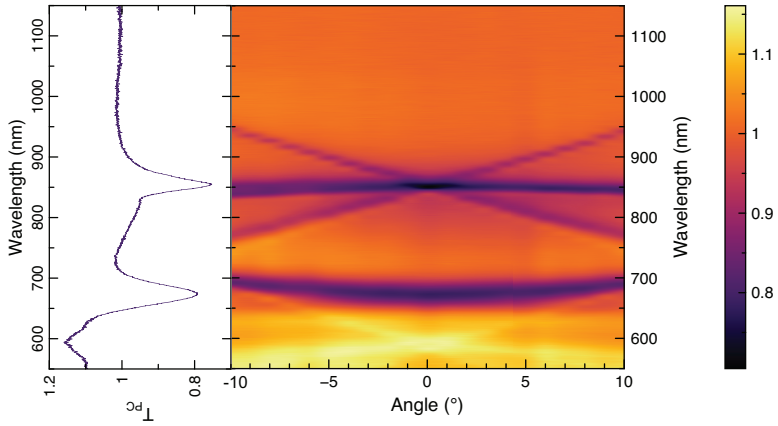

Figure 22: Light transmission properties of the 2D PC slab as a function of the light incidence angle. The sample is rotated from 0° to ± 10°. The short wavelength resonance slightly changes its wavelength from ~ 680 nm at 0° to ~ 700 nm at ± 10°. The long wavelength resonance splits in three different components. The most intense does not change, while the other two experience a symmetric ~ 100 nm splitting with respect to their wavelength at 0°. On the left-hand side is reported for reference a T_{PC} spectrum of the 2D slab acquired at an angle of 0°.

on high aspect ratios. Therefore, to exploit ALD to its full capabilities, we decided to fabricate a WS_2-based PC using a different approach, as will be shown in the next section.

4.4 CONFORMAL COATING OF A PRE-FABRICATED PC

While in Section 4.3 we synthesized a WS_2 film and then fabricated a PC into it, we decided to revert this approach by fabricating a PC into a low n substrate and then coating it with WS_2. We designed a set of 3x3 PCs by following the same scheme described in Figure 19. As a low n substrate we chose a fused SiO_2 wafer, because SiO_2 is an easily fabricatable material and can be etched with extreme control. We then fabricated the PC structures by EBL and subsequent etching of 100 nm deep holes with RIE. The n of SiO_2 is too low (~ 1.4) to give any measurable photonic properties and PCs fabricated in this way did not show any features in the transmission spectra. Thus, we needed to achieve the high index contrast by depositing a high n material on the SiO_2 substrate. To do so, we deposited on the low-n SiO_2 PC a thin layer of WO_3 using ALD, and we converted it to WS_2 using the same process described above. The schematic of the fabrication route is reported in

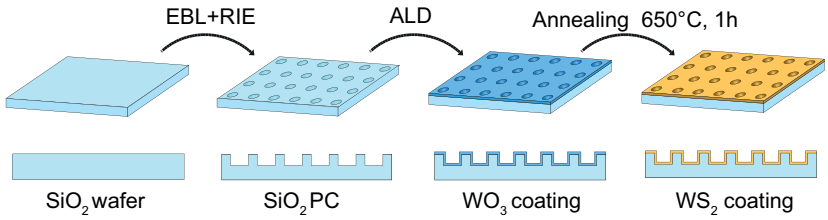

Figure 23: Schematic of the fabrication process for the conformally coated WS_2 PC. A PC is fabricated into a fused SiO_2 wafer and is then coated with a WO_3 film via ALD. The film is then chalcogenized at 650°C in presence of H_2S for 1 h to obtain the final WS_2 PC.

Figure 23. The top-view SEM micrograph of the fabricated structure is reported in Figure 20. The coverage of a low n PC with a high n material as WS_2 generates enough index contrast to have features in the transmission spectrum, as shown in Figure 24, where we report the transmission spectra of a 40 nm WS_2 PC as a function of PC periodicity and hole diameter.

Similarly to the 2D slab case, it is possible to tune the resonance wavelength by changing periodicity of the PC, and the intensity by fabricating PCs with different hole diameters, respectively. Moreover, the variation of the light incidence angle has an even larger effect on the transmission spectrum with respect to the 2D slab case, as shown in Figure 25. While the effect on the two major resonances is similar, it can be noticed that the different, more complex structure of the PC generates several less intense features, yielding a considerably more structured pattern. It should be noted that the transmission spectrum of the PC is dominated by two peaks that are totally analogous to those of the 2D slab. This suggests that the complex pseudo-3D conformal structure of the PC is dominated by the 2D in-plane slab component and that the inside coverage of the holes does not yield a large effect, but instead a set of minor features that do not affect strongly the overall transmission spectrum.

The conformal deposition obtained with ALD allowed for the investigation of the photonic properties dependency on the thickness of the WS_2 layer in a much faster and simpler way with respect to the 2D slab case. In the latter, we would have needed to first deposit various WO_3 films with different thicknesses, then fabricate a PC in each of them with EBL and RIE, and finally chalcogenize all of them to WS_2. The bottleneck would have been the fabrication step, that would have required a severe amount of time. Following the fabrication route we described in this chapter, i.e. using ALD to coat a pre-etched structure

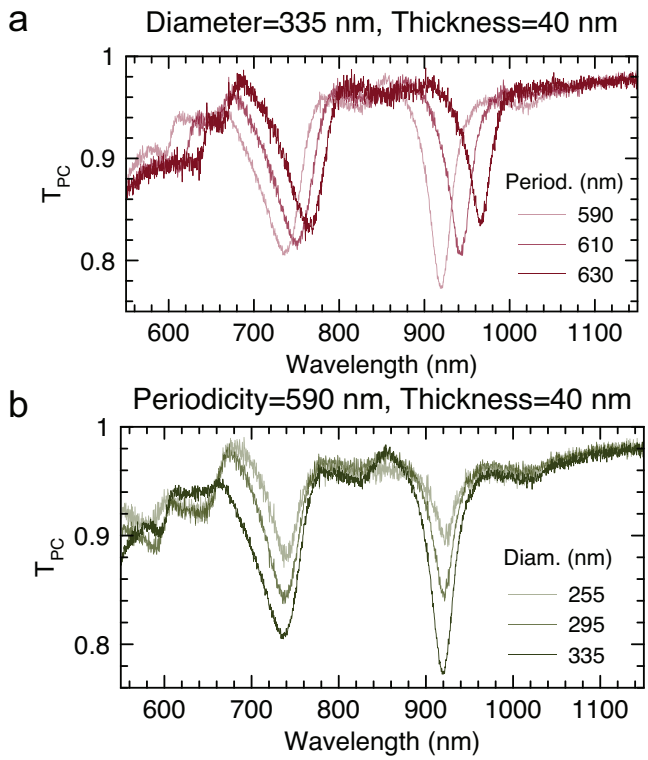

Figure 24: Light transmission properties of the conformally coated WS_2 PC. a) Variation of T_{PC} as a function of the PC periodicity. As the periodicity increases from 590 nm (light red) to 630 nm (dark red), both the long- and short-wavelength resonances red-shift. b) Variation of T_{PC} as a function of the hole diameter. As the diameter increases from 255 nm (light green) to 335 nm (dark green), both the long- and short-wavelength resonances increase their intensity.

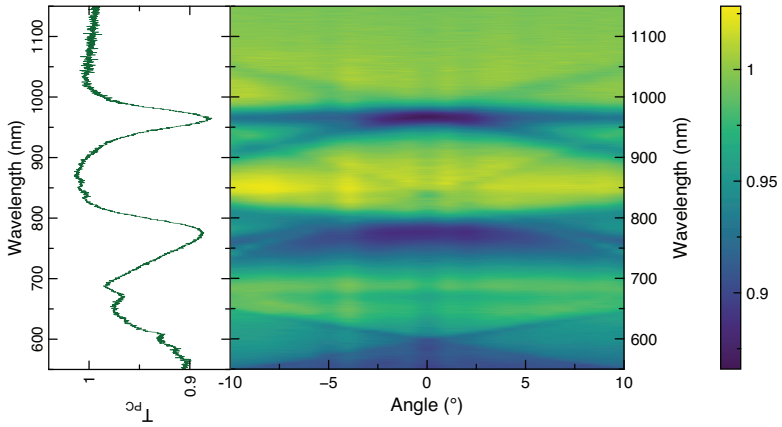

Figure 25: Light transmission properties of the conformally coated PC as a function of the light incidence angle. The sample is rotated from 0° to ± 10°. The short wavelength resonance does not change its wavelength, but underlying features can be detected with increasing angle. The long wavelength resonance splits in three different components. The most intense does not change, while the other two experience a symmetric ~ 100 nm splitting with respect to their wavelength at 0°. The overall contour plot shows a more complex pattern with respect to that of the 2D slab reported in Figure 22. On the left-hand side is reported for reference a T_{PC} spectrum of the PC acquired at an angle of 0°.

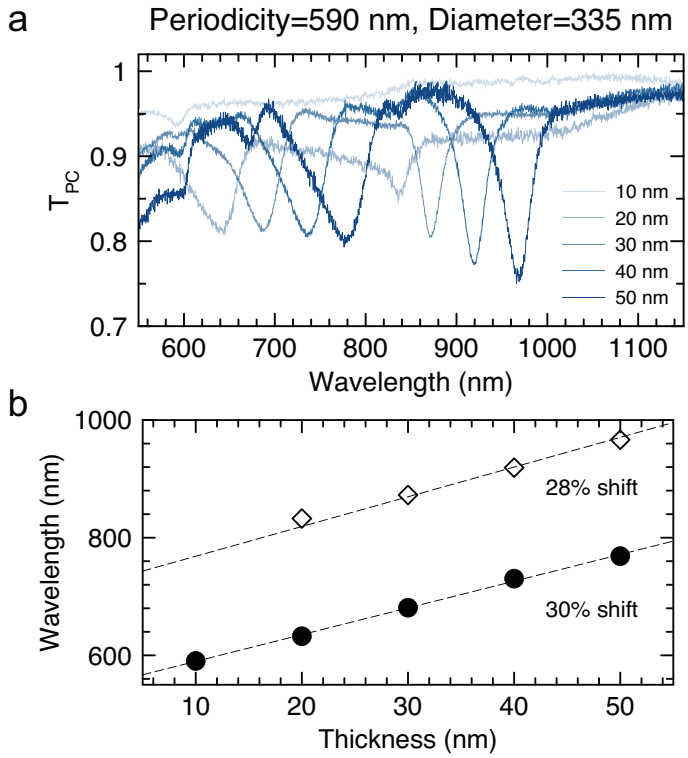

Figure 26: Light transmission properties of the conformally coated PC with increasing WS_2 thickness. a) Variation of T_{PC} as a function of the WS_2 film thickness, from 10 nm (lighter blue) to 50 nm (darker blue). As the thickness increases, both resonances become more intense and experience a red-shift. b) Red-shift for both resonances as a function of WS_2 thickness. The shift is about 200 nm, corresponding to ~ 30%, for both resonances.

on a low-n material, it was possible to perform only one EBL and RIE step and then to increase the WS_2 thickness by sequentially depositing a small amount of WO_3. Therefore we simplyfied the overall process and we were able to perform an accurate analysis of the WS_2 thickness effect on the light transmission properties of the PC. Following this strategy, we first deposited 10 nm of WO_3 on the SiO_2 wafer patterned with a PC made of holes with the same parameters as before, as shown in Figure 19. Then, we converted it to WS_2 and we measured the transmission spectrum. We then increased the thickness of the WS_2 to 50 nm by 10 nm steps. After each deposition/conversion cycle we measured the light transmission properties of the PC, as it is reported in Figure 26.

After the first deposition/conversion cycle, i.e. with WS_2 just 10 nm thick, only a weak resonance at 590 nm could be detected. The WS_2 film was too thin to yield significant coupling of light into the PC structure: the optimal thickness t to have light coupling in an ideal 2D slab is indeed[92]:

$$t \sim \frac{\lambda}{2n}, \tag{43}$$

where λ is the wavelength of the incident radiation. Therefore, for a resonance at 600 nm, where the n of our material is $n \sim 3.5$, the optimal thickness for the coupling of light into the material is ~ 85 nm. The presence of a resonance, although small, with just a 10 nm film indicated a strong coupling due to the high n of the WS_2. When the film thickness was increased to 20 nm, the resonance intensity dramatically increased and experienced a slight red-shift. A thicker WS_2 layer allows for a better coupling of the incident radiation into the PC, thus increasing the dip in transmission. Moreover, the thicker layer increases the effective n experienced by the incident light, thus shifting the resonance wavelength to longer values. In addition to the first dip in the transmission spectrum, a second resonance appeared at a longer wavelength (830 nm). Then, the thickness of the WS_2 layer was sequentially increased to 30 nm, 40 nm and 50 nm. After each step both the short-wavelength and the long-wavelength resonances red-shifted and increased their intensity. An analysis of the red-shift of the resonances as a function of WS_2 thickness shows that the trend is linear, as shown in Figure 26. The short-wavelength resonance shifts by 180 nm (from 590 nm to 770 nm), while for the long-wavelength resonance the shift is 190 nm (from 760 nm to 970 nm). These values correspond to a 30% and 28% shift in wavelength, respectively. Therefore, the thickness of the material has a strong effect on the light transmission properties of the PC. We could have proceeded towards larger WS_2 thicknesses, but we decided to stop at 50 nm. In Figure 26 it can be noticed that in the higher energy region, at around 600 nm, there is a feature that appears more intense with increasing thickness and is as intense as the resonances for the 50 nm film. This feature is caused by non-negligible absorption. At 50 nm coverage, the film starts to be severely absorbing. While T_{PC} is calculated by normalizing the light transmitted by the PC on an unstructured film of the same thickness, the conformal coverage of a prefabricated PC generates a coating on the inside of the holes. This hollow-cylinder-like shape, entirely made of WS_2, is about 100 nm deep and therefore strongly absorbs the incident light, and its contribution is not considered by the normalization operation that allows to calculate T_{PC}. While when the WS_2 thickness is low this contribution is still negligible, when the film starts to be thick it gets progressively

more intense until it is the dominant term. Therefore, we decided to stop the PC characterization after depositing the 50 nm thick film to avoid poor quality data with non-negigible errors in the measurement. However, our measurements demonstrated that it is possible to tune intensity and position of resonances in a wide spectral range in the Vis-to-NIR region of the electromagnetic spectrum just by conveniently changing thickness of the deposited material. With just 50 nm of WS_2 we were able to have a strong modulation of the photonic properties, validating the candidacy of TMDs as promising materials for photonics.

4.5 FDTD SIMULATIONS

To further investigate light-matter interaction in the complex photonic structure fabricated with the conformal deposition of WS_2 on a prefabricated PC in SiO_2, we simulated the structure with a 3D Finite Difference Time Domain (3D-FDTD) method using Lumerical software.[Lumerical FDTD solutions, http://www.lumerical.com] The material was simulated by using n and k obtained with spectroscopic ellipsometry and reported in Figure 17. A plane-wave broadband excitation source was simulated incident on the structure reported in Figure 27. The simulation allows for evaluating both transmission spectrum of the PC and mode propagation profiles for any chosen wavelength.

Field profiles are shown in Figure 28. The short-wavelength resonance has a quadrupole-like behavior: the electromagnetic field couples into the WS_2 film in a shape that has four lobes with maxima in the middle point between two neighboring holes. For the long-wavelength resonance the electromagnetic field behaves in a completely different way and it couples into the film in a sort of grating-like geometry, with maxima between each row of holes and parallel to the field polarization. A slightly localized state on the edges of the holes can be identified for the long-wavelength resonance, but it is worth noting that both of the resonances correspond to the coupling of the incident light into the 2D slab-like part of the PC, which is in agreement with the experimental result showing a transmission spectrum dominated by the 2D behavior. Moreover, it should be noted how the mode profiles we obtained from our FDTD simulations agree with those calculated by Tikhodeev with a completely different theoretical approach[155].

Simulated transmission properties for a set of PCs with pitch of 590 nm, 610 nm and 630 nm, hole diameter of 255 nm, 295 nm, 335 nm and 50 nm thickness are reported in Figure 27 together with experimental results. There are some discrepancies between theoretical and experimental spectra. Specifically, the simulated resonances are markedly more intense and narrower with respect to the experiment. The cause

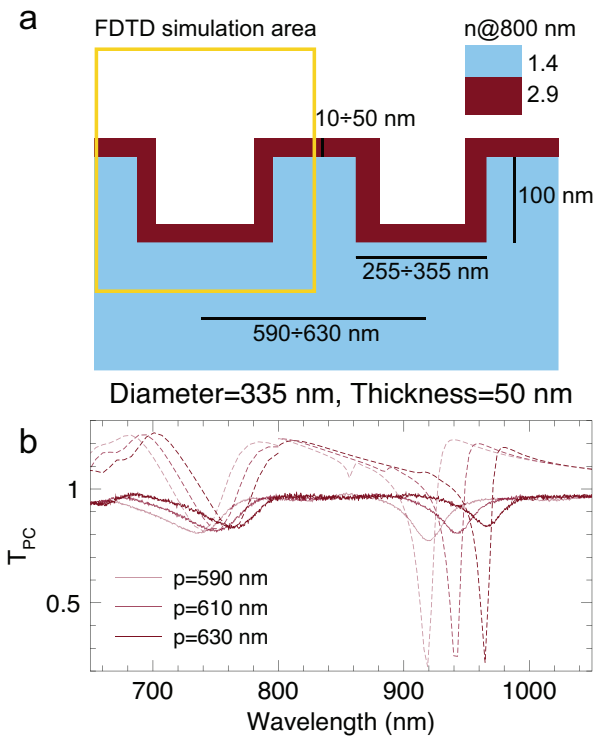

Figure 27: FDTD simulation of the conformal coated WS_2 PC. a) Schematic of the simulation area. b) Simulated T_{PC} curves (dashed lines) for a PC with 50 nm thickness and 335 nm hole diameter as a function of the PC periodicity from 590 nm (light red) to 630 nm (dark red). Solid lines are the measured T_{PC} curves for PCs with the same geometric parameters. The simulated peak position is in perfect agreement with the experimental case reported in Figure 24a.

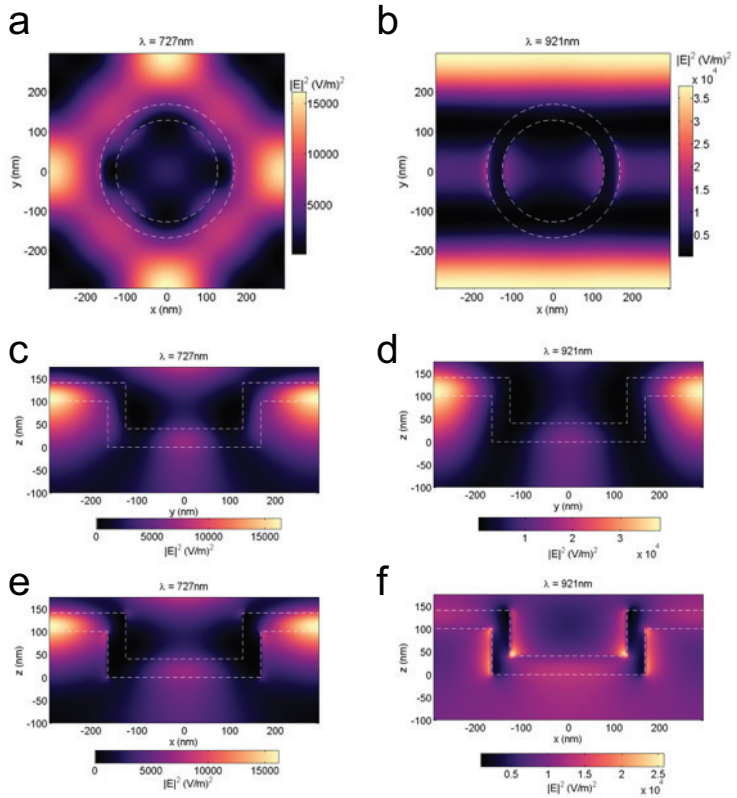

Figure 28: Simulated mode profiles for the short and long wavelength resonances in the conformal coated WS_2 PC. Left-hand side: short wavelength resonance. Right-hand side: long wavelength resonance. a),b) top view c),d) cross-sectional view from the y plane. e),f) cross-sectional view from the x plane.

of these differences has to be searched in the design of the FDTD simulation. The ideality of the design yields sharp and intense resonances, while defects in fabrication, morphology and in experimental setup determine broadening of the resonance FWHM. However, despite the mentioned discrepancies, it should be noted that the wavelength of the resonances are extremely well reproduced by the simulation and the wavelength shift with the PC periodicity perfectly traces the measured one. This remarkable result is not only a validation of the FDTD simulation in itself, but also of the spectroscopic ellipsometry measurement and data fitting we performed to obtain the WS_2 optical constants.

CONCLUSIONS

In this work, we have demonstrated that TMDs are a promising class of materials for the application to NIR photonics. First, they possess a surprisingly high n in the region of negligible k. This is a necessary, but not sufficient condition for a material to be interesting for photonics: a simple and reproducible synthetic route is also needed. While there is no easy way to directly fabricate PCs with a TMD, the chalcogenization of a transition metal oxide allows to go around this limitation. Thus, every fabrication step is performed on a "easy" material, that is then converted to the the final, high-n TMD.
Moreover, we have shown that ALD is an extremely powerful technique for both the synthesis of TMDs and the fabrication of PCs. The synthetic interest in ALD arises from the great control on morphology, thickness and composition of the deposited film. It is indeed possible to synthesize high quality thin films with sub-nanometer control on remarkably large areas. On the other hand, ALD is a precious tool for fabrication because it allows the perfectly conformal coating of virtually any substrate morphology and on surprisingly high aspect ratios.
We fabricated WS_2 PCs by following two different approaches. The first consisted in directly fabricating a 2D slab by etching a square hole lattice into a thin film. The second exploited ALD's conformal coating capacity to cover a pre-fabricated SiO_2 PC with a controlled thickness. In both cases, the high-n material was WS_2, that was synthesized at the end of the fabrication process by chalcogenizing a WO_3 film at high temperatures in a tube furnace.
The WS_2 film we synthesized showed very good optical properties, with a $n \sim 3$ in the transparency range. The n value is quite good if compared to other materials for photonics, but it can be improved with some synthesis optimization. PCs fabricated with both strategies show similar behavior, with two resonances that are indentified as dips in the light transmission spectra. The similar behavior suggests that in the case of the conformally coated PC the spectrum is dominated by the 2D slab-like structure, with some smaller effects given by the coverage of the vertical sides of the holes. We have shown that the PCs resonances can be modulated by changing the design, i.e. the geometric parameters of the PC (periodicity and hole diameter) and by tilting the sample with respect to the light incidence direction. Moreover, in case of the conformally coated PC, we demonstrated how increasing the WS_2 thickness has a dramatic effect on the light transmission prop-

erties, red-shifting both resonances by ~ 200 nm and drastically increasing their intensities.
This work demonstrates the possibility to coat an easily fabricated PC with a high-index material such as WS_2 by conformally depositing the corresponding oxide and subsequently converting it into TMD in presence of a chalcogenizing agent. To our knowledge, this is the first example of a PC based on TMDs. This procedure opens a wide range of possibilities that are not limited to photonics. We believe that the simple and inexpensive process presented herein is a promising way for the fabrication of high-index contrast PCs for applications in the visible and NIR range and that it could be combined with self-assembly process to have complete bandgap PCs in all the three spatial dimensions. For instance, the deposition of a thin transition metal oxide layer on a 3D PC based on polymeric beads in opaline configuration generates a filled inverse opal structure. The annealing in presence of a chalcogenizing agent has two effects: it converts the oxide to TMD and it removes the templating polymer by burning it, generating a 3D inverse opal structure made of hollow TMD spheres. This structure should have an extremely high n contrast, therefore showing a full photonic bandgap in 3D. Work is already in progress on this project and shows promising results.
Moreover, the validation of the candidacy of TMDs for photonics opens a new, unexplored line of research on TMD refractive index. A deeper insight in the TMD field is necessary in order to find a material with optimized optical constants for visible light applications.

Work at the Molecular Foundry was supported by the Office of Science, Office of Basic Energy Sciences, of the U.S. Department of Energy under Contract No. DE-AC02-05CH11231.

Part II

NANOMATERIALS FOR BIO-IMAGING AND SENSING

1

SELF-ASSEMBLED MICELLES FOR UP-CONVERSION BIOIMAGING

This work was performed in collaboration with the Stem Cell Laboratory in the Department of Pathophysiology and Transplantation - University of Milano.
Results of this work have been published:
S. Mattiello, A. Monguzzi, J. Pedrini, M. Sassi, C. Villa, Y. Torrente, R. Marotta, F. Meinardi, L. Beverina, "Self-Assembled Dual Dye-Doped Nanosized Micelles for High-Contrast Up-Conversion Bioimaging". *Adv. Funct. Mater.*, 26, 46, 8447-8454 (2016)

Fluorescence imaging is one of the most common approaches used on biological specimens for visual diagnostics[156–159]. However, even if this technique is extremely common *in vitro*, its application on human living patients is still impractical. Living tissues strongly absorb UV–vis radiation, that is needed to excite most of the available and affordable fluorescent probes[160]. As a consequence, practical applications require the use of high intensity sources, with two important consequences: increased scattering of excitation light and stronger background autofluorescence from tissues. The combined effect of those two issues significantly reduces the signal-to-noise ratio of optical detection, resulting in low-contrast images. Moreover, intense excitation light greatly increases potential damages to the tissues under investigation, thus making harmful an otherwise noninvasive technique. Many of the most advanced researches in this field aim at overcoming this critical issue. As depicted in Figure 29a, a possible solution is the use of materials showing anti-Stokes photoluminescence, i.e. the emission of photons at higher energy with respect to excitation[161]. This effect is known as photon up-conversion (UC), and it is commonly achieved through nonlinear optical phenomena like second harmonic generation or two-photon absorption (2PA). By exploiting UC, it is thus possible to eliminate autofluorescence background, present only at energies lower with respect to the excitation, with an increase in the image contrast, and enabling the use of low power, innocuous light sources. The

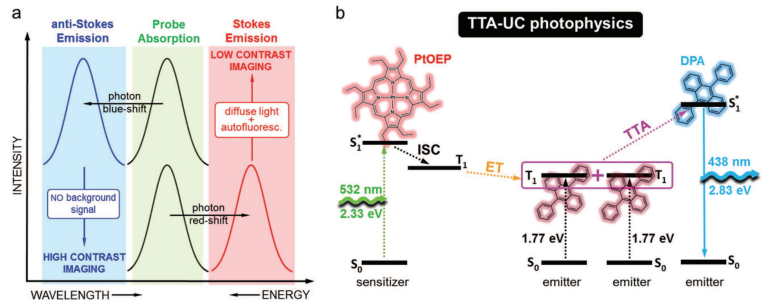

Figure 29: a) Outline of Stokes and anti-Stokes emissions for fluorescence imaging applications. b) Photophysics of the TTA-UC process using PtOEP as sensitizer and DPA as emitter. Dotted arrows indicate radiationless transitions. Upon absorption of a green photon, a sensitizer molecule is excited to its first singlet state that efficiently undergoes intersystem crossing into the triplet state. If efficient triplet–triplet ET occurs, the emitter dark triplets are populated before the radiative recombination of sensitizers. Subsequently, annihilation of two colliding emitter triplets (TTA) generates one high energy, fluorescent emitter in the excited singlet state, from which the blue UC emission occurs.

field of anti-Stokes fluorescence imaging was traditionally dominated by inorganic crystals doped with luminescent lanthanide ions and by organolanthanide complexes. In those systems, UC requires the sequential absorption of two or more photons exciting the metastable states of the emitting ions[162–165]. The anti-Stokes imaging based on lanthanides enables the use of infrared light excitation, which matches the transparency window of biological tissues. However, due to the small UC cross section of the exploited lanthanide electronic transitions, it requires the use of extremely intense excitation sources[161]. The same consideration is valid in materials for 2PA, where UC light is generated by the simultaneous absorption of two photons. Such approaches were successfully validated over the years for both in vitro and in vivo applications. Unfortunately, in both cases the required excitation irradiances are typically in the order of[166] MW cm^{-2}.

Conversely, UC based on sensitized triplet–triplet annihilation (TTA-UC), recently proposed as an efficient photon managing technique for solar applications, can efficiently occur[163,166–169] at excitation irradiances of few mW cm^{-2}. TTA-UC is a stepwise process which exploits the annihilation of optically dark, metastable triplets of an emitter to produce high-energy singlets, that generate the up-converted emission. These metastable triplets are optically dark and can only be indirectly populated via energy transfer from a proper sensitizer moiety, that plays the role of the photon harvester.
As detailed in Figure 29b, TTA-UC requires a pair of selected chro-

mophores with suitable electronic properties. Here, we used Pt(II)-octaethylporphyrin (PtOEP) as sensitizer and 9-10-diphenylanthracene (DPA) as annihilator/emitter. PtOEP can be excited to its first singlet excited state by irradiation at 532 nm. After absorption, PtOEP experiences intersystem crossing, which almost istantaneously converts the photogenerated singlet excited state to a low-lying triplet. If, within the lifetime of this latter, the sensitizer collides with a ground state DPA, the two molecules undergo triplet–triplet energy transfer (Dexter ET) that results in the excitation of the emitter in its first triplet state. Finally, the collision of two emitters, populated via ET in their triplet states, leads to the promotion of one of them in the first, fluorescent singlet excited state through triplet-triplet annihilation (TTA). It is worth pointing out that, since the triplets of the dyes usually employed as emitters are long-living states with typical natural lifetime in the range of hundreds of milliseconds and more, the annihilation is exceptionally efficient, resulting in effective UC also at extremely low excitation light intensity. This allowed proving TTA-UC with a range of molecule pairs operating in different spectral windows in organic solvents[170–176]. UC-light activated drug release was also demonstrated[171,177,178]. The need to extend this phenomenon to water environment and to biological specimen triggered remarkable efforts in the preparation of TTA-UC structures. Among them, active polymeric structures[179–184], ionogels[185], liposomes[178,186,187], diverse supramolecular approaches[179–184], oil in water microemulsions[188–190], dendrimers[191], micelles[192], and water dispersible nanoparticles[193,194] and nanocapsules[195–201] led to demonstration of the applicability of TTA-UC both in vitro and in vivo, within the tissue transparency window[164,165,193,195,197]. Nowadays, the full exploitation of TTA-UC in bio-related applications remains challenging due to two major issues. First, molecular oxygen is an excellent quencher of triplet states, and therefore its presence quickly switches off the TTA-UC process. This sets a very critical requirement, as in biological tissues oxygen tension is around 0.5–2.5 kPa, to be compared with its equilibrium value in air of 21 kPa[202]. TTA-UC is actually so sensitive that it was recently used in the preparation of oxygen sensing materials with a particularly broad dynamic range[203]. Second, sensitizers and emitters need to be in close proximity to efficiently undergo short-range interactions such as ET and TTA. The literature reports several approaches to tackle this limit.

Encapsulating the two active molecules within a polymeric shell provided working UC capsules, having dimensions ranging from hundreds of nanometers to microns[195,198]. Step by step assembly of structures featuring a liquid or a low viscosity core surrounded by a silica shell provides an elegant approach to solve both issues at the same time, while maintaining the dimensions of the final TTA-UC nanostruc-

ture within the nanometric range[190]. Encapsulation in other inorganic matrices like tungsten oxide, in this case for photocatalysis applications, was also demonstrated[194]. The approach is general and versatile, yet somewhat complicated by its multistep nature. Oil in water microemulsions, requiring an organic solvent based inner phase, also offer a viable and general way to prepare colloids that show efficient TTA-UC in oxygenated environments[188189]. Recently, Yanai and coworkers demonstrated that synthesis and water phase self-assembly of amphiphilic cationic acceptor molecules with anionic donor (sensitizer) molecules provide an efficient way to address the oxygen quenching issue by a purely supramolecular approach[180]. Finally, König and coworkers demonstrated efficient TTA-UC in large unilamellar vesicles loaded with suitably functionalized diphenylanthracene derivatives as well as both PtOEP and a Ru bipyridine complex[186]. Unfortunately, all of the aforementioned approaches require either the synthesis of specifically designed chromophores, the incorporation of organic solvents, or a complex multistep fabrication of appropriate nanovectors, and therefore they can be in many cases impractical.

In this work, we demonstrate an extremely simple procedure for the preparation of efficient TTA up-converting nanomicelles (UC-NMs) based on the use of the commercially available surfactant Kolliphor EL, one of the most commonly employed emulsifier for water insoluble drugs. Moreover, Kolliphor EL is the key excipient of several FDA (Food and Drug Administration) approved preparations including Paclitaxel and Miconazole[204]. Our protocol enables the synthesis of stable nanomicelles loaded with a proper dye pair for green-to-blue UC. The inclusion of the dyes in the micelles preserves UC performances in oxygenated deionized water as well as in phosphate-buffered saline (PBS) solution used in biological research. Moreover, Kolliphor EL guarantees for a high biocompatibility of these supramolecular optical probes.

1.1 METHODS

1.1.1 *UC-NM Synthesis*

1,2-propanediol and KH_2PO_4 were purchased from Merck. Na_2HPO_4 was purchased from Alfa Aesar. Deionized water was purchased from Carlo Erba. All the others starting materials were purchased from Sigma-Aldrich. All materials and solvents were used as received. 13.50 mg of DPA and 0.30 mg of PtOEP were dissolved in 10 mL of THF, then 220 mg of 1,2-propanediol/Kolliphor EL 3:10 v/v mixture were added to 2 mL of the starting solution. The obtained solution was son-

icated for 30 min in a SONICA 3200 EP ultrasonic cleaner, then THF was removed under reduced pressure and the oily residue was taken up either with 15 mL of deionized water or PBS solution. PBS solution was prepared dissolving 80 g of NaCl, 14.4 g of Na_2HPO_4, 2.4 g of KH_2PO_4, and 2 g of KCl in 1 L of deionized water, and diluting 10 times before use.

1.1.2 *UC-NM Structural Analysis*

Up-conversion nanoparticles once applied in thin film on glow discharged holey TEM grids were plunge frozen in liquid ethane cooled at liquid nitrogen temperature using a FEI Vitrobot Mark IV semi-automated cryoplunger. CryoEM projection images and single-axis tilt series were recorded in low dose using an FEI Tecnai G2 F20 Schottky field emission gun transmission electron microscope, equipped with automated cryobox, and a Gatan Ultrascan 2kx2k CCD (Charge-Coupled Device) detector. The tilt series were acquired from ±60° with a tilt angle of 2° at a magnification of 29000x (pixel size of 0.39 nm) with a total electron dose between 60 and 80 $e^{-}Å^{-2}s^{-1}$.

1.1.3 *Photophysical Studies*

Absorption spectra were acquired with a Cary 50 spectrometer in normal incidence conditions using quartz Suprasil cuvettes. Continuous wave (CW) photoluminescence (PL) signals were recorded by a nitrogen cooled CCD coupled with a double monochromator Triax-190 (Horiba Jobin-Yvon), with a spectral resolution of 0.5 nm. The recorded spectra were corrected for the setup optical response. The excitation intensity threshold was measured by modulating the power of a CW 532 nm doubled Nd:YAG laser Coherent Verdi V10. The excitation laser beam is Gaussian shaped, and the spot diameter, containing 90% of the intensity, was 340 μm. Shape and spot size were measured by the knife-edge method. Time resolved PL measurements were performed by modulating the 532 nm laser with a TTi TG5011 wavefunctions generator, with a time resolution better than 0.1 μs (5 ns pulse width). Time resolved PL spectra were detected in photon-counting mode using an ORTEC digital multichannel scaler, with a temporal resolution of 0.1 ns. Images of UC-NM/phalloidin stained 3T3 cells were acquired with a Nikon C1 confocal microscope coupled with the 532 nm laser focused on the sample with a 60x (1.4 NA) immersion oil objective. The spot size in this configuration is 460 nm. The fluorescence intensity was filtered with blue- and red-pass dichroic mirrors and detected with two photomultiplier tubes with independent gain, in order to record the

UC-NM up-converted blue luminescence and the phalloidin red fluorescence, respectively.

1.1.4 *Cell Culture and Staining*

Protocols: 3T3 cells (ATCC CRL-1658) were thawed and plated on cell culture dish in DMEM high glucose (Gibco) supplemented with 10% FBS (Fetal Bovine Serum, Euroclone) for 48 h before use. For immunofluorescence experiments, 3T3 cells were detached with 0.25% Trypsin (Gibco), resuspended in complete medium and plated in 12-well plates at a density of 5×10^4 cells per well. After 24 h from seeding, UC-NMs were added to the cells at different concentration of the mother solution (1:10, 1:50, and 1:100). 24 h after labeling, cell viability was assessed by performing live dead fluorescent assay (Thermo Fisher), in accordance with protocol by manufacturer. Briefly, Calcein-AM (green-Live) and ethidium homodimer-1 (red-Death) were diluted 1:1000 in complete medium and incubated for 30 min at 37 °C. Cells were then washed twice with PBS (1×, Gibco) and visualized with an inverted fluorescent microscope (Leica). 1:2000 Hoechst counter staining was performed for nuclei visualization. In order to visualize UC-NM uptake within cells, actin cytoskeleton was labeled with phalloidin tetramethylrhodamine B isothiocyanate (TRITC). 3T3 cells were washed with PBS, fixed with 4% formaldehyde solution for 4 min, washed twice, and permeabilized by 0.1% Triton X-100 in PBS. After washing in PBS, cells were incubated for 30 min with 50 $\mu g\ mL^{-1}$ fluorescent phalloidin conjugated solution; afterward they were extensively washed before visualization. Unlabeled cells were used as control. Since the concentration 1:50 was shown to maintain both a good cell viability and a high number of detectable nanoparticles, further experiments considered 1:50 up-converting nanomicelles labeled 3T3 cells throughout time (24, 48, 72 h after labeling).

1.1.5 *Cell Viability and ROS Test*

For proliferation experiments, cells were seeded in a 96 well plate at 3×10^3 cells per well density in triplicate (n = 3 wells for each time point). Evaluation of ROS production from cells was performed 24, 48, and 72 h after 1:50 UC-NM labeling. ROS-Glo H_2O_2 Assay (Promega) was used, following the producer protocol. Cells treated with 50×10^{-6} M menadione were considered as positive control, while growth medium were reported as negative control. The nonlytic protocol was applied for proceeding with additional evaluations on the same cells assessed for ROS production. Specifically, the cell titer glow viabil-

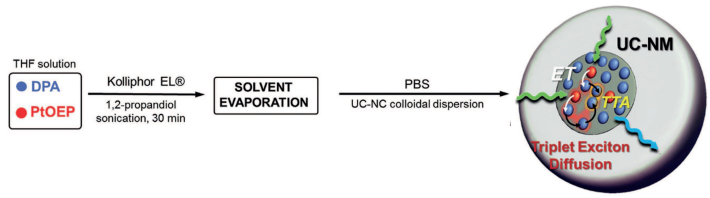

Figure 30: Outline of the UC-NM self-assembly reaction scheme and sketch of the TTA-UC process in a single UC-NM. Up-converted photons are generated thanks to the diffusion (black arrows) and annihilation (TTA) of sensitized dark triplet excitons among the network of acceptors (DPA, blue dots) embedded in the Kolliphor EL micelles.

ity assay (Promega) was performed following the datasheet instruction. The CellTiter-Glo 3D Cell viability assay is a homogeneous method to determine the number of viable cells based on quantitation of the ATP (Adenosine Triphosphate) present, which is a marker for the presence of metabolically active cells. For both ROS and cell titer glow assays, relative luminescence units were measured by a plate reader (GloMax Discover, Promega).

1.2 UC-NM PREPARATION

We selected PtOEP and DPA as model sensitizer and emitter because they are amongst the most investigated and best performing chromophores for TTA-UC[199]. Figure 30 sketches the self-assembly strategy followed for the preparation of UC-NMs aqueous dispersion. The first step consisted in the preparation of a tetrahydrofuran (THF) solution of PtOEP (40×10^{-6} M) and DPA (4000×10^{-6} M), in the stoichiometric ratio of 1:100, which is the preferred feeding ratio to observe efficient TTA-UC in solution[205]. Then we added to this solution Kolliphor EL and 1,2-propanediol under sonication and we maintained the solution in the ultrasound bath for 30 min. All volatiles were evaporated and the oily residue was taken up either with deionized water or with PBS (Phosphate-buffered saline) solution to give a limpid UC-NMs stable dispersion with no appreciable haze. The absence of scattering suggests the lack of undesired aggregates. A precise estimate of the micellar size was obtained by means of high-resolution Cryo-TEM (Transmission Electron Microscopy) measurements, that was chosen to avoid the collapse of the micellar structure due to the removal of the dispersing medium. Indeed, Cryo-TEM images (Figure 31) show a series of spherical objects, with a monodisperse diameter distribution peaked at 6.2 nm (inset). Given the affinity of DPA and PtOEP with the emulsifier en-

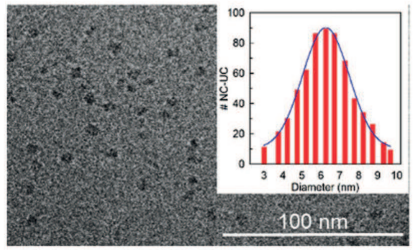

Figure 31: Cryo-TEM images of UC-NMs loaded with a 100:1 DPA:PtOEP cargo. The inset reports the size distribution of the micellar diameter, peaked at 6.2 nm.

vironment, and considering their insolubility in the aqueous medium, these spheroids likely correspond to the amorphous blend of Kolliphor EL, PtOEP, and DPA.

To verify the presence of both sensitizers and emitters, we recorded the UV–vis absorption of the dispersion. As reported in Figure 32 (black line), the UC-NMs spectrum shows the fingerprint absorption peaks of DPA, i.e. the broad band centered at 380 nm characterized by a well-defined vibronic structure[206], and of PtOEP, with a weak narrow band centered at 535 nm[207]. The data suggest that both molecules form a stable solution within the Kolliphor EL matrix. Therefore, we can assume that the incorporation of DPA and PtOEP is not selective toward one of the two components. The final demonstration of the successful chromophores loading in the Kolliphor EL nanomicelles was obtained by recording the photoluminescence (PL) spectrum of the suspension under a laser excitation at 532 nm, matching the PtOEP absorption. Figure 32 shows that, beside a residual sensitizer phosphorescence at 645 nm due incomplete ET (red line), we can detect the typical blue emission of DPA (blue line) thanks to the effective UC of the harvested photons. This suggests that sensitizer and emitter moieties are closely packed in the UC-NMs core, allowing TTA-UC through exciton diffusion in the dyes framework defined by the micellar volume, with no need for molecular motion, as sketched in Figure 30. To support this view, we performed a simple stochastic simulation of the spatial distribution of DPA molecules in a sphere of 6.2 nm radius, in order to have an approximate estimate of the intermolecular distance. Figure 33 shows the result of Monte Carlo calculations performed using 56 DPAs per UC-NM and imposing a minimum center-to-center intermolecular distance of 1.0 nm (in accordance with the steric hindrance of the DPA whose molecular radius is 0.45 nm). All the dyes have a nearest-neighbor closer than 1.3 nm and a next-nearest-neighbor closer than 1.5

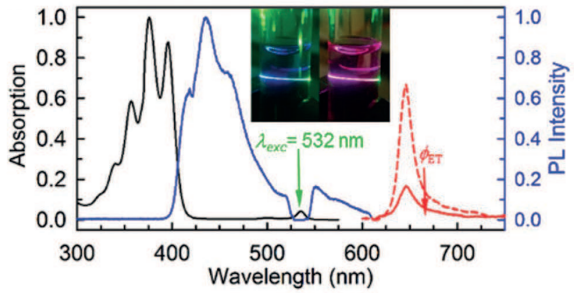

Figure 32: Absorption (black line) and PL (blue line) spectrum of UC-NM under 532 nm laser excitation. The red spectra show the sensitizer (PtOEP, red dots) phosphorescence in presence (solid line) and in absence (dashed line) of the acceptors in the NC. The inset reports a photograph of the UC-NM dispersion in PBS under 532 excitation with (left) and without (right) a high-pass blue filter

nm. These values are comparable with the distances at which the exchange interactions are effective[205], confirming that excitation energy can migrate via exchange-mediated homomolecular hopping within the ensemble of emitters exploring the micellar volume to experience TTA. The resulting TTA-UC luminescence can be observed also by the naked eyes using a high-pass optical filter, as showed by photographs of the sample (inset of Figure 32).

1.3 UC-NM CHARACTERIZATION AND PERFORMANCE ANALYSIS

One of the most critical properties required for UC-NMs to operate in an aqueous medium is the strong ability to shield chromophores from environmental oxygen. To test this feature, we recorded UC intensity I_{uc} at different times, while leaving the sample in aerated conditions. As shown in Figure 34, after a 20% drop observed during the first 4 h, I_{uc} remains constant up to 10 h, demonstrating remarkable resistance of UC-NMs, as also observed for other self-assembled structures[208]. The initial decrease of I_{uc} can be simply determined by a progressive consumption of the oxygen embedded in the UC-NM during the synthesis.

If we now consider efficiency, the UC quantum yield QY_{uc} in a TTA-UC system is generally poor at very low excitation intensity I_{exc}, but it becomes higher when the incident light intensity is increased, and then it saturates to a maximum value. We measured a noteworthy QY_{uc} ~6.5% in UC-NMs filled with the largest tested concentration of PtOEP and DPA (400 and 4000 × 10^{-6} M respectively; in this case we used a 1:10 ratio instead of the 1:100 employed so far due to the limited

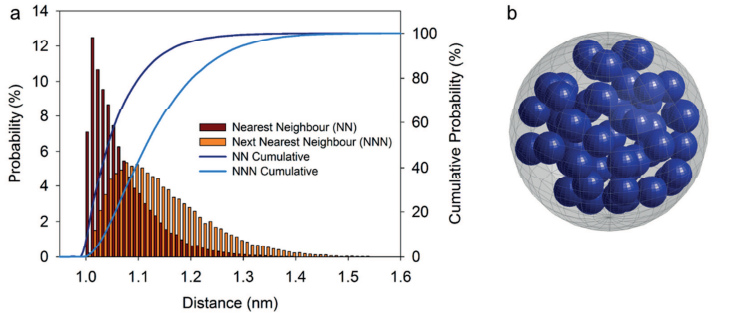

Figure 33: Monte Carlo simulations of UC-NMs. (a) Histogram of the intermolecular stochastic nearest-neighbor (NN) and next-nearest-neighbor (NNN) distance distribution of an ensemble of 56 DPA molecules embedded in a spherical UC-NM of radius 6.2 nm. The continuous line are the corresponding cumulative probabilities. (b) One example of the 105 randomly generated distributions. 56 is the average number of DPA molecules in a micelle, calculated as the ratio of the total number of DPA molecules to the estimated number of micelles. The number of micelles is calculated as the ratio of the total volume of Kolliphor EL (0.15 cm^3) to the average volume of a single micelle, based on the diameter obtained from DLS measurements (15 nm).

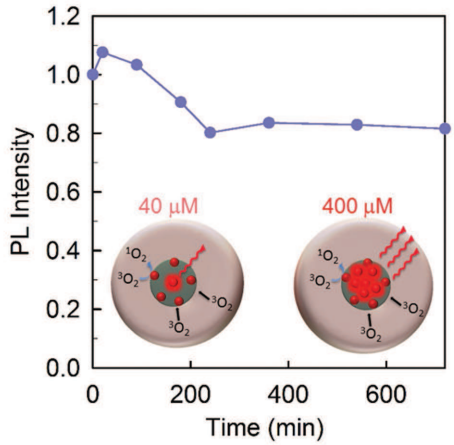

Figure 34: Air stability of UC-NMs. Time dependence of UC emission intensity at 435 nm upon continuous excitation at 532 nm of the as prepared UC-NM sample (PtOEP 40 $\times$ 10^{-6} M) in aerated conditions. The inset illustrates the PtOEP molecule distribution in the UC-NM structure with an initial doping concentration of 40 $\times$ 10^{-6} and 400 $\times$ 10^{-6} M.

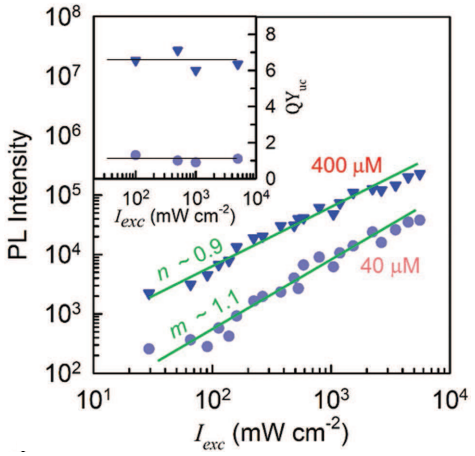

Figure 35: Double logarithmic plot of the UC emission intensity for UC-NM dispersions prepared using 40 × 10^{-6} (dots) and 400 × 10^{-6} M (triangles) of the sensitizer PtOEP, as a function of the excitation intensity I_{exc} at 532 nm. The solid straight lines show the fit of the experimental data with a linear function with slope m and n, respectively. Inset: UC yield QY_{uc} measured at different excitation intensities.

solubility of DPA in the micelles). Moreover, importantly, UC-NMs are in saturation regime for every irradiance above few tens of mW cm^{-2}. This is demonstrated by the linear dependence of the TTA-UC emission versus I_{exc}, which also corresponds to a constant QY_{uc} (see Figure 35, triangles). Even if such a value is definitely high enough to enable in vitro fluorescence imaging experiments (see below), it is lower with respect to a liquid solution of PtOEP/DPA with the same concentrations, in which QY_{uc} ~20%[209]. This discrepancy requires some additional comments, especially in view of a future optimization of this class of materials. For an ideal system, the maximum QY_{uc} obtained in the high excitation limit depends only on the sensitizer-to-emitter ET efficiency and on the statistical probability f to obtain a singlet state upon annihilation of two triplets[209]:

$$QY_{uc} = \frac{1}{2} \times f \times \Phi_{ET}, \tag{44}$$

where $\frac{1}{2}$ indicates that two low energy states are required for generating a high energy one, and f is ~1/2. In our system we measured Φ_{ET}= 55%, which implies a QY_{uc} around 12.5%, two times larger than the observed value. To justify this discrepancy, and considering that Φ_{ET} is not as high as expected for the employed dyes concentration, we investigated the dyes distribution within the nanomicelles. To this aim,

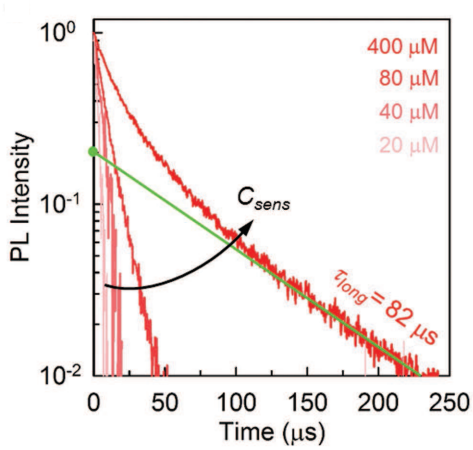

Figure 36: Time-resolved PL decay at 645 nm measured for a series of NMs prepared with different PtOEP initial concentrations C_{sens} and with no DPA.

we prepared two distinct series of UC-NMs. In both of them we varied the sensitizer concentration C_{sens} in an interval between 20×10^{-6} and 400×10^{-6} M. In the series we labeled as *series A* we did not introduce DPA molecules, while in the one labeled *series B* DPA concentration was 4000×10^{-6} M.

Samples belonging to series A show striking differences in their respective PtOEP luminescence decay dynamics. Figure 36 shows the time-resolved PL decay recorded at 645 nm as a function of C_{sens}. At the lowest PtOEP concentration (20×10^{-6} M), the PL decay is notably faster (~3 μs) than the intrinsic PtOEP radiative lifetime (120 μs)[210]. This effect is typical of oxygen quenching, meaning that even though PtOEP molecules are effectively embedded in the NMs, they do not localize within the dense and hydrophobic core where, according to our data, no oxygen is present. Conversely, they probably rather localize at the interface between the oleic core and the polyethyleneglycol hydrophilic shell (see inset of Figure 34). By increasing PtOEP concentration, its PL lifetime progressively lengthens and becomes clearly non-exponential. In the sample with $C_{sens} = 400 \times 10^{-6}$ M the PL long-time component is $\tau_{long} = 82$ μs (green solid line), comparable to the PtOEP decay time usually observed in de-oxygenated organic solvents[211]. This behavior suggests that PtOEP molecules preferentially accommodate on, or very close to, the micelle surface, where the interaction with the ambient oxygen are not fully prevented. The need to include a higher number of PtOEP molecules per single nanomicelle pushes more PtOEP within the micelle's anoxic core, as sketched in the

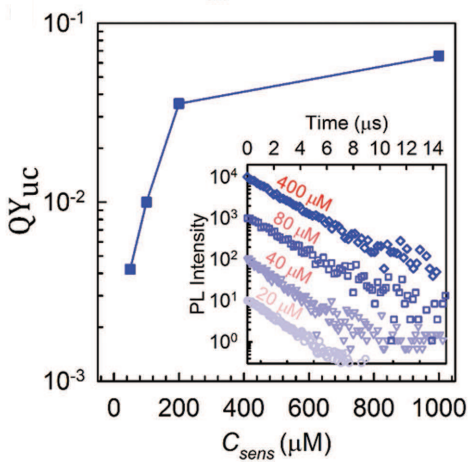

Figure 37: QY_{uc} for a series of UC-NMs with a fixed DPA initial concentration (4000×10^{-6} M) as a function of C_{sens}. Inset: up-converted light decay at 435 nm for each sample.

inset of Figure 34. The same phenomenology is expected to hold also for DPA molecules, even though it is not directly detectable: the oxygen sensitive triplet state of this dye is completely dark and no upconversion occurs in presence of quenching agents. Following this picture, not every porphyrin is effective as a sensitizer for the UC process, but only those inside the NM core can efficiently transfer the excitation to properly included DPA molecules.

Based on the results we obtained with series A samples, we expected a substantial enhancement of the nanomicelles average TTA-UC capabilities by using a high C_{sens}. Measurements on series B samples support our general view. Figure 37 reports the QY_{uc} values measured as a function of C_{sens} showing that the conversion yield increases from less than 1% in the sample with $C_{sens} = 20 \times 10^{-6}$ M to 6.5% for the 400×10^{-6} M sample. These findings suggest that the limited QY_{uc} we observed is not related to an inefficient TTA-UC photophysics in the UC-NM environment, but rather on a still not completely optimized distribution of PtOEP within each single NM structure. This conclusion is strongly supported by time-resolved data of TTA-UC emission reported in the inset of Figure 37, which show that the dynamics of the upconverted PL is exactly the same regardless of C_{sens}, i.e. regardless of the overall efficiency of the system. These data prove that, if incident photons are absorbed by molecules correctly embedded in the NMs structure, TTA-UC occurs always in the same, highly efficient way. In

contrast, the NMs embedding unprotected dyes are basically inactive as up-converters.

1.4 UC-NM FOR IN VITRO FLUORESCENCE IMAGING

In order to demonstrate the applicative potential of UC-NMs, and to verify their stability in biological media, we performed in vitro labeling of 3T3 murine fibroblast cell. First of all we proved the absence of any cytotoxic effects induced by the UC-NMs by performing a cell viability assessment by means of Live/Dead staining on cells labeled with increasing nanomicelle concentrations, as reported in Figure 38. At high UC-NM concentration (1:10), the micelle signal can clearly be detected, but it can be seen that the majority of cells is dead. Conversely, when the concentration is too low (1:100), cell proliferation is not affected, but the UC-NMs are barely visible. The 1:50 dilution of the mother solution gave the best trade-off between good cell viability, without signs of stress and cell injuries, and UC-NMs concentration providing satisfactory fluorescence imaging.

Accordingly, we tested this concentration for further experiments to evaluate UC-NMs cytocompatibility throughout time. One of the most frequently reported nanoparticle-associated toxicities is the generation of reactive oxygen species (ROS), chemically reactive compounds that are formed as by-products of cellular oxygen metabolism. However, environmental stress factors such as exposure to intense light or excessive heating, common consequences of a prolonged irradiation in diagnostic circumstances, can increase intracellular ROS concentration to cytotoxic levels, causing damage to cell structures and possible cell death[212]. Moreover, oxidative stress induced by the staining with nano-objects can cause further pathophysiological effects including genotoxicity, inflammation, and fibrosism, as demonstrated by activation of associated cell signaling pathways[213]. Since oxidative stress is a key determinant of UC-NM-induced injury, it is necessary to characterize ROS response resulting from the labeling. Cell Titer-Glo viability and ROS evolution assessments have been performed on labeled 3T3 cells throughout 72 h. Figure 39 show results of viability and ROS tests, respectively. Although CellTiter-Glo shows a slower proliferation rate for UC-NM labeled cells compared to the unlabeled control sample (P value < 0.005, for 24, 48, and 72 h), the overall labeled cell viability has been maintained constant through the experiment course. In the same time, the amount of ROS released from labeled 3T3 cells has been kept on physiological levels, since ROS production test displayed no difference between control and stained samples, confirming the highly biocompatible composition of UC-NMs. Finally, we proceeded to ac-

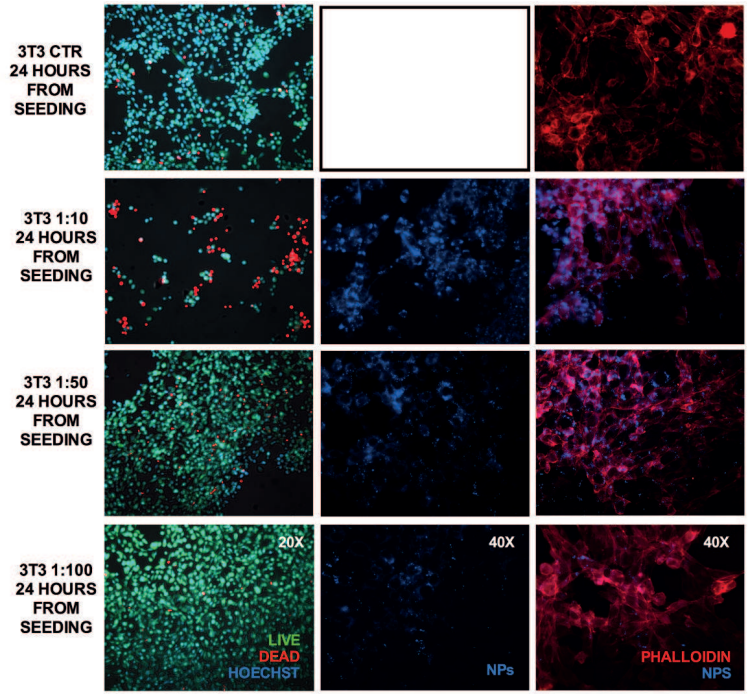

Figure 38: (left) Live/Dead test results on 3T3 fibroblast stem cells stained with Hoechst. (center) Fluorescence imaging of 3T3 cells stained with UC-NMs under UV excitation. (right) Fluorescence imaging of 3T3 cells stained with UC-NMs (blue) and phalloidin under UV excitation.

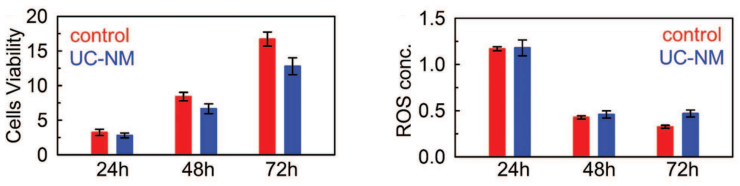

Figure 39: a) Cell titer glow viability test and b) ROS test on 3T3 cells stained with UC-NMs at 1:50 dilution of the mother solution, monitored at three time points (24 h, 48 h, and 72 h, respectively).

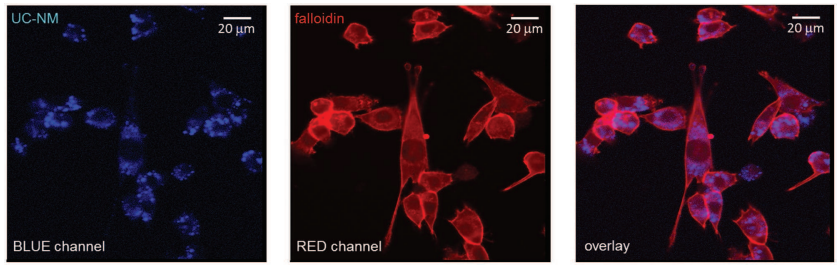

Figure 40: Confocal fluorescence image of 3T3 cell stained with UC-NMs (blue) and phalloidin positive F actin (red) under laser excitation at 532 nm.

quire fluorescence confocal microscope images of paraformaldehyde fixed 3T3 cells stained with UC-NMs (blue) and phalloidin positive F actin (red) using a green laser excitation at 532 nm. As shown in Figure 40, we can clearly observe that blue UC light is generated in the cytoplasm region, mostly around the cell nucleus, as expected for dyes not functionalized with target-specific ligands. In contrast, phalloidin is a well-known standard dye employed for specific staining of the cytoskeleton. Therefore, thanks to the overlay of blue and red channels of the optical detector, we are able to record a nice, high-contrast, dual-channel image of the 3T3 cells by using the same excitation source. This colocalization staining clearly shows that the UC-NMs are effectively internalized by the 3T3 cells, leading to a perinuclear localization and confirming their good stability in the biological medium. This result is the first demonstration of the efficient staining of cells with a TTA-UC based anti-Stokes emitter prepared through such a simple formulation approach employing FDA approved materials. These remarkable results are promising in perspective of UC-NM applicability as optically active systems for advanced theranostic applications. The observation of UC emission indicates not only that the nanomicelles effectively work as photon up-converters, but it is also an evidence of the structural stability of the micellar structure. As TTA-UC and the corresponding signal would be lost in case of UC-NMs collapsing, this optical feedback could be used to image the controlled release of water-insoluble additional payloads embedded within the micelles[157].

1.5 CONCLUSIONS

In summary, we demonstrated a simple and general approach for the preparation of water dispersible, self-assembled nanomicelles loaded with a sensitizer/emitter chromophores pair, which show efficient sensitized up-conversion emission at low excitation power. Thanks to a

deep analysis of their optical properties, we were able to optimize the synthesis protocol and obtain nano up-converters with an efficiency of 6.5% in aqueous, oxygenated environment. The stability of these anti- Stokes emitters in biological medium in conjunction with suitable biocompatibility enabled us to obtain a multichannel, high-contrast optical imaging of 3T3 cells using a single excitation wavelength. Notably, our material has several advantages with respect to the traditional up-converting systems, such as the low excitation intensity required, limiting damages to living tissues, and the shielding effect of nanomicelles from oxygen that protect embedded dyes from quenching and photodegradation. More importantly, the synthesis of UC-NMs is based on a simple formulation with a commercially available surfactant already employed in the formulation of several FDA-approved drugs. To our knowledge, this is the first example of efficient bi-component up-converters prepared by using biocompatible materials approved by the international authority, paving the way for the development of more complex, multicomponent, and multifunctional materials for advanced theranostics.

2

DUAL COLOR EMITTING NANOCRYSTALS FOR RATIOMETRIC PH SENSING

This work was performed in collaboration with the Italian Institute of Technology (IIT) and Los Alamos National Laboratory.
Results of this work are to be published:
F. Bruni, J. Pedrini (co-autorship), C. Bossio, B. Santiago-Gonzalez, F. Meinardi, W. K. Bae, V. I. Klimov, G. Lanzani, S. Brovelli, "Two-color emitting colloidal nanocrystals as single particle ratiometric probes of intracellular pH", *Adv. Funct. Mater.*, in press (2017).

Intracellular pH is a central parameter in the regulation of cell metabolism and in a large number of biological mechanisms, such as glycolysis and hydrolysis of adenosine triphosphate (ATP), protein folding and enzyme activity[214–217]. Moreover, alterations of intracellular pH can typically indicate cellular disfunctionalities, cancer[218–222] or major brain and heart diseases[223–226]. Therefore, sensing of intracellular pH is a fundamental diagnostic tool in biological and medical sciences. Conventionally, pH sensing is performed by using organic fluorophores as fluorescent probes. Their luminescence is quenched in acidic or basic conditions, thus allowing for the monitoring of cellular pH. The most common organic dyes for pH sensing are fluorescein and cyanine derivatives[227–229]. More recently, naphthalimide derivatives that feature multiple sites for target-specific functionalization have also found applications in pH sensing[230,231]. Other classes of materials that have recently been proposed for pH sensing[232–235] are colloidal semiconductor nanocrystals (NCs)[236,237] and metal nanoclusters with biocompatible capping ligands[238]. They combine high emission efficiency and size-tunable electronic properties with enhanced stability and exceptionally large surface-to-volume ratios. Furthermore, NCs feature broad absorption spectra that allow for non-resonant excitation. This property lowers the detection limit and increases contrast and resolution of confocal microscopy by minimizing detrimental background signals due to diffuse stray-light and auto-fluorescence of organic tissues[239–244].The bio-

compatibility of intracellular pH probes and their selectivity for specific cytoplasmic organelles can be further enhanced by using polymeric or silica nanoparticles or electrolyte nanocapsules as vehicles for their targeted internalization through the cellular membrane[245–255]. A common experimental difficulty of pH sensing based on direct photoluminescence (PL) detection (*radiometric* approach) is that it requires the accurate quantitative estimation of the emission intensity in biological systems: analyte PL is typically strongly dependent on the concentration of fluorophores inside cells. Moreover, radiometric pH sensing requires the use of fluorescent standards, such as rhodamines, to correct for experimental conditions[256]. An alternative approach that is gaining momentum in the scientific community is *ratiometric* pH sensing, that, as the name says, detects pH variations through the intensity ratio between two coexisting emissions with different pH sensitivities[257–260]. To date, ratiometric pH sensors are mostly based on metallic or semiconducting nanoparticles coupled to organic dyes, whose mutual photophysical interaction through charge- or energy-transfer is determined by the external environment, leading to pH-induced spectral variations[261–265]. Alternatively, multi-component silica nanospheres[266] or polymeric vesicles embedding ratiometric organic sensors[254] are being employed for ratiometric pH sensing experiments. Despite the diversity of proposed architectures, all ratiometric sensors available to date comprise of at least one organic component[267–269], which typically suffer from low photostability. In addition to this, a common limitation of ratiometric pH sensors is the strong cross-readout due to spectral overlap between the broad luminescence profiles of the two emitting species[256].

2.1 DOT-IN-BULK NANOCRYSTALS

In this work, we demonstrate for the first time the use of intrinsically ratiometric two-colour emitting inorganic heterostructures as single-particle intracellular pH sensors, combining many important advantages over conventional pH probes. The intrinsic ratiometric behavior eliminates the need for supramolecular constructs and for accurate control of secondary interactions. Moreover, it removes the concentration dependence of the response signal of radiometric pH probes. Furthermore, our ratiometric nanostructures have widely separated narrow-line emission bands, which completely suppresses cross-readout errors. Specifically, we used so-called dot-in-bulk CdSe/CdS NCs (DiB-NCs)[270–273] consisting of a small quantum confined CdSe core (radius ~1.5 nm) embedded in a bulk-like CdS particle (thickness ~8.5 nm). In Figure 41 we show transmission electron micrographs of CdSe/CdS

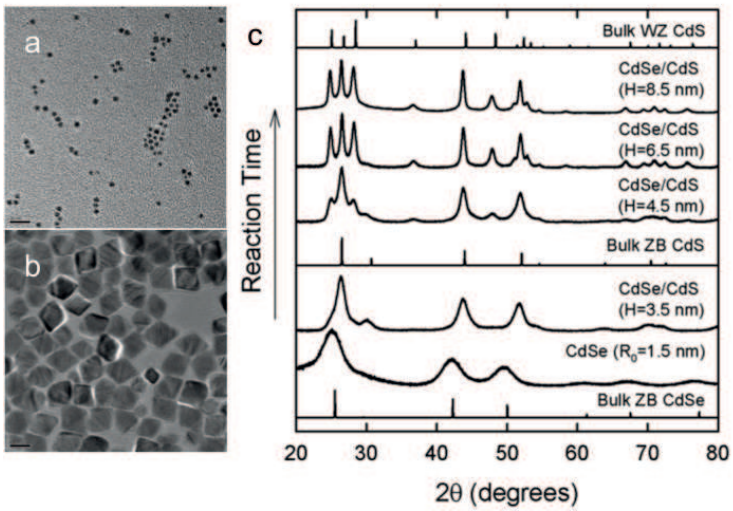

Figure 41: Structural analysis of DiB-NCs. Transmission electron microscopy images of CdSe/CdS NCs with core radius R0 = 1.5 nm and different shell thicknesses (3.5 nm (a) and 8.5 nm (b)). Scale bars in the main panels correspond to 40 nm. (c) X-ray diffraction (XRD) patterns of NCs with a core radius of 1.5 nm and different thicknesses (H = 0, 3.5, 4.5, 6.5, and 8.5 nm) in comparison to the XRD spectra of bulk CdSe and CdS.

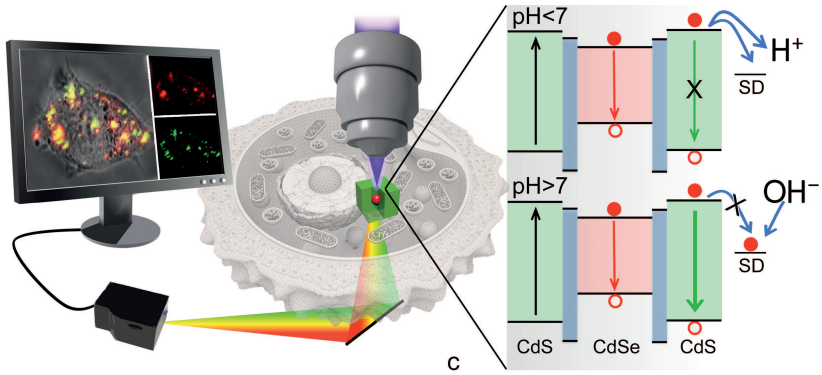

Figure 42: Schematic of intracellular ratiometric pH sensing with Dot-in-Bulk NCs, showing the simultaneous generation of two luminescence maps for the core and the shell emissions using the red and green detector channels of a confocal fluorescence microscope, respectively. The schematic representation of the band diagram of CdSe/CdS DiB-NCs and the pH sensing mechanism are shown in the right panel. At pH<7, excess H^+ cations quench the shell luminescence by directly removing electrons from the NC conduction band and by depleting (activating) electron accepting surface defects (SD). At pH>7, excess OH^- species passivate surface electron traps promoting the radiative recombination of excitons.

NCs during the synthesis at different shell thickness (3.5 nm and 8.5 nm respectively). Diffraction pattern collected at different reaction times show that the CdS shell grows in the same zincblende structure of the core for a few layers and then rearranges to the more thermodynamically stable wurtzite structure.

The two-color red and green emission, originating respectively from the core and the shell, is a direct result of a unique internal structure that features a sharp, unalloyed, core/shell interface[273] and a 30 meV potential barrier between the core and the shell valence bands[272] (Figure 42). Two-color emission in DiB NCs has been detected from core and shell excitons under low fluence optical excitation or electrical drive[270,272]. A similar well separated two-color emission behavior determined by radiative recombination of excitons localized in different compositional domains of the same heterostructure has also been observed in elongated dot-in-rod structures, tetrapods[274–277] and spherical core/shell systems[278–283].

Photoluminescence (PL) spectra of DiB-NCs are reported in Figure 43, showing the characteristic red and green emissions at 510 nm and 635 nm, respectively. The interest in DiB NCs for the application to ratiometric pH sensing arises from the different exposure of core and shell excitons to the NC surfaces. This leads to a drastically different response of their respective emission intensities to the local chemical

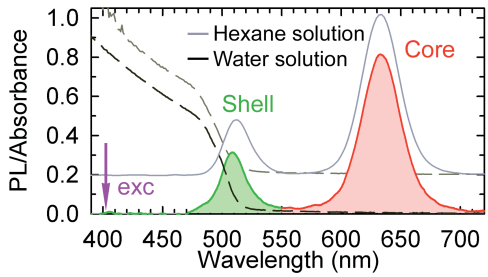

Figure 43: Optical absorption (dashed lines) and photoluminescence (solid lines) spectra (λ_{EXC}=405 nm, excitation fluence 1μJ/cm^2) of as-synthesized CdSe/CdS DiB-NCs (core radius=1.5 nm, shell thickness=8.5 nm) capped with oleic acid in hexane (grey lines) and of the same NCs in water obtained through ligand exchange with thioglycolic acid molecules (black lines, pH=7). Absorption and emission spectra of the hexane NC solution have been rigidly shifted for clarity. The core and the shell emission bands in the spectra of aqueous NCs are highlighted by red and green shading, respectively.

environment[270]: core PL is weakly affected by surface chemistry, while suppression (activation) of electron trapping under negative (positive) electrochemical potentials leads to strong enhancement (quenching) of the green shell PL, resulting in a trajectory from red-to-yellow-to-green of the total emission colour as a function of the oxidative vs. reductive nature of the NC surroundings[271]. Furthermore, in DiB NCs, quenching of the shell PL is exclusively due to extraction of photogenerated shell electrons, while holes photogenerated in the shell are unaffected by surface states and chemical agents due to their very short (~20-45 ps) residence time in the shell states. As a result, DiB NCs are sensitive mostly to electron-withdrawing agents[271], which makes them particularly suitable to optically probe the acidity of the NC surroundings and eliminates possible cross-sensitivity errors due to the competition between electron- and hole-trapping processes that characterize conventional core-only NCs. Thanks to their intrinsic ratiometric sensing ability, DiB-NCs have been recently used to probe the local charge distribution at the interface between light-sensitive organic semiconductor thin films and water[284], which constitute the functional platform of neural stimulation devices[285] for the realization of artificial retinal prosthesis for visual restoration[286]. These conditions resemble very closely the situation encountered in the pH sensing experiment schematically depicted in Figure 42: H^+ ions act as electron scavengers resulting in a drop of the shell PL, while OH^- species saturate electron poor surface states, thus enhancing the shell emission intensity. Motivated by this result, here we propose the use of DiB-NCs as intracellular ratiomet-

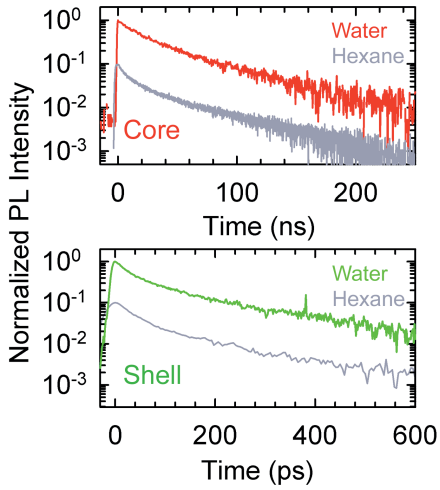

Figure 44: PL dynamics of DiB-NCs in hexane and water. Comparison between the time decay curves of the core (upper panel) and the shell (lower panel) emissions of the two NC solutions, showing essentially identical recombination dynamics in water and in hexane.

ric pH sensors whose response, in contrast to conventional ratiomeric pH probes, relies on the direct interaction between the photoexcited carriers and the local chemical surroundings.

CdSe/CdS DiB-NCs were synthesized according to the procedure reported in Section 2.2 using oleic acid as capping agent. To solubilize the NCs in water, thus making them compatible with a biological environment and for bio-imaging experiments, we performed a ligand exchange procedure with thioglycolic acid[287]. The optical properties of DiB-NCs are fully preserved upon the ligand exchange procedure, as shown in Figure 43: organic and aqueous solutions show no difference in absorption, with onset at ~520 nm due to strong absorption by the thick CdS shell, and PL profiles featuring two well-separated bands at 635 nm and 515 nm corresponding to the recombination of core and shell excitons, respectively[288]. The PL quantum efficiency of the pristine NCs ($\Phi_{PL} = 14 \pm 2\%$) is also unchanged upon ligand exchange. This is confirmed by experimental quantum yield measurements and by the essentially identical decay dynamics of both the core (average lifetime $< \tau_C > \sim 35$ ns) and shell ($< \tau_S > \sim 100$ ps) emission in the two solvents, as shown in Figure 44.

To test the photostability of pristine and ligand exchanged NCs, we monitored their PL intensity for 15 minutes under continuous illumination with UV light. Figure 45 shows stable emission from core and shell for both hexane and water solution, thus confirming DiB-NCs stability

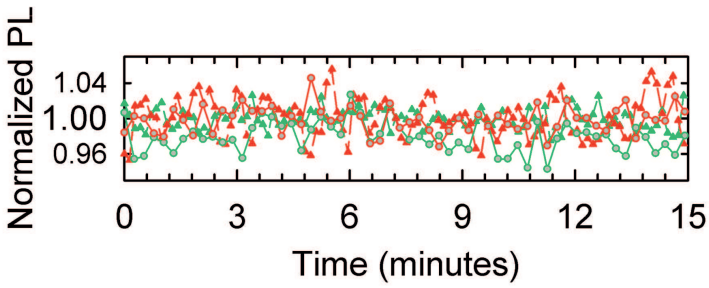

Figure 45: Time stability of DiB-NCs under illumination. Normalized integrated PL intensity of core (red curves) and shell (green curves) emission under continuous illumination (λ_{EXC}=405 nm, excitation fluence 1μJ/cm^2) for thioglycolic-capped (triangles) and oleic acid passivated CdSe/CdS DIB-NCs in water and hexane, respectively.

for illumination times significantly longer than typical bio-imaging experiments. Moreover, the two-color emission of DiB-NCs is essentially independent of temperature in the 0-70°C range, as highlighted in Figure 46 that shows a rigid red-shift of ~8 nm of both emission peaks and nearly constant I_S/I_C ratio and its first derivative $d(I_S/I_C)/dT$ across the whole temperature range. This is important for ratiometric pH sensing as it removes possible cross sensitivity effects due to variations of the sample temperature during the measurements.

2.2 METHODS

2.2.1 *Synthesis of CdSe/CdS DiB NCs*

DiB NCs NCs were synthesized following the procedure described by Brovelli and coworkers[270]. Briefly, zincblende CdSe NCs were synthesized by previously reported methods[289]. For the synthesis of CdSe (Ro = 1.5 nm)/CdS NCs, 2 × 107mol of CdSe NCs (purified twice) dispersed in 10 mL of 1-octadecene (ODE) were loaded into a 100 mL flask, degassed at 110C for 1 h. The flask was filled with Ar, and heated up to 300°C for CdS shell growth. A 0.2 mmol sample of Cd-oleate and 0.2 mmol of 1-dodecanethiol were added slowly (0.1 mmol/min) and the reaction was maintained at elevated temperature for 30 min to form a thin CdS buffer layer (~3 monolayers) on top of CdSe cores. For further CdS shell growth, a mixed solution of Cd-oleate and trioctylphospine-sulfur (0.5 M/0.5M) in ODE was continuously added at a rate of 1 mmol/hour at 300°C. After the injection of precursors was completed, reaction products were cooled to room temperature and purified repeat-

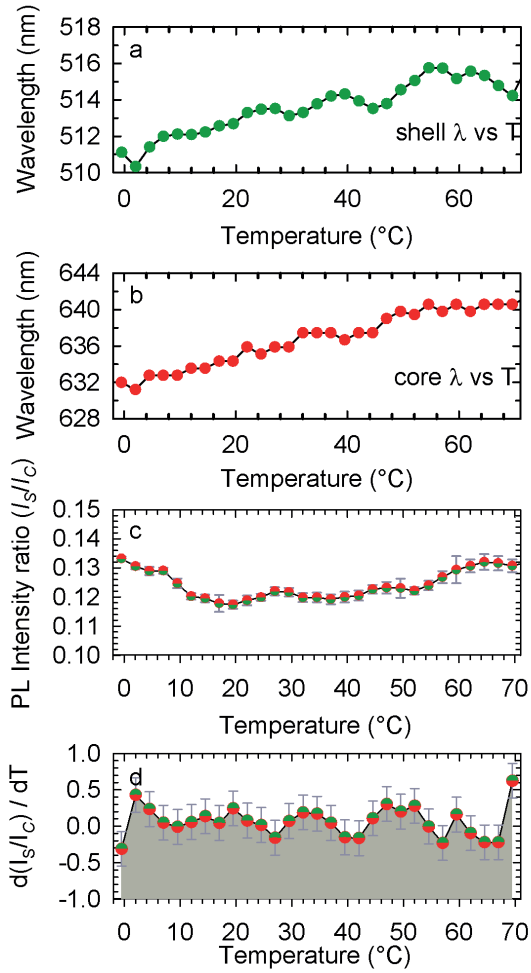

Figure 46: Temperature dependent spectral shift of shell (a) and core (b) emission at 510 nm and 640 nm, respectively. c) Temperature dependence of the ratio between core and shell integrated PL intensities (I_S/I_C, red/green cyrcles). d) First derivative of the (I_S/I_C)-vs.-T dependence. All measurements were performed using the 15 $\mu J/cm^2$ excitation fluence and the excitation wavelength of 400 nm.

edly by a precipitation-and-redispersion method. The final products were dispersed in hexane for characterization.

2.2.2 *Ligand exchange procedure*

Hydrophobic NCs were transferred from hexane to aqueous solution by adding thioglycolic acid. Excess of thioglycolic acid (twice the concentration of NCs), calculated according to Yu et al.[287] was added to the hexane solution while stirring. After two hours, a solution of tetramethylammonium hydroxide having the same concentration as the thiol was added dropwise, rendering the NCs water soluble. The water phase was then separated and precipitated by adding isopropanol followed by centrifugation. (10 min at 5000 rpm). The precipitation was repeated twice redispersing then the pellet in ultrapure water.

2.2.3 *Spectroscopic Studies*

Optical absorption and emission measurements were performed on stirred NC solutions to avoid aggregation and precipitation. Optical absorption was measured with a Varian Cary 50 spectrophotometer. Steady-state and time-resolved photoluminescence (PL) spectra were acquired exciting with a frequency-doubled Ti:Sapphire laser (emission wavelength 405 nm, pulse duration 150 fs, repetition rate 76 MHz). PL spectra were collected with a liquid-nitrogen cooled Instrument SA Spectrum One charge coupled device (CCD) coupled to a Horiba Scientific Triax 180 monochromator. PL dynamics of the shell emission in the sub-nanosecond time regime were measured with a Hamamatsu streak camera, while those of the core emission in the nanosecond time regime were studied with the same Ti:Sapphire laser as an excitation source, but reducing its repetition rate to 760 kHz with a pulse selection system based on a Conoptics 350-160 electro-optical modulator. PL dynamics were measured with a Hamamatsu R943-02 time-correlated single-photon counting unit coupled to an Oriel Instruments Cornerstone 260 monochromator. In pH sensing measurements, solution pH was modified by adding 0.1 M solutions of HNO_3 and NaOH and its value was monitored in situ using a Eutech XS pH6+ pH meter.

2.2.4 *Cell Culture*

HEK-293 cells were cultured in cell culture flasks containing Dulbecco's modified Eagle's medium (DMEM) with 10% Fetal Bovine Serum (FBS), 100 U ml^{-1} Penicillin, 100 μg ml^{-1} Streptomycin and 100 U ml^{-1} L-Glutamine. Culture flasks were maintained in a humidified incubator

at 37 °C with 5% CO_2. When at confluence, HEK-293 cells were enzymatically dispersed using trypsin-EDTA and then plated on the different polymer substrates at a concentration of 20,000 cells cm^{-2}. Cells were fixed for 20 min at RT in 4% paraformaldehyde and 4% sucrose in 0.12 M sodium phosphate buffer, pH 7.4.

2.2.5 *Cell proliferation (MTT assay)*

In order to evaluate the cell viability with DiB-NCs, the MTT [3-(4,5-dimethylthiazol-2-yl)-2,5-diphenyltetrazolium bromide] (Sigma Aldrich) assay was performed on HEK-293 cells. Cells were seeded in 12 well plates at a density of $4x10^4$ cells/well with and without the DiB-NCs. Cell proliferation was evaluated after 6 h, 24 h, 48 h and 72 h of incubation. For each time point, the growing medium was replaced with RPMI without phenol red containing 0.5 mg/mL of MTT. Samples were incubated again for 3 h at 37° C with 5% CO_2 in dark. Formazan salt produced by cells through reduction of MTT was then solubilized with 400 µL of ethanol and the absorbance was read at 560 nm and 690 nm. The proliferation cell rate was calculated as the difference in absorbed intensity at 560 nm and 690 nm. The KRH solution contained [mM]: 135 NaCl, 5.4 KCl, 5 HEPES, 10 Glucose, 1.8 $CaCl_2$, 1 $MgCl_2$. The KRH solution pH was 7.4.

2.2.6 *Confocal imaging studies*

The sample cells were imaged with a Nikon C1 confocal microscope coupled with frequency-doubled Ti:Sapphire laser (405 nm, pulse duration 150 fs, repetition rate 76 MHz), with a 60x, 1.4 NA oil immersion objective. The spot diameter for this configuration is ~ 350 nm. The green and red emission signals were collected selectively using the dedicated photomultiplier channel. The emission intensity was corrected for the respective spectral responses. For fixed cells imaging, cellular pH was changed by adding a Phosphate-Buffered Saline (PBS) solution at different pH values. After each pH change we waited 15 minutes for the system to stabilize. Living cells were observed while being kept in KRH 0.9 mM. The pH was changed by adding 100 µL of 4 mM chloroquine KRH solution, in order to obtain a 400 µM solution of chloroquine in the cellular environment. The excitation fluence was 48 µJ cm^{-2}.

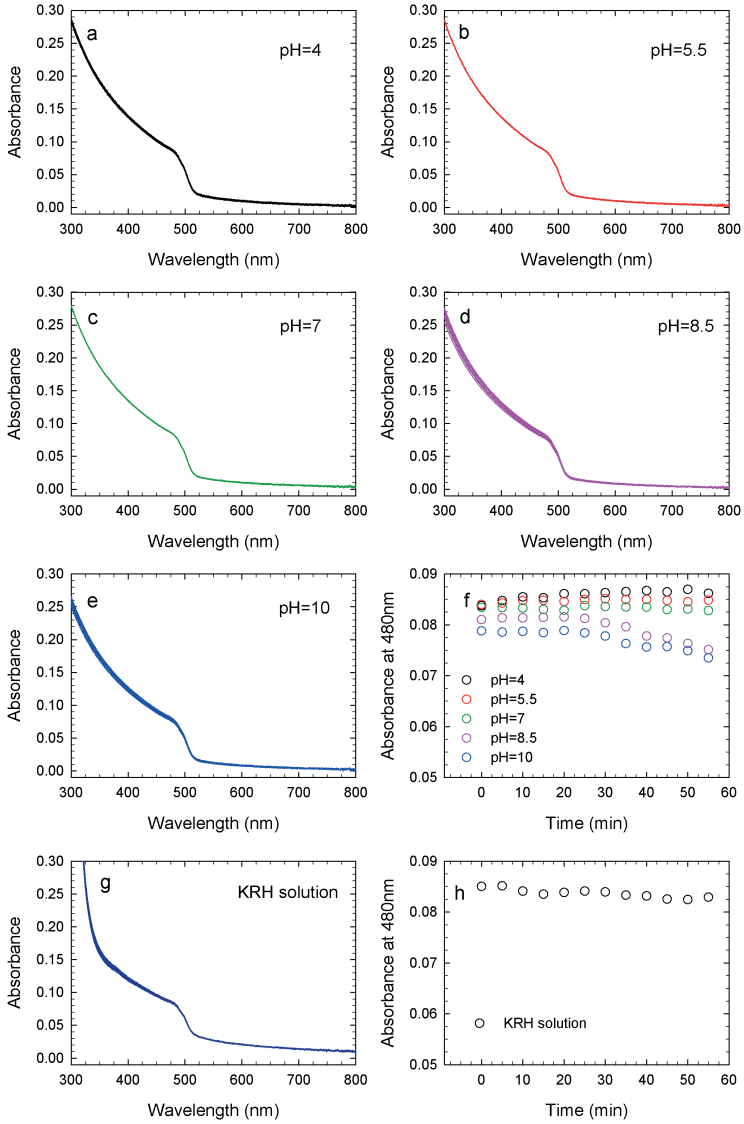

Figure 47: Collidal stability of DiB-NCs. a,e) UV-Vis absorption spectra of a solution of DiB NCs obtained at different pH values as a function of time. Each graph shows a superposition of 12 spectra acquired every 5 minutes. f) Absorbance at 480 nm as a function of time for pH 4 (black dots), 5.5 (red dots), 7 (green dots), 8.5 (pink dots) and 10 (blue dots), showing good colloidal stability in acid and basic environments. g) Superposition of 12 UV-Vis absorption spectra of a solution of DiB NCs in KRH acquired for 1h every 5 minutes. h) Absorbance at 480 nm as a function of time for DiB NCs in KRH showing good colloidal stability in a salt containing medium.

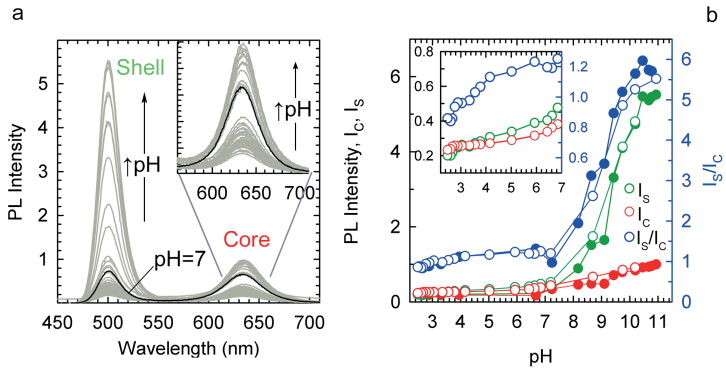

Figure 48: Demonstration of ratiometric pH sensing ability of DiB-NCs. a) Photoluminescence (PL) spectra of thioglycolic acid capped CdSe/CdS DiB-NCs in water at increasing pH (2-11) under 405 nm excitation (fluence $1\mu J/cm^2$). The spectrum corresponding to the neutral condition (pH=7) is shown as a black line for reference. The inset shows a magnification of the core emission band as a function of the pH for clarity. b. Integrated intensity of core (red circles, I_C) and shell (green circles, I_S) emissions as a function of pH in two consecutive cycles (full and empty circles) to demonstrate the reversibility of the pH sensing response. The ratio between shell and core emission intensities (I_S/I_C) is reported as blue circles. The inset highlights the acidic pH range (one cycle only for clarity), showing a 2-fold variation of the ratiometric response.

2.3 RATIOMETRIC PH SENSING IN SOLUTION

After assessing the stability of the DiB-NCs in polar environments, we proceeded with the demonstration of their ratiometric pH sensing ability. We monitored the PL of DiB-NCs in water as a function of pH, which we controlled through titration with HNO_3 and NaOH under intense stirring. Optical absorption measurements of water suspensions of thioglycolic acid capped DiB-NCs, performed as a function of time at different values of pH and of the same NCs in KRH bicarbonate buffered saline solution described in Section 2.2, demonstrate the excellent colloidal stability of the solution, showing no change in the absorption intensity and spectral profile in the investigated pH range, as reported in Figure 47.

In Figure 48a is reported a set of continuous wave PL spectra for increasing pH from 2 to 11, recorded with excitation at 405 nm. In Figure 48b, we plot the amplitudes of the shell (I_S) and the core-related (I_C) PL bands extracted from the spectra together with their ratio, I_S/I_C. The data show progressive increase of both emissions with pH, which is determined by the suppression of electron harvesting by H^+ ions upon basification of the solution (as schematized in Figure 42). This behav-

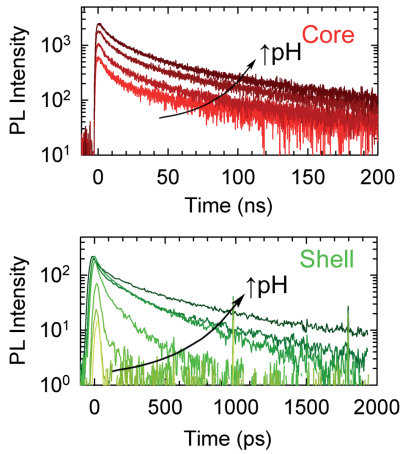

Figure 49: PL dynamics as a function of pH. Normalized time decay curves of core (red lines, λ_{PL}=635 nm) and shell (green lines, λ_{PL}=500 nm) PL at increasing pH (as indicated by the arrow).

ior is in agreement with what is reported in the literature for spectro-electrochemical observations in reductive conditions[271]. According to the direct exposure of shell excitons to NC surfaces, I_S undergoes intense, ~30-fold, enhancement with increasing pH, which is almost 10 times stronger than the growth experienced by I_C in the same pH range (~4-fold increase). As a result of this strong difference in pH sensitivity, I_S/I_C spans from 1 to 6 as a function of pH with the most intense effect in the basic region (Figure 48b), leading to a progressive change of the total emission color from red to green. In order to gather deeper insight into the ratiometric sensing mechanism of DiB-NCs, we measured the time dynamics of both core and shell PL as a function of pH. We notice that the decay profile of the core emission, reported in Figure 49, is essentially unaffected by the NC environment, while the zero-delay emission intensity grows with increasing pH. This indicates that the electron capture process responsible for PL quenching in acidic conditions is much faster than the ~ 1 ns resolution of the time-correlated single photon counter used for measuring the core PL dynamics. Since core excitons are localized away from the NC surfaces, extraction of core electrons only occurs in a minor fraction of the NCs ensemble. In the majority of NCs core excitons are almost unaffected by external conditions, leading to a mild sensitivity of core PL to local pH. Conversely, shell PL dynamics show a strong effect of the pH on both zero-delay PL intensity and shell exciton lifetime. This observation points to the coexistence of a distribution of electron capture processes occurring on

different time regimes and affecting different subpopulations of NCs in the ensemble. The growth of the zero-delay signal confirms the ultrafast nature of the electron capture process observed for core PL. This depletes the shell conduction band from photo-excited electrons in a large moiety of NCs before their radiative decay or localization into core states[271]. Shell PL lifetime simultaneously increases upon basification, due to progressive suppression of slower electron trapping processes, most likely associated to the distribution of NC-H^+ distances in water solution and with the variety of surface sites mediating the electron capture mechanism[271].

2.4 RATIOMETRIC PH SENSING IN FIXATED CELLS

To experimentally validate the ratiometric sensing ability of DiB-NCs *in vitro*, we internalized them into Human Embryonic Kidney (HEK-293) cells and monitored I_S/I_C as a function of intracellular pH using confocal fluorescence microscopy. For fixated cells, pH was changed by titrating the phosphate-buffered saline (PBS) solution with NaOH or HNO_3 solutions (0.1 M). Each image of the same cell was recorded under identical excitation and collection conditions after 15 minutes from the addition of the titrating solution to ensure the achievement of stable intracellular pH. In Figure 50 we report fluorescence images of two HEK-293 cells stained with DiB-NCs overlaid to their respective bright field images (Figure 50a-e). DiB-NCs are not functionalized with target-specific ligands, therefore they disperse inside the cell forming small domains of aggregated NCs, enabling the visualization of local intracellular environment even at very low concentrations. Better dispersion of the NCs inside the cell, or targeting to specific subcellular organelles is in principle achievable by suitable capping with site selective functionalities. However, specific targeting and functionalization is beyond the scope of this proof-of-principle study and was not dealt with in this work. The ratiometric pH response of the DiB-NCs is emphasized in Figure 50a1-e1 and 50a2-e2, by reporting fluorescence images collected using the red and green detector channels of the confocal microscope to selectively monitor the evolution of core and shell PL, respectively. These images show the progressive emergence of green shell luminescence for increasing pH (pH= 4-10), in agreement with the sensing behavior observed in ensemble measurements. The quantitative estimation of the ratiometric sensing response obtained by extracting the intensity of the two detection channels for 40 emitting spots as a function of pH is reported in Figure 50f. In Figure 50g, we report the average ratiometric response $<I_S/I_C>$ corresponding to the average pH response per detection spot. A similar trend to the ensemble response

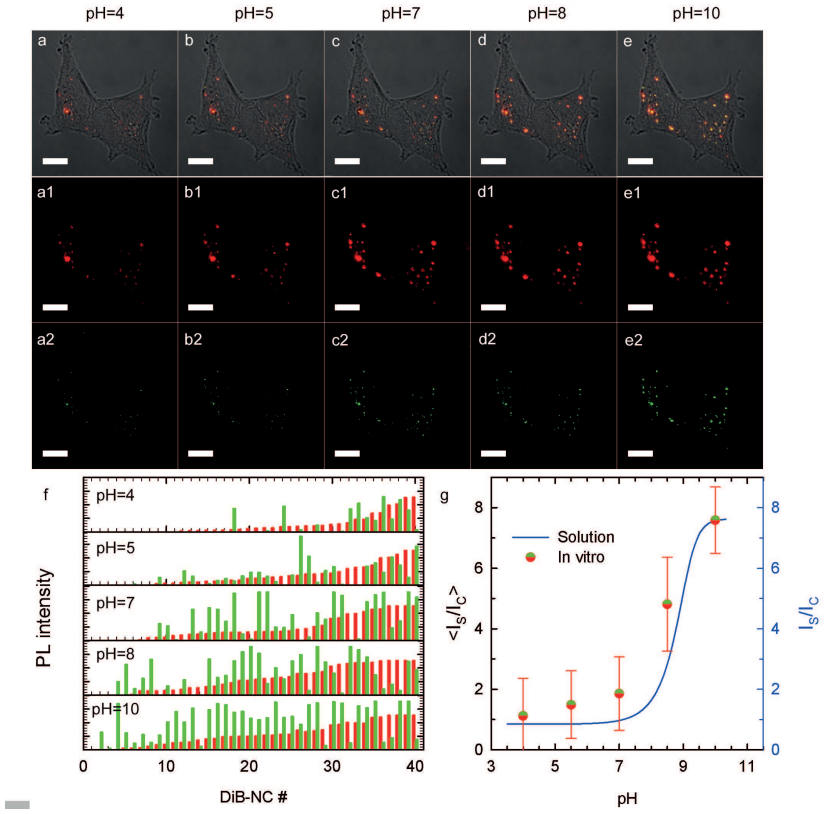

Figure 50: Intracellular pH sensing on fixed HEK-293 cells. Confocal images of HEK-293 cells stained with 130 nM DiB-NCs at increasing pH collected under 405 nm excitation (fluence 18 $\mu J/cm^2$). a-e) Overlay of confocal images and bright-field images collected with a 60x, 1.4 NA, oil immersion objective. Evolution of core (a1-e1) and shell (a2-e2) emissions with increasing pH. The scale bar is 10μm for all panels. f) Histograms of shell (green bars) and core (red bars) PL intensity of the DiB-NCs collected selectively with the green and the red detector channels at increasing pH. g) Average shell-to-core PL intensity ratio ($< I_S/I_C >$) as a function of pH in fixed HEK-293 cells extracted from the histograms in 'f' (circles). The ensemble I_S/I_C measured in aqueous solution is reported as a blue line.

reported in Figure 48b can be noticed. The differences between the absolute values of the ratiometric response in confocal and far-field measurements are most likely due to different experimental setups and to local inhomogeneities of intracellular pH.

2.5 RATIOMETRIC PH SENSING IN LIVING CELLS

Fixation preserves tissues from degradation, but it terminates every biochemical process inside the cell, resulting in a different chemical environment with respect to that found in a living sample[290–294]. Studies on fixated cells are often employed just as a calibration of a proof-of-principle system, while the real pH-sensing experiment needs to be done on living cells. Therefore we internalized DiB-NCs into living HEK-293 cells in Krebs-Ringer Bicarbonate (KRH) buffer solution. The time lapse imaging of NC internalization is shown in Figure 51, together with the I_S/I_C ratio, showing progressive dimming of the shell PL for a NC approaching and interacting with the cell membrane, according to the expected acidity of the cell membrane with respect to the culture medium. Unfortunately, we were not able to observe complete internalization of a single DiB-NC because of setup constraints. Our confocal microscope is not equipped with an incubator. Therefore, cells are not kept at 37°C with 5% CO_2 during the measurement and they die just after some hours. With a different setup it should be possible to successfully detect DiB-NC internalization into a living cell. Prior to pH monitoring experiments, we evaluated the cytotoxicity of DiB-NCs by performing the MTT [3-(4,5-dimethylthiazol-2-yl)-2,5-diphenyltetrazolium bromide] assay on HEK-293 cells after 6h, 24h, 48h and 72h of incubation with and without the NCs. MTT is reduced to formazan in living cells. Since this reduction depends on cellular metabolic activity, stronger formazan optical absorption indicates progressively larger cell population[295,296]. Figure 52 shows the results of the MTT assay on cells stained with increasing concentrations of DiB-NCs, showing that cell proliferation is unaffected by NCs, even at high concentration, which indicates good biocompatibility of DiB-NCs.

We induced changes in intracellular pH by exposing the living cells to chloroquine, a weakly basic amine that accumulates into the lysosomes and into the Golgi apparatus. This accumulation results in a slight basification of the intracellular environment[297]. In Figure 53, we show confocal images of a single living HEK cell stained with DiB-NCs before and 30 minutes after exposure to a 400µM chloroquine solution[298], overlaid to the corresponding bright field pictures. Confocal images reveal a significant brightening of the green shell PL upon addition of chloroquine, in agreement with its expected cytoplasm basi-

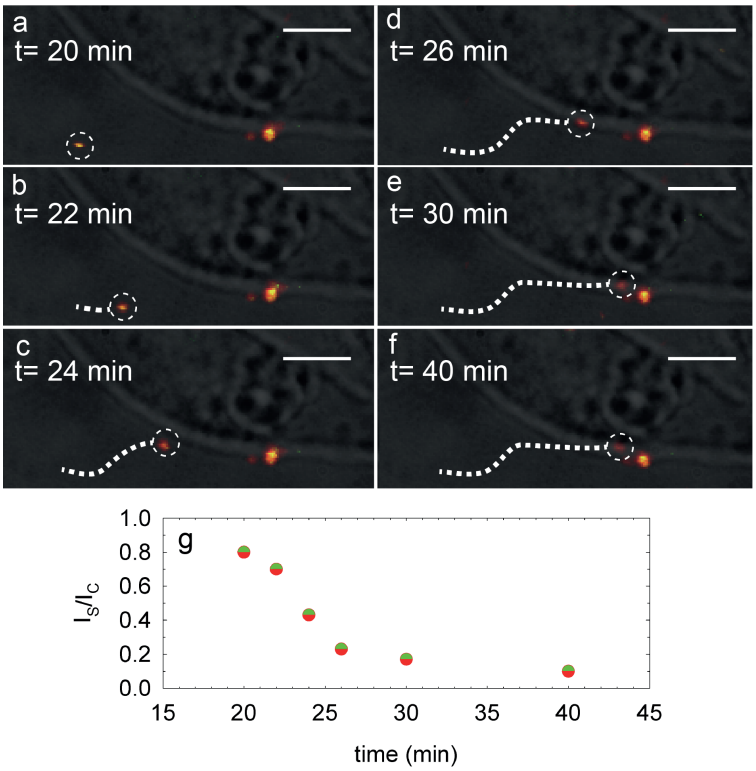

Figure 51: Trajectory of a DiB NC during internalization in living HEK-293 cells in KRH. a,f) Overlay of confocal images collected with the red and green detector channels and bright-field images of living HEK cells stained with 130 nM DiB-NCs at increasing internalization time. The temporal resolution of the images is 60 s. The scale bar is 10 μm for every image. One of the DiB NCs moves and its path and PL intensity can be tracked. The DiB NCs approaches the cell (a, b, c) and touches the membrane (d), stopping there for a long period of time (e, f). g) The ratio of the shell and the core PL intensities (I_S/I_C) suggests acidification in the surrounding of the cell.

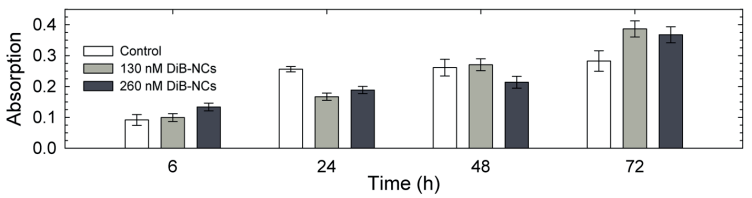

Figure 52: Cell proliferation experiments and intracellular ratiometric pH sensing in living HEK-293 cell. MTT assay for cell viability up to 3 days in vitro for two different DiB-NCs concentrations (130 nM and 260 nM) and for untreated control cells (ctrl). Data are reported as average n = 12 ± SE.

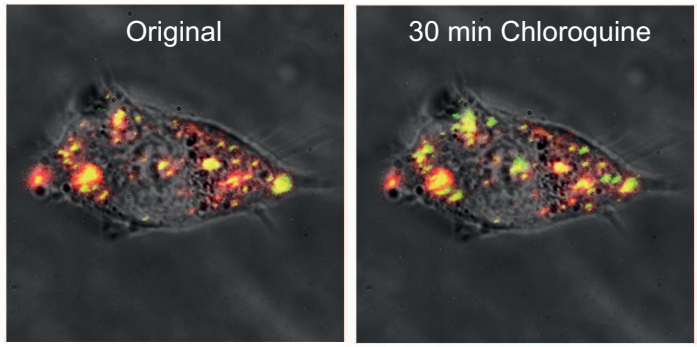

Figure 53: Intracellular ratiometric pH sensing in living HEK-293 cell. Overlay of confocal images collected with the red and green detector channels and bright-field images of living HEK cells stained with 130 nM DiB-NCs at increasing pH. The intracellular pH was modified by adding a 400 μM solution of chloroquine. The measurements were performed 30 min after adding the chloroquine solution.

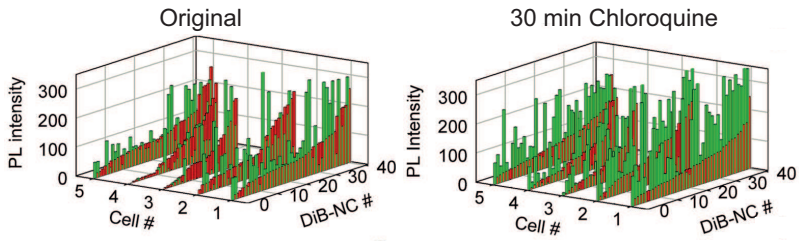

Figure 54: Histograms of green and red photoluminescence intensities for a statistically relevant ensemble of 40 NCs repeated for 5 different cell cultures.

fication effect. To quantify the variation of core and shell PL intensities and confirm the reproducibility of the pH sensing assay, in Figure 54 we report histograms for 40 representative emitting spots for five different cells, showing progressive enhancement of shell emission with exposure time, while core PL remains essentially unaltered by the addition of chloroquine. As a result, the $<I_S/I_C>$ ratio increases by a factor ~2 after a 30-minutes exposure (Figure 55), thus confirming the suitability of our NCs as pH-sensitive optical probes for in-vitro applications.

2.6 CONCLUSIONS

In this work we demonstrated that heterostructured NCs can be used as intrinsic ratiometric probes for intracellular pH sensing. With this aim, we specifically chose CdSe/CdS DiB-NCs that show a characteristic two-color emission arising from simultaneous radiative recombi-

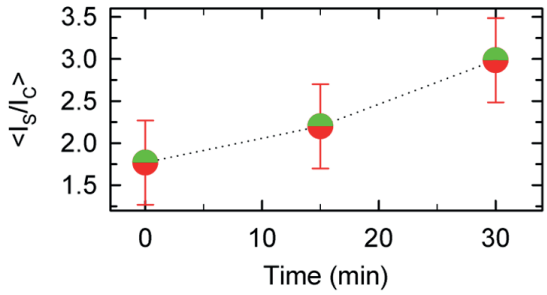

Figure 55: Average shell-to-core emission ratio as a function of exposure time to chloroquine extracted from the histograms reported in Figure 54

nation of core and shell excitons. Those are differently affected by the NC surfaces and chemical agents and can therefore be exploited to ratiometrically probe the local NC environment. This has been demonstrated through far-field spectroscopic measurements upon titration with HNO_3 and NaOH, leading to ~600% enhancement of the shell-to-core PL ratio and through confocal measurements on fixed and living HEK-293 cells in controlled pH conditions. Cell viability studies reveal good bio-compatibility of DiB-NCs, validating their potential as intracellular pH sensors. We want to point out that the reported proof-of-principle CdSe/CdS NCs are not optimized in terms of CdS shell thickness or capping ligand. Further improvements in photoluminescence quantum efficiency and pH sensitivity might be expected by optimizing surface coverage and functionalization. The strategy demonstrated here for CdSe/CdS heterostructured NCs is not dependent on composition and might, in principle, be extended to other semiconductors. In particular, heavy-metal free semiconductors such as ternary I-III-VI_2 NCs[299], as well as heterostructures with different band alignment (type I, inverted type I etc...) may be considered.

LIST OF PUBLICATIONS

1. M. Lorenzon, S. Christodoulou, G. Vaccaro, J. Pedrini, F. Meinardi, I. Moreels, S. Brovelli, "Reversed oxygen sensing using colloidal quantum wells towards highly emissive photoresponsive varnishes", *Nature Communications*, 6:6434 (2015)

2. A. Monguzzi, S. M. Borisov, **J. Pedrini**, I. Klimant, M. Salvalaggio, P. Biagini, F. Melchiorre, C. Lelii, F. Meinardi, "Efficient Broadband Triplet–Triplet Annihilation-Assisted Photon Upconversion at Subsolar Irradiance in Fully Organic Systems", *Advanced Functional Materials*, 26, 35, 5617-5624 (2015)

3. B. Santiago-Gonzalez, A. Monguzzi, J. M. Azpiroz, M. Prato, S. Erratico, M. Campione, R. Lorenzi, **J. Pedrini**, C. Santambrogio, Y. Torrente, F. De Angelis, F. Meinardi, S. Brovelli, "Permanent excimer superstructures by supramolecular networking of metal quantum clusters", *Science*, 353, 6299, 571-575 (2016)

4. A. Monguzzi, M. Mauri, M. Frigoli, **J. Pedrini**, R. Simonutti, C. Larpent, G. Vaccaro, M. Sassi, F. Meinardi, "Unraveling Triplet Excitons Photophysics in Hyper-Cross-Linked Polymeric Nanoparticles: Toward the Next Generation of Solid-State Upconverting Materials", *The Journal of Physical Chemistry Letters*, 7, 14, 2779-2785 (2016)

5. S. Mattiello, A. Monguzzi, **J. Pedrini**, M. Sassi, C. Villa, Y. Torrente, R. Marotta, F. Meinardi, L. Beverina, "Self-Assembled Dual Dye-Doped Nanosized Micelles for High-Contrast Up-Conversion Bioimaging". *Advanced Functional Materials*, 26, 46, 8447-8454 (2016)

6. F. Bruni, **J. Pedrini** (co-autorship), C. Bossio, B. Santiago-Gonzalez, F. Meinardi, W. K. Bae, V. I. Klimov, G. Lanzani, S. Brovelli, "Two-color emitting colloidal nanocrystals as single particle ratiometric probes of intracellular pH", *Advanced Functional Materials*, in press (2017)

7. **J. Pedrini**, A. Monguzzi, M. Salvalaggio, F. Meinardi, "Supersensitized Triplet-triplet Annihilation based Photon Up-conversion at Subsolar Irradiance in Organic Systems", *in preparation*

8. **J. Pedrini**, C. T. Chen, G. Calafiore, T. Kuykendall, S. Cabrini, S. Aloni, and A. M. Schwartzberg, "Simple fabrication of photonic structures via atomic layer deposition of WS_2 films", *in preparation*

BIBLIOGRAPHY

[1] J. D. Joannopoulos et al. 2008.

[2] N. Bloembergen. 1965.

[3] A. R. Parker, *J. Opt. A: Pure Appl. Opt.* 2.6 (2000), R15–R28.

[4] V. Pete, S. J. Roy, and L. C. R., *Nature* 404 (2000), p. 457.

[5] S. R. A. and P. H. K., *Electron Microsc.* 2 (1980), 754–755.

[6] N. A. C. and C. S., *Biol. Rev.* 44 (1969), 531–62.

[7] L. M. Mäthger et al., *J. Exp. Biol.* 215.21 (2012), pp. 3752–3757.

[8] J. Zi et al., *Proc. Natl. Acad. Sci.* 100.22 (2003), pp. 12576–12578.

[9] P. Vukusic and J. R. Sambles, *Nature* 424 (2003), pp. 852–855.

[10] J. V. Sanders, *Nature* 204 (1964), pp. 1151–1153.

[11] J. V. Sanders, *Acta Crystallogr. Sect. A* 24.4 (1968), pp. 427–434.

[12] L. R. Sec.R.S., *Philos. Mag. Series 5* 26.160 (1888), pp. 256–265.

[13] E. Yablonovitch, *Phys. Rev. Lett.* 58.20 (1987), pp. 2059–2062.

[14] J. Sajeev, *Phys. Rev. Lett.* 58.23 (1987), pp. 2486–2489.

[15] E. Yablonovitch, T. J. Gmitter, and K. M. Leung, *Phys. Rev. Lett.* 67 (17 1991), pp. 2295–2298.

[16] T. F. Krauss, R. M. De La Rue, and S. Brand, *Nature* 383 (1996), pp. 699–702.

[17] R. C. Schroden et al., *Chem. Mater.* 14.8 (2002), pp. 3305–3315.

[18] G. I. N. Waterhouse et al., *Chem. Mater.* 20 (2008), pp. 1183–1190.

[19] J. S. King et al., *Appl. Surf. Sci.* 244 (2005), pp. 511–516.

[20] D. Gaillot, T. Yamashita, and C. J. Summers, *Phys. Rev. B* 72.20 (2005), pp. 1–10.

[21] S. Noda et al., *Science* 289.5479 (2000), pp. 604–606.

[22] S. Ogawa et al., *Science* 305.5681 (2004), pp. 227–229.

[23] M. Campbell et al., *Nature* 404.6773 (2000), pp. 53–56.

[24] X. Wang et al., *Appl. Phys. Lett.* 82.14 (2003), pp. 2212–2214.

[25] C. K. Ullal et al., *Appl. Phys. Lett.* 84.26 (2004), pp. 5434–5436.

[26] S. Noda et al., *Science* 289.5479 (2000), pp. 604–606.

[27] L. Chen and A. V. Nurmikko, *Appl. Phys. Lett.* 85.17 (2004), pp. 3663–3665.

[28] E. Matioli and C. Weisbuch, *J. Phys. D* 43.35 (2010), p. 354005.

[29] S. Fan et al., *Phys. Rev. Lett.* 78.17 (1997), p. 3294.

[30] M. Meier et al., *Appl. Phys. Lett.* 74.1 (1999), pp. 7–9.

[31] M. Imada et al., *Phys. Rev. B* 65 (19 2002), p. 195306.

[32] F. Scotognella et al., *Phys. Chem. Chem. Phys.* 12 (2 2010), pp. 337–340.

[33] D. P. Puzzo et al., *Nano Lett.* 9.12 (2009), pp. 4273–4278.

[34] O. Painter et al., *Science* 284.5421 (1999), pp. 1819–1821.

[35] M. Lončar et al., *Appl. Phys. Lett.* 81.15 (2002), p. 2680.

[36] R. Colombelli et al., *Science* 302.November (2003), pp. 1374–1377.

[37] H.-G. Park et al., *Science* 305.5689 (2004), pp. 1444–1447.

[38] L. M. Duan and H. J. Kimble, *Phys. Rev. Lett.* 92.12 (2004), pp. 127902–1.

[39] Y. Akahane et al., *Nature* 425.October (2003), p. 944.

[40] M. Notomi, *Rep. Prog. Phys.* 73.9 (2010), p. 096501.

[41] E. Dulkeith, S. J. McNab, and Y. A. Vlasov, *Phys. Rev. B* 72.11 (2005), pp. 1–9.

[42] G. Calafiore et al., *Nanotechnology* 27.11 (2016), p. 115303.

[43] L. Feng et al., *Science* 333.6043 (2011), pp. 729–733.

[44] C. J. Barrelet, A. B. Greytak, and C. M. Lieber, *Nano Lett.* 4.10 (2004), pp. 1981–1985.

[45] C. Pina-Hernandez et al., *Nanotechnology* 25.32 (2014), p. 325302.

[46] G. Calafiore et al., *Light Sci. Appl.* 3.9 (2014), e203.

[47] T. Zijlstra et al., *J. Vac. Sci. Technol. B* 17.6 (1999), pp. 2734–2739.

[48] M. Tokushima et al., *Appl. Phys. Lett.* 76.8 (2000), pp. 952–954.

[49] S. F. Mingaleev et al., *Opt. Lett.* 29.24 (2004), pp. 2858–2860.

[50] I. Guryev et al., *Appl. Phys. B* 84.1 (2006), pp. 83–87.

[51] E. Waks and J. Vuckovic, *Phys. Rev. A* 73 (4 2006), p. 041803.

[52] J. Zhou et al., *Opt. Lett.* 30.12 (2005), pp. 1560–1562.

[53] A. Shinya et al., *Opt. Express* 16.23 (2008), pp. 19382–19387.

[54] P. Andalib and N. Granpayeh, *J. Opt. Soc. Am. B* 26.1 (2009), pp. 10–16.

[55] T. Tanabe et al., *Appl. Phys. Lett.* 87.15 (2005), pp. 1–3.

[56] K. Nozaki et al., *Nat. Photonics* 4.7 (2010), pp. 477–483.

[57] H. Xiao and D. Yao, *Phys. Lett. A* 359 (6 2006), 723—727.

[58] J. L. O'Brien, *Science* 318.5856 (2007), pp. 1567–1570.

[59] J. L. O'Brien, A. Furusawa, and J. Vučković, *Nat. Photonics* 3.12 (2009), pp. 687–695.

[60] R. H. Hadfield, *Nat. Photonics* 3.12 (2009), p. 696.

[61] P. Russell, *Science* 299.5605 (2003), p. 358.

[62] L. Zeng et al., *Appl. Phys. Lett.* 89.11 (2006), pp. 3–6.

[63] J. R. Piper and S. Fan, *ACS Photonics* (2016).

[64] H. K. Raut et al., *Energy Environ. Sci.* 4.10 (2011), p. 3779.

[65] S. Y. Choi et al., *Nano Lett.* 6.11 (2006), pp. 2456–2461.

[66] J. W. Galusha, M. R. Jorgensen, and M. H. Bartl, *Adv. Mater.* 22.1 (2010), pp. 107–110.

[67] Z. Z. Gu et al., *Angew. Chem. Int. Ed.* 42.8 (2003), pp. 894–897.

[68] O. Sato, S. Kubo, and Z.-Z. Gu, *Acc. Chem. Res.* 41.1 (2009), pp. 1–10.

[69] Z. Wu et al., *Small* 3.8 (2007), pp. 1445–1454.

[70] N. Yu et al., *Science* 334 (2011), pp. 333–337.

[71] E. De Tommasi et al., *Appl. Phys. Lett.* 102.8 (2013), pp. 1–6.

[72] J. Valentine et al., *Nature* 455.7211 (2008), pp. 376–379.

[73] J. Valentine et al., *Nat. Mater.* 8.7 (2009), pp. 568–571.

[74] V. Mocella et al., *Phys. Rev. Lett.* 102.13 (2009), pp. 1–5.

[75] P. Dardano et al., *Light Sci. Appl.* 1.12 (2012), e42.

[76] N. Yu and F. Capasso, *Nat. Mater.* 13.2 (2014), pp. 139–50.

[77] E. Chow et al., *Opt. Lett.* 29.10 (2004), pp. 1093–1095.

[78] K. Lee and S. A. Asher, *J. Am. Chem. Soc.* 122.39 (2000), pp. 9534–9537.

[79] P. Ganter, K. Szendrei, and B. V. Lotsch, *Adv. Mater.* (2016).

[80] H. M. et al., *Nat. Photon.* 7 (2013), pp. 1001–1005.

[81] A. Rickman, *Nat. Photon.* 8 (2014), pp. 579–582.

[82] A. Blanco-Redondo et al., *Nat. Commun.* 5 (2014), p. 3160.

[83] S. A. Rinne, F. Garcia-Santamaria, and P. V. Braun, *Nat. Photon.* 2 (2008), pp. 52–56.

[84] M. A. Green and M. J. Keevers, *Prog. Photovoltaics* 3.3 (1995), pp. 198–192.

[85] D. P. Gaillot et al., *Appl. Phys. Lett.* 91.18 (2007), pp. 89–92.

[86] Y. Zhu et al., *Appl. Phys. A* 94.4 (2009), pp. 731–734.

[87] M. R. Jorgensen, J. W. Galusha, and M. H. Bartl, *Phys. Rev. Lett.* 107.14 (2011), pp. 1–5.

[88] Z. A. Sechrist et al., *Chem. Mater.* 18.15 (2006), pp. 3562–3570.

[89] M. Scharrer et al., *Appl. Phys. Lett.* 86.15 (2005), pp. 1–3.

[90] H. Miguez et al., *Appl. Phys. Lett.* 71.9 (1997), pp. 1148–1150.

[91] H. Miguez et al., *Adv. Mater.* 10.6 (1998), pp. 480–483.

[92] S. G. Johnson et al., *Phys. Rev. B* 60.8 (1999), pp. 5751–5758.

[93] Y. Li et al., *Phys. Rev. B* 90.20 (2014), p. 205422.

[94] D. G. Figueroa del Valle, E. Aluicio-Sarduy, and F. Scotognella, *Opt. Mater.* 48 (2015), pp. 267–270.

[95] X. Duan et al., *Chem. Soc. Rev.* 44 (2015), pp. 8859–8876.

[96] L. Tao et al., *Nat. Nanotechnol.* 10.3 (2015), pp. 227–231.

[97] L. Song et al., *Nano Lett.* 10.8 (2010), pp. 3209–3215.

[98] L. Li et al., *Nat. Nanotechnol.* 9.5 (2014), pp. 372–377.

[99] K. I. Bolotin et al., *Solid State Commun.* 146.9 (2008), pp. 351–355.

[100] C. R. Dean et al., *Nat. Nanotechnol.* 5.10 (2010), pp. 722–726.

[101] M. Nath et al., *Chem. Phys. Lett.* 368.5 (2003), pp. 690–695.

[102] F. H. L. Koppens et al., *Nat. Nanotechnol.* 9.10 (2014), pp. 780–793.

[103] Y. Chen et al., *Science* 325.5937 (2009), pp. 178–181.

[104] A. Splendiani et al., *Nano Lett.* 10.4 (2010), pp. 1271–1275.

[105] G. Eda et al., *Nano Lett.* 11.12 (2011), pp. 5111–5116.

[106] H. R. Gutiérrez et al., *Nano Lett.* 13.8 (2013), pp. 3447–3454.

[107] B. Radisavljevic et al., *Nat. Nanotechnol.* 6.3 (2011), pp. 147–50.

[108] J. Wilson and A. Yoffe, *Adv. Phys.* 18.73 (1969), pp. 193–335.

[109] Y. Kim, J. Huang, and C. M. Lieber, *Appl. Phys. Lett.* 59.26 (1991), pp. 3404–3406.

[110] K. S. Novoselov et al., *Science* 306.5696 (2004), pp. 666–669.

[111] Q. H. Wang et al., *Nat. Nanotechnol.* 7.11 (2012), pp. 699–712.

[112] F. Wang et al., *Nanoscale* 7 (2015), pp. 19764–19788.

[113] Q. H. Wang et al., *Nat. Nanotechnol.* 7.11 (2012), pp. 699–712.

[114] M. Shanmugam et al., *Appl. Phys. Lett.* 100.15 (2012), p. 153901.

[115] A. Fujishima and K. Honda, *Nature* 238.5358 (1972), pp. 37–38.

[116] A. K. Geim and I. V. Grigorieva, *Nature* 499.7459 (2013), pp. 419–425.

[117] M. Bosi, *RSC Adv.* 5.92 (2015), pp. 75500–75518.

[118] A. Pospischil, M. M. Furchi, and T. Mueller, *Nat. Nanotechnol.* 9.4 (2014), pp. 257–261.

[119] R. Cheng et al., *Nano Lett.* 14.10 (2014), pp. 5590–5597.

[120] C.-H. Lee et al., *Nat. Nanotechnol.* 9.9 (2014), pp. 676–681.

[121] M. Massicotte et al., *Nat. Nanotechnol.* 11.January (2016), pp. 42–47.

[122] H. L. Liu et al., *Appl. Phys. Lett.* 105.20 (2014).

[123] D. Bouhafs et al., *Sol. Energ. Mat. Sol. C* 52.1–2 (1998), pp. 79 –93.

[124] T. Nakamura et al., *Opt. Rev.* 13.2 (2006), pp. 104–110.

[125] M. Ma et al., *J. Appl. Phys.* 108.4 (2010), p. 043102.

[126] G.-H. Lee et al., *ACS Nano* 9.7 (2015), pp. 7019–7026.

[127] C. Kim et al., *Adv. Funct. Mater.* 25 (2015), pp. 4512–4519.

[128] Y. Shi, H. Li, and L.-J. Li, *Chem. Soc. Rev.* 44.9 (2015), pp. 2744–2756.

[129] S. M. Eichfeld et al., *ACS Nano* 9.2 (2015), pp. 2080–2087.

[130] Y.-H. Lee et al., *Adv. Mater.* 24.17 (2012), pp. 2320–2325.

[131] R. Browning et al., *Mater. Res. Express* 2.3 (2015), p. 035006.

[132] Y. Zhan et al., *Small* 8.7 (2012), pp. 966–971.

[133] J. Kibsgaard et al., *Nat. Mater.* 11.11 (2012), pp. 963–969.

[134] J.-G. Song et al., *ACS Nano* 7.12 (2013), pp. 11333–11340.

[135] J. S. King, E. Graugnard, and C. J. Summers, *Appl. Phys. Lett.* 88.8 (2006), p. 081109.

[136] E. Graugnard et al., *Appl. Phys. Lett.* 89.18 (2006), pp. 10–13.

[137] S. M. George, *Chem. Rev.* 110.1 (2010), pp. 111–131.

[138] A. M. Schwartzberg and D. Olynick, *Adv. Mater.* 27 (2015), pp. 5778–5784.

[139] Z. Jin et al., *Nanoscale* 6.23 (2014), pp. 14453–14458.

[140] L. K. Tan et al., *Nanoscale* 6 (18 2014), pp. 10584–10588.

[141] J. S. Becker and R. G. Gordon, *Appl. Phys. Lett.* 82.14 (2003), pp. 2239–2241.

[142] H. Fujiwara. John Wiley & Sons, 2007.

[143] M. D. Groner et al., *Chem. Mater.* 16.4 (2004), pp. 639–645.

[144] T Millner and J. Neugebauer, *Nature* 163 (1949), pp. 601–602.

[145] A. Berkdemir et al., *Sci. Rep.* 3 (2013), p. 1755.

[146] N. An et al., *MRS Comm.* 6.2 (2016), pp. 1–7.

[147] A. R. Beal, H. P. Hughes, and W. Y. Liang, *J. Phys. C* 8.24 (1975), p. 4236.

[148] C. Yim et al., *Appl. Phys. Lett.* 104.10 (2014), p. 103114.

[149] C. C. Shen et al., *Appl. Phys. Express* 6 (2013), p. 125801.

[150] A. Matthias et al., *Thin Solid Films* 558 (2014), pp. 86 –92.

[151] E. Chow et al., *Nature* 407.6807 (2000), pp. 983–6.

[152] S. Fan and J. D. Joannopoulos, *Phys. Rev. B* 65.23 (2002), p. 235112.

[153] M. Kanskar et al., *Appl. Phys. Lett.* 70.11 (1997), pp. 1438–1440.

[154] A. R. Cowan et al., *J. Opt. Soc. Am. A* 18.5 (2001), pp. 1160–70.

[155] S. G. Tikhodeev et al., *Phys. Rev. B* 66.4 (2002), p. 045102.

[156] J. W. Lichtman and J.-A. Conchello, *Nat. Methods* 2.12 (2005), pp. 910–919.

[157] K. D. Wegner and N. Hildebrandt, *Chem. Soc. Rev.* 44.14 (2015), pp. 4792–4834.

[158] B. Zhou et al., *Nat. Nanotechnol.* 10.11 (2015), pp. 924–936.

[159] J. A. Barreto et al., *Adv. Mater.* 23.12 (2011).

[160] I. Villa et al., *Nano Res.* 8.2 (2015), pp. 649–665.

[161] J. C. Goldschmidt and S. Fischer, *Adv. Opt. Mat.* 3.4 (2015), pp. 510–535.

[162] F. Wang et al., *Nat. Mater.* 10.12 (2011), pp. 968–973.

[163] J. Zhou et al., *Chem. Rev.* 115.1 (2014), pp. 395–465.

[164] W. Feng, X. Zhu, and F. Li, *NPG Asia Mater.* 5.12 (2013), e75.

[165] L. Zhou et al., *Nat. Commun.* 6 (2015).

[166] C. Ye et al., *Phys. Chem. Chem. Phys.* 18.16 (2016), pp. 10818–10835.

[167] A. Monguzzi et al., *Adv. Funct. Mater.* 25.35 (2015), pp. 5617–5624.

[168] T. F. Schulze and T. W. Schmidt, *Energy Environ. Sci.* 8.1 (2015), pp. 103–125.

[169] A Monguzzi et al., *Nano Lett.* 14.11 (2014), pp. 6644–6650.

[170] K. Xu et al., *J. Phys. Chem. C* 119.42 (2015), pp. 23801–23812.

[171] R. Tao et al., *Chem. Commun.* 51.62 (2015), pp. 12403–12406.

[172] X. Cui et al., *J. Org. Chem..* 79.5 (2014), pp. 2038–2048.

[173] W. Wu et al., *J. Org. Chem.* 76.17 (2011), pp. 7056–7064.

[174] V. Yakutkin et al., *Chem. Eur. J.* 14.32 (2008), pp. 9846–9850.

[175] T. N. Singh-Rachford and F. N. Castellano, *J. Phys. Chem. A* 112.16 (2008), pp. 3550–3556.

[176] S. Baluschev et al., *Angew. Chem. Int. Ed.* 46.40 (2007), pp. 7693–7696.

[177] W. Wang et al., *Nano Lett.* 15.10 (2015), pp. 6332–6338.

[178] S. H. Askes, A. Bahreman, and S. Bonnet, *Angew. Chem. Int. Ed.* 53.4 (2014), pp. 1029–1033.

[179] C. Ye et al., *Phys. Chem. Chem. Phys.* 18.5 (2016), pp. 3430–3437.

[180] H. Kouno et al., *Chem. Sci.* 7 (2016).

[181] T. Gatti et al., *The Journal of Physical Chemistry C* 119.31 (2015), pp. 17495–17501.

[182] P. Mahato et al., *Nat. Mater.* 14 (2015), p. 924.

[183] J. Zimmermann et al., *J. Chem. Phys.* 141.18 (2014), p. 184104.

[184] C. Wohnhaas et al., *ACS Macro Lett.* 2.5 (2013), pp. 446–450.

[185] Y. Murakami et al., *J. Phys. Chem. B* 120.4 (2016), pp. 748–755.

[186] M. Poznik et al., *RSC Adv.* 6.48 (2016), pp. 41947–41950.

[187] S. H. Askes et al., *Chem. Commun.* 51.44 (2015), pp. 9137–9140.

[188] C. Ye et al., *J. Mater. Chem. C* 2.40 (2014), pp. 8507–8514.

[189] M. Penconi et al., *Photochem. Photobiol. Sci.* 13.1 (2014), pp. 48–61.

[190] Q. Liu et al., *J. Am. Chem. Soc.* 135.13 (2013), pp. 5029–5037.

[191] K. Tanaka, K. Inafuku, and Y. Chujo, *Chem. Commun.* 46.24 (2010), pp. 4378–4380.

[192] A. Turshatov et al., *New J. Phys.* 13.8 (2011), p. 083035.

[193] O. S. Kwon et al., *ACS nano* 10.1 (2016), pp. 1512–1521.

[194] J.-H. Kim and J.-H. Kim, *J. Am. Chem. Soc.* 134.42 (2012), pp. 17478–17481.

[195] K. Katta et al., *Macromol. Rapid. Commun.* 36.11 (2015), pp. 1083–1083.

[196] A. J. Tilley et al., *Chem. Phys. Lett.* 618 (2015), pp. 198–202.

[197] C. Wohnhaas et al., *Macromol. Biosci.* 13.10 (2013), pp. 1422–1430.

[198] J.-H. Kang and E. Reichmanis, *Angew. Chem. Int. Ed.* 51.47 (2012), pp. 11841–11844.

[199] A. Monguzzi et al., *Adv. Funct. Mater.* 22.1 (2012), pp. 139–143.

[200] Y. C. Simon and C. Weder, *J. Mater. Chem.* 22.39 (2012), pp. 20817–20830.

[201] C. Wohnhaas et al., *Macromol. Biosci.* 11.6 (2011), pp. 772–778.

[202] M. Sitkovsky and D. Lukashev, *Nat. Rev. Immunol.* 5.9 (2005), pp. 712–721.

[203] S. M. Borisov, C. Larndorfer, and I. Klimant, *Adv. Funct. Mater.* 22.20 (2012), pp. 4360–4368.

[204] R. A. Petros and J. M. DeSimone, *Nat. Rev. Drug Discov.* 9.8 (2010), pp. 615–627.

[205] A Monguzzi, R Tubino, and F Meinardi, *Phys. Rev. B* 77.15 (2008), p. 155122.

[206] I. Berlman. Elsevier, 2012.

[207] S. M. Borisov, G. Zenkl, and I. Klimant, *ACS Appl. Mater. Interfaces* 2.2 (2010), pp. 366–374.

[208] T. Ogawa et al., *Sci. Rep.* 5 (2015).

[209] A. Monguzzi et al., *Phys. Chem. Chem. Phys.* 14.13 (2012), pp. 4322–4332.

[210] D. B. Papkovsky and T. C. O'Riordan, *J. Fluoresc.* 15.4 (2005), pp. 569–584.

[211] A Monguzzi et al., *Phys. Rev. B* 82.12 (2010), p. 125113.

[212] C. Y. Tay et al., *Nano Res.* 7.6 (2014), pp. 805–815.

[213] A. Manke, L. Wang, and Y. Rojanasakul, *Biomed. Res. Int.* 2013 (2013).

[214] W. B. Busa and R. Nuccitelli, *Am. J. Physiol.* 246.4 Pt 2 (1984), R409–38.

[215] J. R. Casey, S. Grinstein, and J. Orlowski, *Nat. Rev. Mol. Cell Biol.* 11.1 (2010), pp. 50–61.

[216] D. Lagadic-Gossmann, L. Huc, and V. Lecureur, *Cell Death Differ.* 11.9 (2004), pp. 953–61.

[217] H. Y. Wang and G. Oster, *Nature* 396.6708 (1998), pp. 279–282.

[218] R. A. Cardone, V. Casavola, and S. J. Reshkin, *Nat. Rev. Cancer.* 5.10 (2005), pp. 786–95.

[219] J. R. Griffiths, *Br. J. Cancer* 64 (1991), pp. 425–427.

[220] S. Harguindey et al., *Biochim. Biophys. Acta* 1756.1 (2005), pp. 1–24.

[221] R. Perona and R. Serrano, *Nature* 334.6181 (1988), pp. 438–440.

[222] I. F. Tannock and D. Rotin, *Cancer Res.* 49 (1989), pp. 4373–4384.

[223] S. M. Day et al., *Nat. Med.* 12.2 (2006), pp. 181–9.

[224] M. Obara, M. Szeliga, and J. Albrecht, *Neurochem. Int.* 52.6 (2008), pp. 905–19.

[225] S. Sánchez-Armáss et al., *Am. J. Physiol., Cell Physiol.* 290.2 (2006), pp. C524–C538.

[226] R. D. Vaughan-Jones, K. W. Spitzer, and P. Swietach, *J. Mol. Cell. Cardiol.* 46.3 (2009), pp. 318–31.

[227] S. A. Hilderbrand et al., *Bioconjug. Chem.* 19 (2008), pp. 1635–1639.

[228] L. Li et al., *Anal. Chem.* 86.12 (2014), pp. 6115–6120.

[229] B. Tang et al., *J. Am. Chem. Soc.* 131.8 (2009), pp. 3016–3023.

[230] L. Chen et al., *RSC Adv.* 3.32 (2013), pp. 13412–13416.

[231] Y. Tian et al., *Biomaterials* 31.29 (2010), pp. 7411–7422.

[232] X. H. Gao, W. C. W. Chan, and S. M. Nie, *J. Biomed. Opt.* 7.4 (2002), pp. 532–537.

[233] X. Ji et al., *J. Am. Chem. Soc.* 134.13 (2012), pp. 6006–6017.

[234] G. Kaur and S. K. Tripathi, *Mater. Chem. Phys.* 143.2 (2014), pp. 514–523.

[235] J. Ma et al., *Nanotechnology* 17.9 (2006), pp. 2083–2089.

[236] J. M. Pietryga et al., *Chem. Rev.* 116.18 (2016), pp. 10513–10622.

[237] M. V. Kovalenko et al., *ACS nano* 9.2 (2015).

[238] M. A. Boles et al., *Nat. Mater.* 15.2 (2016), pp. 141–153.

[239] Z. Deng et al., *J. Phys. Chem. B* 111.41 (2007), pp. 12024–12031.

[240] J. R. Lakowicz. Springer, 2010.

[241] A. Maroto et al., *ChemPhysChem* 8.2 (2007), pp. 220–223.

[242] I. L. Medintz et al., *Nat. Mater.* 4.6 (2005), pp. 435–446.

[243] X. Michalet et al., *Science* 307 (2005), pp. 538–544.

[244] B. R. Panda and A. Chattopadhyay, *J. Colloid Interface Sci.* 316.2 (2007), pp. 962–967.

[245] E. Allard and C. Larpent, *J. Polym. Sci. A* 46.18 (2008), pp. 6206–6213.

[246] A. Burns et al., *Small* 2.6 (2006), pp. 723–726.

[247] A. Burns, H. Ow, and U. Wiesner, *Chem. Soc. Rev.* 35.11 (2006), p. 1028.

[248] Y.-N. Chen et al., *Chem. Commun.* 50.62 (2014), p. 8571.

[249] H.-s. Peng et al., *Angew. Chem. Int. Ed.* 49.25 (2010), pp. 4246–4249.

[250] X.-d. Wang, R. J. Meier, and O. S. Wolfbeis, *Adv. Funct. Mater.* 22.20 (2012), pp. 4202–4207.

[251] R. Hartmann et al., *Angew. Chem. Int. Ed.* 54.4 (2015), pp. 1365–1368.

[252] H. A. Clark et al., *Sens. Actuators B Chem.* 51.1 (1998), pp. 12–16.

[253] P. Rivera_Gil et al., *Small* 8.6 (2012), pp. 943–948.

[254] O. Kreft et al., *J. Mater. Chem.* 17.42 (2007), pp. 4471–4476.

[255] K. Kantner et al., *Small* 11.8 (2015), pp. 896–904.

[256] W. Shi, X. H. Li, and H. M. Ma, *Methods Appl. Fluoresc.* 2.4 (2014).

[257] S. Chen et al., *J. Am. Chem. Soc.* 135.13 (2013), pp. 4926–4929.

[258] G. Miesenbock, D. A. De Angelis, and J. E. Rothman, *Nature* 394 (1998), pp. 192–195.

[259] C.-G. Niu et al., *Anal. Bioanal. Chem.* 383.2 (2005), pp. 349–357.

[260] A. A. Venn et al., *Proc. Natl. Acad. Sci.* 106.39 (2009), pp. 16574–16579.

[261] I. L. Medintz et al., *Nat. Mater.* 9.8 (2010), pp. 676–684.

[262] K. Paek et al., *ACS Nano* (2014).

[263] P. T. Snee et al., *J. Am. Chem. Soc.* 128.41 (2006), pp. 13320–13321.

[264] M. Suzuki et al., *J. Am. Chem. Soc.* 130.17 (2008), pp. 5720–5725.

[265] M. Tomasulo, I. Yildiz, and F. M. Raymo, *J. Phys. Chem. B* 110.9 (2006), pp. 3853–3855.

[266] X. Wang et al., *Analyst* 135.7 (2010), pp. 1585–1591.

[267] A. M. Dennis et al., *ACS Nano* 6.4 (2012), pp. 2917–2924.

[268] T. Jin et al., *Chem. Commun.* 46.14 (2010), p. 2408.

[269] W. Shi, X. Li, and H. Ma, *Angew. Chem. Int. Ed.* 51.26 (2012), pp. 6432–6435.

[270] S. Brovelli et al., *Nano Lett.* 14.2 (2014), pp. 486–494.

[271] S. Brovelli et al., *Nano Lett.* 14.7 (2014), pp. 3855–3863.

[272] C. Galland et al., *Nano Lett.* 13.1 (2013), pp. 321–328.

[273] V. Pinchetti et al., *ACS Nano* (2016).

[274] J. I. Wong et al., *ACS nano* 8.3 (2014), pp. 2873–2879.

[275] U. Soni et al., *ACS nano* 8.1 (2013), pp. 113–123.

[276] J. Lin, S. T. Pantelides, and W. Zhou, *ACS Nano* 9.5 (2015), pp. 5189–5197.

[277] S. Liu et al., *ChemPhysChem* 16.8 (2015), pp. 1663–1669.

[278] D. Battaglia, B. Blackman, and X. Peng, *J. Am. Chem. Soc.* 127.31 (2005), pp. 10889–10897.

[279] S. Nizamoglu et al., *Appl. Phys. Lett.* 92.11 (2008), pp. 113110–113110.

[280] S. Sapra et al., *Adv. Mater.* 19.4 (2007), pp. 569–572.

[281] A. Teitelboim and D. Oron, *ACS nano* 10.1 (2015), pp. 446–452.

[282] H. Zhao, A. Vomiero, and F. Rosei, *Small* 11.43 (2015), pp. 5741–5746.

[283] H. Zhao et al., *Nanoscale* 8.7 (2016), pp. 4217–4226.

[284] E. Mosconi et al., *ACS Energy Lett.* 1.2 (2016), pp. 454–463.

[285] D. Ghezzi et al., *Nat. Commun.* 2 (2011), p. 166.

[286] D. Ghezzi et al., *Nat. Photonics* 7.5 (2013), pp. 400–406.

[287] W. W. Yu et al., *Chem. Mater.* 15.14 (2003), pp. 2854–2860.

[288] C. Galland et al., *Nano Lett.* 13.1 (2013), pp. 321–328.

[289] Y. A. Yang et al., *Angew. Chem.* 117.41 (2005), pp. 6870–6873.

[290] C. H. Fox et al., *J. Histochem. Cytochem.* 33.8 (1985), pp. 845–853.

[291] M. M. Mariani et al., *Analyst* 134.6 (2009), pp. 1154–1161.

[292] A. D. Meade et al., *Anal. Bioanal. Chem.* 396.5 (2010), pp. 1781–1791.

[293] U. Schnell et al., *Nat. Methods* 9.2 (2012), pp. 152–158.

[294] Y. Williams et al., *J. Microsc.* 232.1 (2008), pp. 91–98.

[295] D. Gerlier and N. Thomasset, *J. Immunol. Methods* 94.1 (1986), pp. 57–63.

[296] T. Mosmann, *J. Immunol. Methods* 65.1 (1983), pp. 55–63.

[297] J. Chudzik, S. Ohkuma, and B. Poole, *J. Cell. Biol.* 102.3 (1986), pp. 959–966.

[298] Y.-S. Liu et al., *J. Phys. Chem. C* 111.7 (2007), pp. 2872–2878.

[299] J. Kolny-Olesiak and H. Weller, *ACS Appl. Mater. Interfaces* 5.23 (2013), pp. 12221–12237.